



TECHNISCHE
UNIVERSITÄT
WIEN

Vienna University of Technology

DIPLOMARBEIT

Non-Hermitian dynamics in the vicinity of an exceptional point

ausgeführt unter der Leitung von

Univ.-Prof. Dipl.-Ing. Dr.techn. Stefan Rotter
Institut für Theoretische Physik, e136

eingereicht an der Technischen Universität Wien
Fakultät für Physik

von

Schumer Alexander, BSc
Matrikelnummer 1027206
Römergasse 72/12
1160 Wien, Österreich, EU
alexschumer@student.tuwien.ac.at

Wien, am 28. Dezember 2017

Contents

| | | |
|----------|---|-----------|
| 1 | Introduction | 1 |
| 2 | Exceptional points in non-Hermitian Hamiltonians | 3 |
| 2.1 | Biorthogonal quantum mechanics | 3 |
| 2.2 | Model Hamiltonian | 4 |
| 2.3 | Coalescing eigenvalues and eigenvectors | 5 |
| 2.4 | Geometric phase | 6 |
| 2.5 | Generalized eigensystem at the EP | 7 |
| 2.5.1 | Properties of $ v\rangle$ and $ h\rangle$ | 7 |
| 2.5.2 | Projection onto the generalized eigenbasis at the EP | 9 |
| 2.6 | Crossing a branch cut | 9 |
| 2.6.1 | Eigenvalue flip | 9 |
| 2.6.2 | Eigenvector flip | 10 |
| 2.7 | Going through the EP | 12 |
| 3 | Time evolution operator $U(t)$ in the instantaneous eigenbasis of $H(t)$ | 15 |
| 3.1 | Time dependent similarity transformations | 15 |
| 3.2 | Schrödinger equation in the eigenbasis of the Hamiltonian | 16 |
| 3.3 | Special solutions for $\tilde{U}(t)$ | 17 |
| 3.3.1 | Stationary time evolution | 17 |
| 3.3.2 | Time evolution in the vicinity of the EP | 18 |
| 3.3.3 | Adiabatic prediction | 18 |
| 3.3.4 | Coupled adiabatic time evolution | 19 |
| 4 | Generalized Hermitian form | 21 |
| 4.1 | Biorthogonality using the c-product | 21 |
| 4.2 | Non-orthogonality using the Hermitian form | 22 |
| 4.3 | Biorthogonality using a generalized Hermitian form | 23 |
| 4.3.1 | Effect of B on eigenvectors | 25 |
| 4.4 | Inner product using generalized Hermitian form | 26 |
| 4.4.1 | Inner product for different bases | 26 |
| 4.5 | Contour lines of $\Im(\theta)$ | 28 |
| 4.6 | B -pseudo-Hermiticity | 30 |
| 4.7 | B -norm for time dependent Hamiltonians | 31 |
| 4.8 | Asymmetric Hamiltonians | 32 |

| | | |
|-----------|---|-----------|
| 5 | Time evolution at the EP | 35 |
| 5.1 | Stationary time evolution | 35 |
| 5.2 | Dynamical time evolution at the EP | 36 |
| 6 | Transfer efficiency and chirality | 39 |
| 6.0.1 | Transfer efficiency | 39 |
| 6.0.2 | Population inversion | 40 |
| 6.0.3 | Chirality | 41 |
| 6.1 | Relations with the time evolution operator | 41 |
| 7 | Analytical solutions for special parameter paths | 43 |
| 7.1 | Uncoupled second order differential equations | 43 |
| 7.2 | Analytical solutions for straight parameter paths | 44 |
| 7.3 | Analytical solutions for EP-centered circular paths | 48 |
| 7.3.1 | Analytic continuation | 51 |
| 7.3.2 | Uniform asymptotic expansion | 51 |
| 7.3.3 | Floquet basis and the one-cycle evolution operator | 52 |
| 7.3.4 | Reversing the loop direction | 53 |
| 8 | Results for EP-centered circles | 55 |
| 8.1 | Single round | 55 |
| 8.2 | Multiple rounds | 60 |
| 8.3 | Half-integer order ν | 61 |
| 8.4 | Asymptotic expansion of $U(T)$ at $\phi_0 = 0$ | 66 |
| 9 | Results for general circular paths | 71 |
| 9.1 | Fixed radius, variable center | 71 |
| 9.2 | Fixed center, variable radius | 73 |
| 10 | Results for straight paths | 77 |
| 10.1 | Going into an EP | 77 |
| 10.2 | Going through an EP | 79 |
| 10.3 | Experimental predictions for EP-centered squares | 80 |
| 11 | Conclusion and Outlook | 83 |
| | Acknowledgments | 85 |
| | List of Acronyms and Abbreviations | 87 |
| | Bibliography | 88 |

1 Introduction

The description of a quantum system where some degrees of freedom are not incorporated, i.e. of systems with gain or loss, involves a Hamiltonian that is inherently non-Hermitian [1, 2]. This non-Hermiticity results in non-orthogonal eigenvectors as well as complex eigenvalues where the real part corresponds to the frequency of the corresponding mode and the imaginary part to the respective line width. To maintain the convenient concepts of Hermitian Hamiltonians such as Dirac inner products and expectation values it is necessary to generalize certain well-founded aspects of Hermitian quantum mechanics [3–5].

One key feature of non-Hermitian Hamiltonians appears in the light of spectral degeneracies, where eigenvalues coalesce. In the Hermitian case, the eigenvectors at the point of degeneracy can be chosen to constitute an orthonormal basis. This type of singularity is called a *diabolical point* (DP) [6]. At a non-Hermitian degeneracy, also called an *exceptional point* (EP) [7–12], not only the eigenvalues but also the associated eigenvectors merge. Due to the resulting defective eigenbasis (EB) and the special topological structure of the eigenvalue surfaces in the vicinity of those branch point degeneracies there are several astounding effects linked to EPs. Some of the applications include unidirectional invisibility in a Bragg scattering grating [13], coherent perfect absorbers (CPA) [14], EP-enhanced sensing [15–17], robust wireless power transfer [18] or reversing the pump dependence of a laser [19, 20].

The aforementioned topological structure of the eigenvalue sheets at an EP is given by self-intersecting Riemann sheets. By varying at least two system parameters in a closed contour that encloses the EP it is possible to exploit those topological properties that are closely related to the Berry phase picked up during a loop [21–23]. Upon encircling an EP the eigenvalues and eigenvectors interchange with an additional sign change in one of the eigenvectors, which has been demonstrated in a microwave cavity experiment using successive small parameter steps to encircle an EP [24, 25].

The physical behavior for dynamical parameter variations is however governed by the non-Hermiticity and hence does not follow the adiabatic theorem even for very slow parameter changes. The non-Hermitian contribution in the Hamiltonian is said to be singularly perturbing the system. As a result, nonadiabatic transitions inherent in dynamically encircling an EP lead to intriguing new effects such as an intrinsic chirality of the encircling process [26–31]. For virtually all initial configurations the final state only depends on the direction of encirclement. This asymmetric switch has been demonstrated experimentally for a waveguide with undulating boundaries and losses [32] as well as in an cavity optomechanical system using vibrational modes of a slightly non-square membrane [33].

In this thesis we study foremost the chiral behavior that adheres to an EP upon dynamical parameter variations. These variations include closed loops that enclose the EP and also ones that exclude it, as well as trajectories with different initial and final parameter configurations (not closed contours).

The first part of this work is building up a suitable non-Hermitian framework, focusing in particular on the features of non-Hermitian degeneracies (exceptional points) using a particular 2×2 Hamiltonian that has been previously used to describe experimental setups [32, 33]. Within this methodological part we derive a generalized inner product that comes as a natural extension to the Dirac 'bracket' formalism. This new two-form is needed to account for the non-orthogonality of the eigenvectors of a system subject to loss.

In order to be able to analytically investigate the asymmetric switch that appears for closed parameter contours in the vicinity of an EP, the second part of this thesis is dedicated to the exact solutions of the underlying coupled differential equations for special temporal variations of the Hamiltonian. Using a class of circular paths without the restrictions on the initial and end points imposed previously, we reach a better understanding of quasi-adiabaticity [26, 27, 30, 31]. With this tool at hand we show that chirality is not a compulsory property of EP-enclosing parameter contours. We rather find that a certain closeness to the EP is required to obtain chirality.

A new class of analytical solutions for general straight parameter paths in the vicinity of an EP is also introduced, that allows us to concatenate arbitrary parametrical tracks, performing rectangular parameter variations where only one parameter is changed at a time including or excluding an EP. These solutions will be particularly relevant for recent experimental implementations [33].

With the help of arbitrary straight paths we also analyze the effect of the EP on the eigenvector populations when an EP is passed through. A static parametric analysis reveals that the EP exactly levels the eigenvector coefficients so that they get an universal ratio of $\pm i$ [34, 35]. The dynamical aspects for passing through an EP are quite remarkable as the constant ratio of the eigenvectors raises the question whether this is breaking time-reversal symmetry or if it is connected to an information loss at the EP.

2 Exceptional points in non-Hermitian Hamiltonians

The study of artificial physical systems with gain or loss has grown vastly over the last decade [19, 20, 32, 33, 36–39]. The description of these systems usually relies on the time dependent Schrödinger equation (TDSE)¹

$$i\partial_t\psi(t) = H(t)\psi(t) \quad (2.1)$$

with a complex non-Hermitian Hamiltonian that features exceptional points for certain parameter configurations. The simplest models where an EP is accessible is a lossy two-level system that is described by a 2×2 Hamiltonian

$$H = \begin{pmatrix} \omega_1 + i\frac{\gamma_1}{2} & g \\ g & \omega_2 + i\frac{\gamma_2}{2} \end{pmatrix}, \quad (2.2)$$

where $\omega_{1,2}$ are the frequencies of the modes, $\gamma_{1,2}$ are the loss/gain rates and g is the coupling strength. All these parameters are chosen to be real. A positive imaginary part $\gamma > 0$ of a complex frequency $\omega + i\gamma$ corresponds to gain and a negative imaginary part to loss. This Hamiltonian is clearly non-Hermitian $H \neq H^\dagger$. The model Hamiltonian in Eq. 2.2 is used in [30, 32] and hence the notation is partially adopted.

2.1 Biorthogonal quantum mechanics

A far-reaching consequence for non-Hermitian operators is that the eigenvectors are not necessarily orthogonal under the standard Hermitian inner product $(|g_i\rangle)^\dagger |g_i\rangle \equiv \langle g_i | g_i \rangle$. In order to keep the formalism of Hermitian quantum mechanics intact, it is necessary to introduce left eigenstates $\langle f_i^* |$, i.e. the dual basis², which are in general not the Hermitian conjugate ($\langle f_i^* | \neq |f_i\rangle^\dagger$) of the right ones anymore. Those left eigenstates are chosen in a way so that they form a biorthogonal set of basis vectors $\langle f_i^* | g_j \rangle = \delta_{ij}$ using the standard Hermitian form [4]. Additionally, they fulfill a closure relation $\sum_i |g_i\rangle \langle f_i^*| = \mathbb{1}$.

By restricting the Hamiltonian to be symmetric $H = H^T$, the left eigenstates are given as the transpose of their right counterparts ($\langle f_i^* | = (|f_i\rangle)^T$). The resulting inner product $\langle \hat{f}_i | g_i \rangle \equiv (|f_i\rangle)^T |g_i\rangle$ is known as the *c-product* [1, 40]. We will denote left eigenstates that are obtained as the transpose of their corresponding right partners with

¹We have set $\hbar = 1$.

²The star denotes the dual basis and not complex conjugation.

a hat ($\langle \hat{f}_i | \equiv (|f_i\rangle)^T$) to distinguish them from the Dirac formalism.

Although a redefinition of the inner product is a viable approach, we will show an alternative way how to extend the Hermitian formalism for non-Hermitian operators in [chapter 4](#).

2.2 Model Hamiltonian

With a suitable gauge transformation the Hamiltonian in [Eq. 2.2](#) can be brought to a relative frame of reference

$$H = \begin{pmatrix} -\omega - i\frac{\gamma}{2} & g \\ g & \omega + i\frac{\gamma}{2} \end{pmatrix} \quad (2.3)$$

with $\omega = (\omega_2 - \omega_1)/2$ and $\gamma = (\gamma_1 - \gamma_2)/2$. In addition to being symmetric, this Hamiltonian is also traceless $\text{Tr}(H) = 0$ with eigenvalues

$$\lambda_{\pm} = \pm\lambda = \pm\sqrt{(\omega + i\gamma/2)^2 + g^2}, \quad (2.4)$$

that are in general complex. When we define a complex frequency $\xi = \omega + i\gamma/2 \in \mathbb{C}$ the eigenvalues become $\pm\sqrt{\xi^2 + g^2}$. The parameter region where $\lambda \in \mathbb{R}$ is related to a parity-time symmetry (\mathcal{PT} -symmetry) [\[38\]](#) of the Hamiltonian $(\mathcal{PT})H(\mathcal{PT}) = H$ that we will discuss in the following.

The eigenvectors of H can be parametrized by a single³ mixing angle $\theta = \arctan(-g/(\omega + i\gamma/2)) = \arctan(-g/\xi)$ as

$$|+\rangle = \begin{pmatrix} -\sin(\theta/2) \\ \cos(\theta/2) \end{pmatrix}, \quad |-\rangle = \begin{pmatrix} \cos(\theta/2) \\ \sin(\theta/2) \end{pmatrix} \quad (2.5)$$

and they fulfill the eigenvalue equations $H|\pm\rangle = \lambda_{\pm}|\pm\rangle$. We want to note here that we are going to use the `atan2` [\[41\]](#) the two argument inverse tangent, instead of the `arctan` so that its branch cut aligns with the branch cut of the square root.

As the Hamiltonian is non-Hermitian, a set of biorthogonal left eigenvectors $\langle \pm |$ cannot simply be obtained by the Hermitian conjugate $\langle \pm | \neq |\pm\rangle^\dagger$. However, by restricting the analysis to a symmetric Hamiltonian one finds that the left eigenstates are the transpose of the right ones. We denote left vectors that come from their respective transposed right ones by a hat $\langle \hat{\pm} | := |\pm\rangle^T$. The left eigenvectors are hence

$$\begin{aligned} \langle \hat{+} | &= |+\rangle^T = \begin{pmatrix} -\sin(\theta/2) & \cos(\theta/2) \end{pmatrix}, \\ \langle \hat{-} | &= |-\rangle^T = \begin{pmatrix} \cos(\theta/2) & \sin(\theta/2) \end{pmatrix}. \end{aligned} \quad (2.6)$$

³This is not possible for non-symmetric Hamiltonians.

This set of left and right eigenvectors are biorthogonal and complete [4]

$$\begin{aligned}\langle \hat{\pm} | \pm \rangle &= 1 , \\ \langle \hat{\mp} | \pm \rangle &= 0 , \\ |+\rangle \langle \hat{+}| + |-\rangle \langle \hat{-}| &= \mathbb{1} .\end{aligned}\tag{2.7}$$

We want to mention here that despite the amenities involved using the c-product there are several little discomforts. Eigenstates that are chosen to admit a \mathcal{PT} -symmetric phase are not biorthogonal under the c-product anymore. This is because $|+\rangle$ from Eq. 2.5 needs to be redefined as $|\tilde{+}\rangle = i|+\rangle$ to be \mathcal{PT} -symmetric in the parameter region where the Hamiltonian is \mathcal{PT} -symmetric. Then the c-product yields $\langle \hat{+} | \tilde{+} \rangle = -1$, which is not biorthogonal. We will show that there is a better way to generalize the Hermitian form so that biorthogonality is upheld for vectors that allow \mathcal{PT} -symmetry.

2.3 Coalescing eigenvalues and eigenvectors

From Eq. 2.4 we derive that the eigenvalues coalesce when

$$(\omega + i\gamma/2)^2 + g^2 = 0 .\tag{2.8}$$

This gives two separate conditions for the real and imaginary part of Eq. 2.8 that have to be fulfilled simultaneously

$$\omega\gamma = 0 \Rightarrow \omega_{\text{EP}} = 0 ,\tag{2.9}$$

$$g^2 - \gamma^2/4 = 0 \Rightarrow g_{\text{EP}\pm} = \pm\gamma/2 .\tag{2.10}$$

One could assume in Eq. 2.9 that $\gamma = 0$ is also a solution for an EP, but for $\gamma = 0$ the EP is actually a DP, that is a Hermitian degeneracy, located at $\{g_{\text{DP}}, \omega_{\text{DP}}\} = \{0, 0\}$.

The equation for g_{EP} in Eq. 2.10 admits two solutions for $\gamma \neq 0$ so that an EP always appears pairwise: one EP at positive values of the coupling strength g and the other at negative values of g . To distinguish between the two EPs we will refer to the EP at $\{g, \omega\} = \{+\gamma/2, 0\}$ as the positive EP (EP_+) and to the one at $\{g, \omega\} = \{-\gamma/2, 0\}$ as the negative EP (EP_-).

In Fig. 2.1 we display the topological structure of the eigenvalue spectrum upon variation of two system parameters g, ω in the vicinity of the EP_+ . These are in fact the Riemann surfaces of real (left) and imaginary parts (right) of the complex square root function. The real part has a crossing that runs along $g \in [g_{\text{EP}_-}, g_{\text{EP}_+}]$ with $\omega = 0$ and the imaginary part has one crossing at $g \leq g_{\text{EP}_-}$ and another at $g \geq g_{\text{EP}_+}$. The EP, which is located in the center of each image, therefore separates the real and the imaginary crossing but is part of both of them as $\lambda = 0$ at the EP.

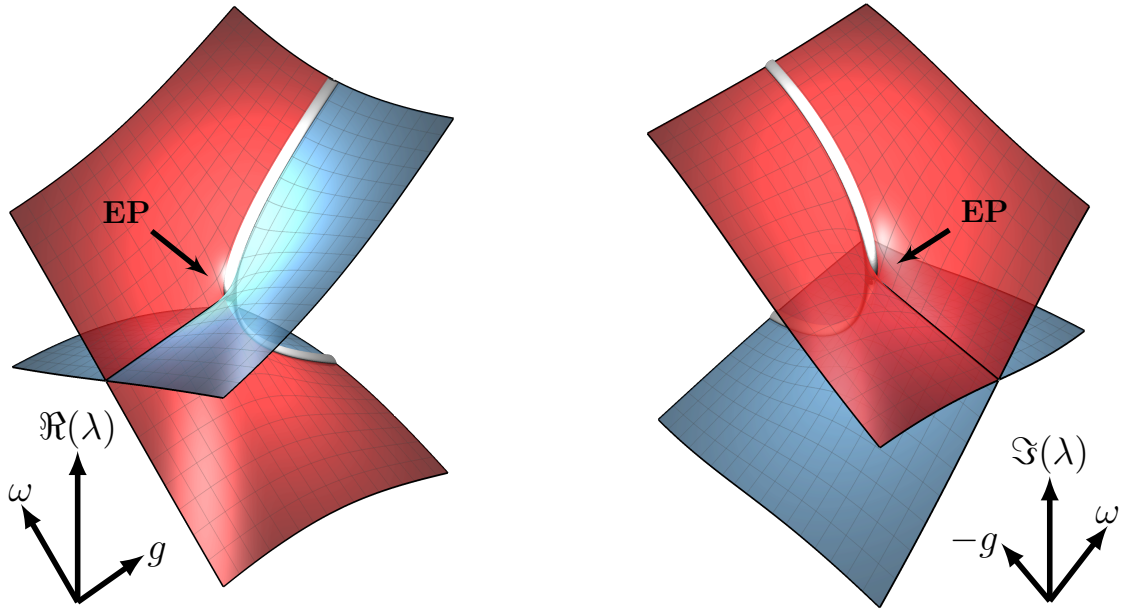


Figure 2.1: Real (left) and imaginary (right) part of the eigenvalue surfaces as a function of two parameters g, ω in the vicinity of an EP (indicated by the arrow). These can also be regarded as the self-intersecting Riemann surfaces of the complex square root function $\sqrt{(\omega + i\gamma/2)^2 + g^2}$ with constant γ . The color corresponds to an eigenvalue with relative gain (red) and loss (blue).

2.4 Geometric phase

The geometric phase that some general eigenvectors $|n\rangle$ pick up along a closed contour C by varying parameters \mathbf{R} in its Hamiltonian is the Berry phase [42]

$$\gamma_n[C] = i \oint_C \langle n(\mathbf{R}) | \nabla_{\mathbf{R}} | n(\mathbf{R}) \rangle d\mathbf{R}, \quad (2.11)$$

that is implicitly taken into account in the basis vectors if we impose on our basis to be parallel-transported $\langle n(\mathbf{R}) | \nabla_{\mathbf{R}} | n(\mathbf{R}) \rangle = 0$ [43]. The parameter variations \mathbf{R} that we perform include a single real parameter, namely the time t ($\mathbf{R} \equiv t$). As we do not want any geometric phase to appear explicitly, the basis defined in Eqs. 2.5 and 2.6 is already parallel-transported $\langle \hat{\pm} | \partial_t | \pm \rangle = 0$ so that $\gamma_{\pm}[C] = 0$.

2.5 Generalized eigensystem at the EP

At the parameter configurations $\{g = g_{\text{EP}\pm}, \omega = 0\}$ the Hamiltonian

$$H_{\text{EP}\pm} = \frac{\gamma}{2} \begin{pmatrix} -i & \pm 1 \\ \pm 1 & i \end{pmatrix} \quad (2.12)$$

is defective and cannot be diagonalized. This also manifests in the mixing angle θ that diverges logarithmically towards $i\infty$. The eigenbasis ($|-\rangle, |+\rangle$) is therefore ill-defined at the EP.

The only eigenvector at the EP is $|v_{\pm}\rangle = (1, \pm i)^T$. The two EPs (EP_+, EP_-) can be distinguished by the sign in front of the i in its respective eigenvector that determines the chirality⁴ of the EP [35].

Although the Hamiltonian at the EP has no diagonal representation in its eigenbasis as there is only one eigenvector one can transform it via a similarity transformation $J = X^{-1}HX$ to a block-diagonal matrix J , i.e. its Jordan normal form. The basis transformation matrix X that does this is given by a generalized eigenbasis $X = (|v\rangle, |h\rangle)$, where $|h\rangle$ is called a generalized eigenvector of rank 2. The generalized eigenbasis for both EPs is found to be

$$|v_{\pm}\rangle = v_0 \begin{pmatrix} 1 \\ \pm i \end{pmatrix}, \quad |h_{\pm}\rangle = \frac{v_0 h_0}{\gamma} \begin{pmatrix} i \\ \pm 1 \end{pmatrix}, \quad (2.13)$$

where we have left two normalizing constants v_0, h_0 for later convenience. These two vectors generally fulfill the relations

$$H_{\text{EP}}|v\rangle = \lambda|v\rangle \quad \text{and} \quad H_{\text{EP}}|h\rangle = \lambda|h\rangle + a|v\rangle \quad (2.14)$$

with $\lambda = 0$ for the traceless symmetric model Hamiltonian that we use. The factor $a = v_0 h_0$ looks unfamiliar but does not alter the fact that $|h_{\pm}\rangle$ is a generalized eigenvector of rank 2. For the particular choice of $v_0 = 1/\sqrt{2}$ and $h_0 = \gamma$ we find

$$|v_{\pm}\rangle = \frac{1}{\sqrt{2}} \begin{pmatrix} 1 \\ \pm i \end{pmatrix}, \quad |h_{\pm}\rangle = \frac{1}{\sqrt{2}} \begin{pmatrix} i \\ \pm 1 \end{pmatrix}. \quad (2.15)$$

2.5.1 Properties of $|v\rangle$ and $|h\rangle$

For either one of the EPs it is apparent from Eq. 2.13 that $|v\rangle$ and $|h\rangle$ are always self-orthogonal under the c-product independent of the normalization

$$\langle \hat{v}|v\rangle = 0, \quad \langle \hat{h}|h\rangle = 0. \quad (2.16)$$

However, it is convenient to normalize both vectors using the standard inner product as shown by the prefactor in Eq. 2.15. This avoidance of the c-product becomes even

⁴The term chirality is used later on in a different context and given a new meaning.

more clear when we decompose H_{EP_+} into its Jordan normal form using a similarity transformation

$$J = X^{-1} H_{\text{EP}_+} X , \quad (2.17)$$

with

$$X = \frac{1}{\sqrt{2}} \begin{pmatrix} 1 & i \\ i & 1 \end{pmatrix} , \quad X^{-1} = \frac{1}{\sqrt{2}} \begin{pmatrix} 1 & -i \\ -i & 1 \end{pmatrix} \quad \text{and} \quad J = \begin{pmatrix} 0 & \gamma \\ 0 & 0 \end{pmatrix} . \quad (2.18)$$

The row vectors of the matrix X^{-1} in Eq. 2.18 already include a set of left eigenvectors $\langle v| = |v\rangle^\dagger$ and $\langle h| = |h\rangle^\dagger$ of H_{EP_+} that are by construction orthogonal onto $|v\rangle$ and $|h\rangle$ under the standard Hermitian form

$$\langle v| = \frac{1}{\sqrt{2}} (1 \quad -i) , \quad \langle h| = \frac{1}{\sqrt{2}} (-i \quad 1) \quad (2.19)$$

rendering the use of the c-product useless. As the off-diagonal element of J is γ this Jordan normal form at the EP_+ also describes the DP at $\gamma = 0$. It is correspondingly equivalent to put the factor γ into the generalized eigenvector $|h\rangle$. In that case the basis would depend on γ which is not necessarily constant anymore. The two possible choices refer to the Schrödinger and Heisenberg picture where we have chosen the latter one.

The (Dirac) left eigenvectors can generally be used for projections and together with the right eigenvectors they form a complete basis

$$\langle v|h\rangle = \langle h|v\rangle = 0 , \quad (2.20)$$

$$\langle v|v\rangle = \langle h|h\rangle = 1 ,$$

$$|v\rangle\langle v| + |h\rangle\langle h| = \mathbb{1}_{2 \times 2} . \quad (2.21)$$

At this point we also mention the completeness relation for the c-product, but just as an additional indication of the c-products illogical implications. The completeness relation for the c-product must be defined as

$$\frac{|h\rangle\langle\hat{v}| + |v\rangle\langle\hat{h}|}{\langle\hat{v}|h\rangle} = \mathbb{1}_{2 \times 2} . \quad (2.22)$$

The necessary projectors

$$\hat{\Pi}_v = \frac{|\hat{h}\rangle\langle\hat{h}|}{\langle\hat{h}|v\rangle} , \quad \hat{\Pi}_h = \frac{|\hat{v}\rangle\langle\hat{v}|}{\langle\hat{v}|h\rangle} , \quad (2.23)$$

that are needed to extract the coefficients c_v, c_h from a general state vector $|\psi\rangle = c_v|v\rangle + c_h|h\rangle$ are also unintuitive. The projector $\hat{\Pi}_v$ that returns the coefficient c_v when acted on a state $\hat{\Pi}_v|\psi\rangle = c_v$ is composed of $|\hat{h}\rangle$ and the other way around for $\hat{\Pi}_h$. At this point we refrain from using the c-product for the generalized eigenbasis and instead

simply use the standard Dirac inner product $\langle \cdot | := |\cdot \rangle^\dagger$. In [chapter 4](#) we show in general how the Hermitian form $\langle \cdot | \cdot \rangle$ can be extended to be applicable also for non-Hermitian theories.

2.5.2 Projection onto the generalized eigenbasis at the EP

When we use go to the close vicinity of the EP so that the imaginary part of the mixing angle θ get very large, we are interested how the population of an arbitrary state $|\psi(t_0)\rangle$ at time t_0 , that is expanded in the eigenbasis ($|+\rangle, |-\rangle$), is distributed among the generalized eigenbasis at the EP ($|v\rangle, |h\rangle$). The expansion coefficients

$$c_v(t_0) = \langle v | \psi(t_0) \rangle = \frac{e^{-i\theta(t_0)/2}}{\sqrt{2}} (c_-(t_0) - ic_+(t_0)) , \quad (2.24)$$

$$c_h(t_0) = \langle h | \psi(t_0) \rangle = \frac{e^{+i\theta(t_0)/2}}{\sqrt{2}} (c_+(t_0) - ic_-(t_0)) , \quad (2.25)$$

tell that c_v is exponentially amplified whereas c_h is in the same way damped as the imaginary part of θ is always positive.

2.6 Crossing a branch cut

In the mathematical field of monodromy it is well-known that an EP of a 2×2 matrix always has $\text{codim}(\text{EP}_2) = 2$. This entails that by varying two real parameters in the Hamiltonian along a closed contour one can unambiguously say whether an EP has been enclosed or not. Such dynamical parameter loops can be carried out in the time domain by making any two of $\{g, \omega, \gamma\}$ time dependent and periodic, e.g. $g = g(t), \omega = \omega(t)$ with $g(0) = g(T)$ and $\omega(0) = \omega(T)$ where T is the period.

Such a periodic loop (encirclement) that encloses one EP has the intriguing feature that the eigenvalues and eigenvectors do not return to their initial values after one period. In case of the eigenvalues, this is already evident in the self-intersecting Riemann sheets (see [Fig. 2.1](#)).

2.6.1 Eigenvalue flip

At first, we are showing the 4π -symmetry of the eigenvalues when the EP is enclosed in a closed contour.

For convenience we first define $\xi = \omega + i\gamma/2 \in \mathbb{C}$ and then recall that the eigenvalues of our model Hamiltonian are $\lambda_\pm = \pm \sqrt{(\omega + i\gamma/2)^2 + g^2} = \pm \sqrt{\xi^2 + g^2}$. The fact that the complex square root has a branch cut along the negative real axis, $z \in (-\infty, 0]$, is responsible for the 4π -symmetry of the eigenvalues upon encircling an EP. If the EP is excluded from a closed contour then the eigenvalues show a regular 2π -symmetry.

Before we can show the 4π -symmetry, we must denote the defining properties of the principal square root function. Let $z = re^{i\phi}$ with $\phi \in (-\pi, \pi]$ then the principal branch of the square root is defined as $\sqrt{z} = \sqrt{r}e^{i\phi/2}$. Analytic continuation across the branch

cut ($\phi = \pi$) requires an additional phase factor

$$\sqrt{ze^{2i\pi}} = e^{i\pi} \sqrt{z} \quad (2.26)$$

as the square root is multivalued along this line. The factor $e^{i\pi}$ in Eq. 2.26 means that a closed contour that passes the branch cut only once transforms the square root according to $\sqrt{z} \rightarrow e^{i\pi} \sqrt{z}$. We state here already that the defining property of an EP-enclosing loop is that the branch cut is only passed once resulting in an eigenvalue flip.

To prove this, we must show that the branch cut of the eigenvalues $\sqrt{(\omega + i\gamma/2)^2 + g^2}$ extends from one EP to the other. This is done by searching for the parameter regions where the argument of the square root becomes purely real and negative, which leads to the defining equation for the branch cut

$$g^2 - \frac{\gamma^2}{4} \leq 0 \Rightarrow -\frac{\gamma}{2} \leq g \leq \frac{\gamma}{2} . \quad \square$$

This completes the proof that the branch cut of the eigenvalues extends from one EP to the other. The difference in the symmetry for EP-enclosing and non-enclosing loops is visualized in Fig. 2.2. The left panel (a) shows one rectangular parameter path that encloses (green line) the EP and one that does not (cyan line). In panel (b) the value of λ_+ along the path is shown for both loops. The eigenvalues clearly only gather a phase of π along a degeneracy enclosing loop ($\lambda_+(0) = -\lambda_+(T)$).

2.6.2 Eigenvector flip

The eigenvectors also undergo a flip for the same reason as the eigenvalues do, namely passing of a branch cut, but this flip results in a 8π -symmetry. As we are using the atan2 , the mixing angle $\theta = \arctan(-g/\xi)$ has its branch cut also along the line $\omega = 0 \wedge -\gamma/2 \leq g \leq \gamma/2$ that connects the two EPs. The value of θ changes by $\pm\pi$ along the branch cut depending on the passing direction, e.g. by choosing a loop in $\{g, \omega\}$ we find that

$$\lim_{\omega \rightarrow 0^+} \theta - \lim_{\omega \rightarrow 0^-} \theta = -\pi . \quad (2.27)$$

Again, only loops that enclose exactly one EP cross the branch cut only once and are subject to an eigenvector flip. A change of $\pm\pi$ in θ leads to a swap of $\cos(\theta/2)$ with $\sin(\theta/2)$ along with a sign change in one of them. The eigenbasis ($|+\rangle, |-\rangle$) hence undergoes the following 8π -symmetric pattern for clockwise (cw) and counter-clockwise (ccw) loops

$$\begin{aligned} \text{cw: } & \begin{array}{ccccccc} |+\rangle & \xrightarrow{2\pi} & |-\rangle & \xrightarrow{4\pi} & -|+\rangle & \xrightarrow{6\pi} & -|-\rangle & \xrightarrow{8\pi} & |+\rangle \\ |-\rangle & & -|+\rangle & & -|-\rangle & & |+\rangle & & |-\rangle \end{array} , \\ \text{ccw: } & \begin{array}{ccccccc} |+\rangle & \xrightarrow{2\pi} & -|-\rangle & \xrightarrow{4\pi} & -|+\rangle & \xrightarrow{6\pi} & |-\rangle & \xrightarrow{8\pi} & |+\rangle \\ |-\rangle & & |+\rangle & & -|-\rangle & & -|+\rangle & & |-\rangle \end{array} . \end{aligned} \quad (2.28)$$

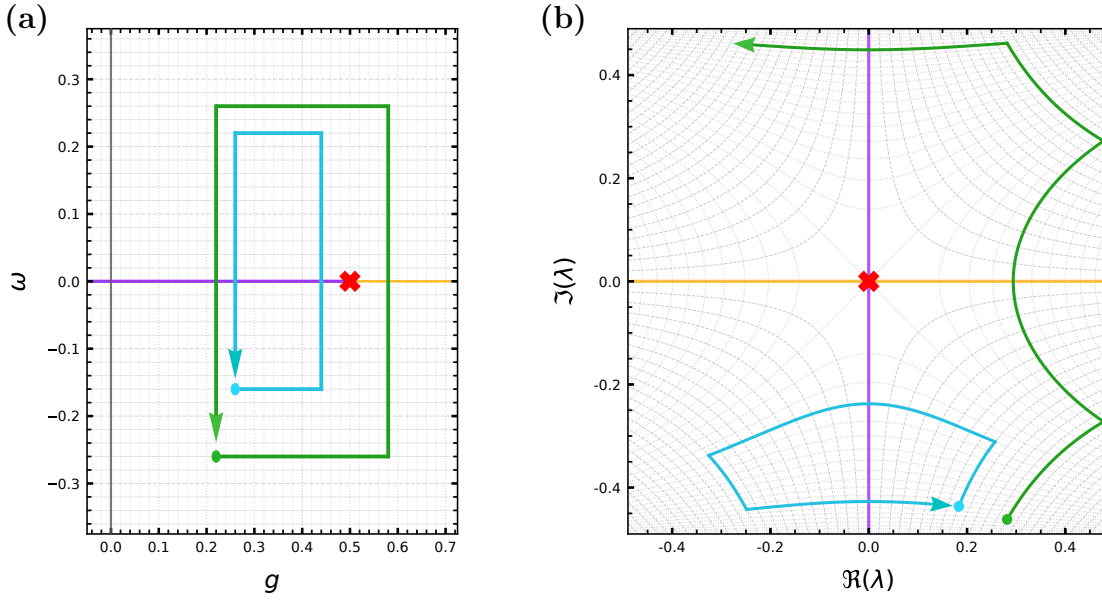


Figure 2.2: Periodicity of the eigenvalues for EP enclosing and non-enclosing loops under rectangular parameter variations in (g, ω) . The EP is depicted with a red cross. (a) Two rectangular parameter paths in $\{g, \omega\}$ -space that are enclosing (green) and not enclosing (cyan) the EP. (b) The eigenvalue $\lambda_+(t)$ in the complex plane along the paths defined in (a). The non-enclosing trajectory (cyan) returns to itself $\lambda(0) = \lambda(T)$ whereas the EP enclosing loop (green) gathers a minus sign $\lambda(0) = -\lambda(T)$. The purple line symbolizes the real crossing and the orange line the imaginary crossing of the complex eigenvalues.

We present this switch for a ccw loop in Fig. 2.3 in a similar fashion as before. In panel (a) we depict the EP-enclosing parameter path and in panel (b) the corresponding trajectory of the first and second component of the eigenvectors $|-\rangle$ and $|+\rangle$. Each color corresponds to one ccw loop shown in (a) where the disks mark the initial position and the arrowheads the final position in the complex plane. This nicely demonstrates the 8π -symmetry of the eigenvectors.

This flip behavior for an enclosing loop can be accounted for by acting with $\pm i\sigma_y$ on the eigenvectors after each loop, where the $+$ sign is related to cw propagation direction.

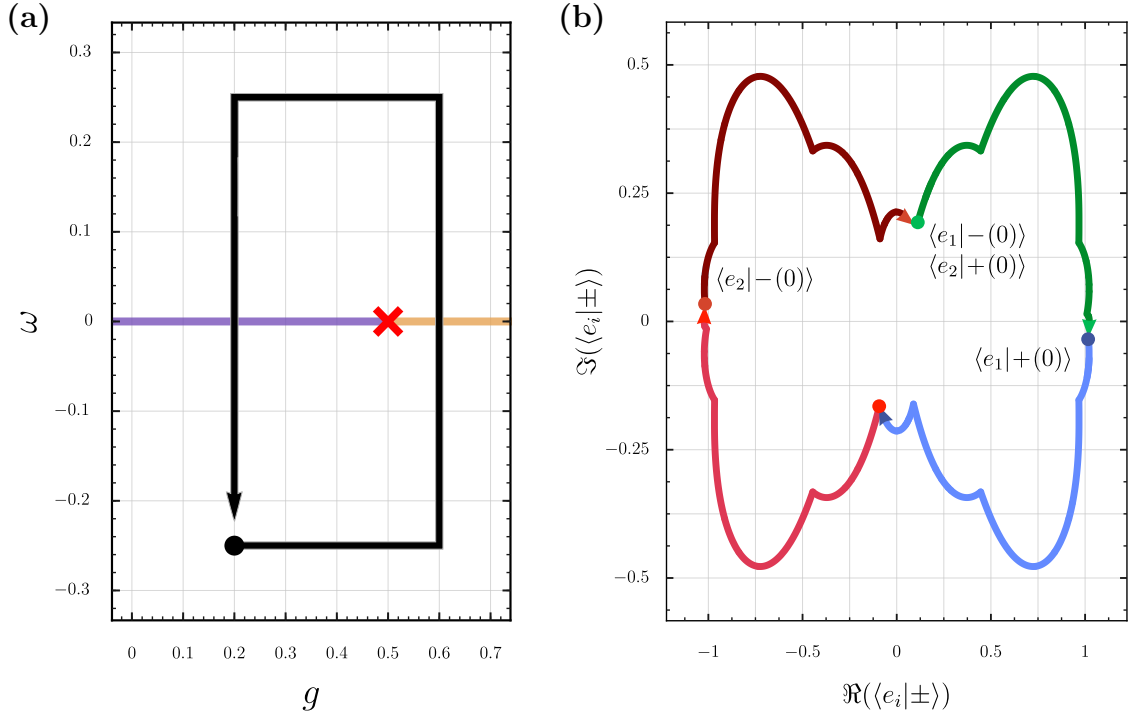


Figure 2.3: Periodicity of the eigenvectors for an EP-enclosing ccw loop using rectangular parameter variations in (g, ω) . (a) The rectangular parameter path (black line) in the $\{g, \omega\}$ -plane that encloses the EP. The EP is depicted with a red cross. The purple line symbolizes the real crossing and the orange line the imaginary crossing. (b) The first $(\langle e_1 | \cdot \rangle)$ and second component $(\langle e_2 | \cdot \rangle)$ of the eigenvectors $|\pm\rangle$ in the complex plane. Every colored line corresponds to one loop around the EP hence four loops are required to come back to the initial states showing explicitly the 8π -symmetry.

2.7 Going through the EP

Although the behavior of the eigenvectors upon encircling an exceptional point is extensively discussed in the literature [11, 24–26, 30, 31], the behavior of the eigenbasis when going through the EP is not. To study the behavior of the eigenvectors more thoroughly we look now at the behavior of the mixing angle θ when we go through an EP. Instead of a gain of $\pm\pi$ as for the branch cut, the height of the discontinuity at the EP is only $\pm\pi/2$,

$$\lim_{\omega \rightarrow 0^\pm} \theta - \lim_{\omega \rightarrow 0^\mp} \theta = \mp\pi/2. \quad (2.29)$$

In this case the matrix that accounts for this flip is

$$\frac{1}{\sqrt{2}}(\sigma_0 \mp i\sigma_y), \quad (2.30)$$

which becomes the identity only after eight turns. The transformation of the basis vectors leads to the sequence

$$\begin{array}{l} |+\rangle \\ |-\rangle \end{array} \xrightarrow{(1)} \begin{array}{l} (|+\rangle + |-\rangle)/\sqrt{2} \\ (|-\rangle - |+\rangle)/\sqrt{2} \end{array} \xrightarrow{(2)} \begin{array}{l} |-\rangle \\ -|+\rangle \end{array} \xrightarrow{(3)} \begin{array}{l} (|-\rangle - |+\rangle)/\sqrt{2} \\ -(|+\rangle + |-\rangle)/\sqrt{2} \end{array} \xrightarrow{(4)} \begin{array}{l} -|+\rangle \\ -|-\rangle \end{array} \quad (2.31)$$

that has a global minus sign after four passages. Note that across the branch cut we applied σ_y and the basis became continuous. Here we realize that the basis vectors mix after the EP and are therefore not eigenvectors of the Hamiltonian anymore

$$H \left(\frac{\pm|+\rangle + |-\rangle}{\sqrt{2}} \right) = \lambda \left(\frac{\pm|+\rangle - |-\rangle}{\sqrt{2}} \right). \quad (2.32)$$

In fact, there is no eigenbasis that can be continuously evolved in time when going through an EP. The appearing phase jump of $\pm\pi/2$ was also discussed in [34].

3 Time evolution operator $U(t)$ in the instantaneous eigenbasis of $H(t)$

To get a better understanding of the appearing effects of dynamically changing parameters in the Hamiltonian during the evolution ($H = H(t)$) we transform the Hamiltonian to its eigenbasis. The time dependence of the Hamiltonian implies that the Schrödinger equation (SE) for the time evolution operator $U(t)$ is not diagonal in the eigenbasis of H . If a state vector $\psi(t)$ fulfills a Schrödinger type equation (Eq. 2.1) then the associated time evolution operator $U(t)$ obeys the same dynamical equations

$$i\partial_t U(t) = H(t)U(t) . \quad (3.1)$$

3.1 Time dependent similarity transformations

In this section we show in general how the Schrödinger equation transforms under a similarity transformation of the Hamiltonian $H(t)$ if the change of basis matrix $S(t)$ is time dependent. For some invertible matrix $S(t)$ we define the matrix $D(t)$ to be similar⁵ to $H(t)$

$$D(t) = S^{-1}(t)H(t)S(t) . \quad (3.2)$$

Now we transform the Schrödinger equation for the time evolution operator (Eq. 3.1) to the basis $S(t)$ by multiplying $S^{-1}(t)$ from the left and $S(0)$ from the right

$$S^{-1}(t)\dot{U}(t)S(0) = -iD(t)\tilde{U}(t) ,$$

where we use $\tilde{U}(t) = S^{-1}(t)U(t)S(0)$ to denote the representation in the basis $S(t)$. The right-hand side is finished, but on the left side we need to put the derivative up front

$$\frac{d}{dt} (S^{-1}(t)U(t)S(0)) = \left(\frac{d}{dt} S^{-1}(t) \right) U(t)S(0) + S^{-1}(t) \left(\frac{d}{dt} U(t) \right) S(0) ,$$

which produces an additional term that includes the derivative of $S^{-1}(t)$. After reordering and putting everything together the differential equation for $\tilde{U}(t)$ becomes

$$\frac{d}{dt} \tilde{U}(t) = \left[\left(\frac{d}{dt} S^{-1}(t) \right) S(t) - iD(t) \right] \tilde{U}(t) = -i\tilde{H}(t)\tilde{U}(t) , \quad (3.3)$$

⁵ $D(t)$ is only diagonal in the eigenbasis of $H(t)$

where the Hamiltonian $\tilde{H}(t)$, that governs the time evolution of $\tilde{U}(t)$ in the basis $S(t)$, is given as

$$\tilde{H}(t) = D(t) + i \left(\frac{d}{dt} S^{-1}(t) \right) S(t). \quad (3.4)$$

Equation 3.3 displays in general how the Schrödinger equation for the time evolution operator⁶ $\tilde{U}(t) = S^{-1}(t)U(t)S(0)$ transforms under a similarity transformation of $H(t)$ using a (invertible) time dependent basis $S(t)$ with $D(t) = S^{-1}(t)H(t)S(t)$. Even though we have denoted the transformed operator in the basis $S(t)$ with $\tilde{H}(t)$ we want to stress here that $\tilde{H}(t)$ is not similar to $H(t)$ anymore, i.e. H and \tilde{H} do not have the same eigenvalue spectrum.

3.2 Schrödinger equation in the eigenbasis of the Hamiltonian

The result from the previous section can be readily applied to transform Eq. 3.1 to the eigenbasis of H (Eq. 2.3) by using $S(t) = (|-\rangle, |+\rangle)$ and $D(t) = \text{diag}(-\lambda, \lambda)$

$$\begin{aligned} \left(\frac{d}{dt} S^{-1}(t) \right) S(t) &= \frac{d}{dt} \begin{pmatrix} \cos(\theta/2) & \sin(\theta/2) \\ -\sin(\theta/2) & \cos(\theta/2) \end{pmatrix} \cdot \begin{pmatrix} \cos(\theta/2) & -\sin(\theta/2) \\ \sin(\theta/2) & \cos(\theta/2) \end{pmatrix} = \\ &= \frac{\dot{\theta}(t)}{2} \begin{pmatrix} 0 & 1 \\ -1 & 0 \end{pmatrix} = i \begin{pmatrix} 0 & f(t) \\ -f(t) & 0 \end{pmatrix} \end{aligned} \quad (3.5)$$

with $f(t) = -i\dot{\theta}(t)/2$. By inserting Eq. 3.5 into Eq. 3.3 the Schrödinger equation for $U(t)$ in the eigenbasis of $H(t)$,

$$\partial_t \tilde{U}(t) = -i\tilde{H}(t)\tilde{U}(t) = -i \begin{pmatrix} -\lambda(t) & -f(t) \\ f(t) & \lambda(t) \end{pmatrix} \tilde{U}(t), \quad (3.6)$$

we find that the effective Hamiltonian \tilde{H} is not diagonal [43]. The additional term $i\dot{S}^{-1}(t)S(t)$ in Eq. 3.4 that produces the off-diagonal components accounts for the changing basis vectors during the propagation. This inevitably couples the two eigenvectors. Since the case $f(t) = 0$ ($\dot{S}(t) = 0$) results in an adiabatic time evolution, the function $f(t)$ is a measure for non-adiabaticity. The coupling $f(t)$

$$f(t) = \frac{\dot{\theta}(t)}{2i} = \frac{g(t)\dot{\xi}(t) - \dot{g}(t)\xi(t)}{2i(\xi(t)^2 + g(t)^2)} = \frac{g(t)\dot{\xi}(t) - \dot{g}(t)\xi(t)}{2i\lambda(t)^2}, \quad (3.7)$$

contains a derivatives and therefore $|f(t)| \propto 1/T$. One could assume that slow enough loops hence obey the adiabatic theorem. It turns out though that for a non-Hermitian

⁶The transformation law for the coefficient vector $\psi(t)$ is congeneric and the resulting dynamical equation also includes the additional term $\dot{S}^{-1}(t)S(t)$.

Hamiltonian the coupling $f(t)$ is singularly perturbing the system and the time evolution has inevitably non-adiabatic contributions. Also the square of the eigenvalue in the denominator explains the divergence of $f(t)$ at the EP ($\lambda = 0$).

The Schrödinger equation for the coefficient vector $(c_-(t), c_+(t))^T$ of a state vector $|\psi(t)\rangle = c_-(t)|-(t)\rangle + c_+(t)|+(t)\rangle$ in the basis $S(t)$ is also given by Eq. 3.6 when $\tilde{U}(t) \rightarrow \psi(t) = (c_-(t), c_+(t))^T$.

3.3 Special solutions for $\tilde{U}(t)$

3.3.1 Stationary time evolution

In the case of constant parameters g , ω and γ we get $f(t) = 0$ as the mixing angle θ becomes constant $\theta(t) = \text{const}$. The initial condition $U(0) = \mathbb{1}$ then implies that the stationary time evolution operator is diagonal

$$\tilde{U}_{\text{stat}}(t) = \begin{pmatrix} e^{+i\lambda t} & 0 \\ 0 & e^{-i\lambda t} \end{pmatrix}. \quad (3.8)$$

A state vector thereafter evolves according to $|\psi(t)\rangle = \sum_{m=\{-,+\}} c_{0,m} \exp(-mi\lambda t) |k(t)\rangle$. The eigenvalues λ are in general complex and since we are in a frame with relative gain and loss one eigenmode is always amplified whereas the other mode is always damped in the same manner.

The population inversion $p_I = (|c_+|^2 - |c_-|^2) / (|c_+|^2 + |c_-|^2) \in [-1, 1]$ is a normalized measure of the overall population distribution among the two basis vectors. For the stationary time evolution we can bring p_I into the form of a *logistic function* (also *Fermi-Dirac distribution*),

$$p_I = 1 - \frac{2|c_{0,-}|^2}{|c_{0,-}|^2 + e^{4\Im(\lambda)t}|c_{0,+}|^2} = 1 - 2 \frac{1}{1 + \exp\left(4\Im(\lambda) \left[t - \ln\left(\frac{|c_{0,-}|}{|c_{0,+}|}\right) / (2\Im(\lambda))\right]\right)}. \quad (3.9)$$

If, without loss of generality, we assume $\Im(\lambda) > 0$, then $|+\rangle$ is the gain state for all times. Consequently, for every initial condition $|c_{0,+}| \neq 0$ the asymptotic solution tends towards $p_I \rightarrow 1$. The midpoint t^* of the logistic function is located at

$$t^* = \frac{1}{2\Im(\lambda)} \ln\left(\frac{|c_{0,-}|}{|c_{0,+}|}\right), \quad (3.10)$$

which has a positive solution for all starting positions with $|c_{0,-}| > |c_{0,+}|$. This time t^* can be thought of as a transition time of the system from $|-\rangle$ to $|+\rangle$. The transition speed only depends on $\Im(\lambda)$.

3.3.2 Time evolution in the vicinity of the EP

At the EP the eigenvalues coalesce and vanish $\lambda_+ = \lambda_- = 0$. The real part of the coupling $f(t)$ diverges at the EP and tends towards $\pm\infty$ depending on the passing direction whereas the imaginary part goes to zero. When we assume a parameter path that is close to the EP we can set $\lambda = 0$ for which the solution of $\tilde{U}(t)$ in Eq. 3.6 is

$$\tilde{U}_{\text{EP}}(t) = \begin{pmatrix} \cosh(\int_0^t f(t')dt') & i \sinh(\int_0^t f(t')dt') \\ -i \sinh(\int_0^t f(t')dt') & \cosh(\int_0^t f(t')dt') \end{pmatrix}. \quad (3.11)$$

The argument of the hyperbolic trigonometric functions in \tilde{U}_{EP} depends only on $f(t)$, which has a large real part at the EP. For arguments z with a large real part $\Re(z) \gg 1$ the absolute values of the hyperbolic sine and cosine are almost the same and we can further approximate Eq. 3.11 by

$$\tilde{U}_{\text{EP}}(t) \approx \cosh\left(\int_0^t |f(t')|dt'\right) \begin{pmatrix} 1 & \pm i(1 - \varepsilon) \\ \mp i(1 - \varepsilon) & 1 \end{pmatrix}. \quad (3.12)$$

For $\varepsilon \rightarrow 0$ (at the EP) the eigenvectors are perfectly leveled with a phase difference of $\pm\pi$ that depends on the passing direction $c_-/c_+ = \pm i$.

This brings us to the conclusion that the EP equalizes the eigenvector populations through a diverging non adiabatic coupling $f(t)$. The coupling depends on the loop time T and the distance to the EP (via λ^2) in parameter space. Through the ratio $c_-/c_+ = \pm i$ it is also clear that the EP imposes a certain relative phase relation on the eigenvectors.

3.3.3 Adiabatic prediction

Assuming adiabaticity, we can set $f(t) = 0$, but this time $\lambda(t)$ is time dependent. This gives us the adiabatic time evolution operator

$$\tilde{U}_{\text{ad}}(t) = \begin{pmatrix} \exp\left(+i \int_0^t \lambda(t')dt'\right) & 0 \\ 0 & \exp\left(-i \int_0^t \lambda(t')dt'\right) \end{pmatrix}. \quad (3.13)$$

The adiabatic theorem suggests that for an infinitely slow change of the parameters in the Hamiltonian the instantaneous eigenstates are continuously transformed into each other without a leak from one eigenstate to the other as the off-diagonal elements of \tilde{U}_{ad} are zero. However, since the Hamiltonian is non-Hermitian the eigenstates themselves are not orthogonal⁷ in the first place and therefore a change of basis through a change of parameters (g, ω or γ) will inevitably lead to a mixing in the population of the eigenmodes.

⁷The basis states are just orthogonal using the c-product $\langle \hat{-}|+\rangle = \langle \hat{+}|-\rangle = 0$.

3.3.4 Coupled adiabatic time evolution

Without proof we note that for an initial eigenstate it is possible that either c_+ or c_- encounters an evolution that follows the adiabatic prediction [26, 30, 31]. The other component is however always populated through the nonzero coupling $f(t)$. A suitable ansatz for a general infinitesimal time evolution operator is therefore to equip the adiabatic prediction of Eq. 3.13 with the coupling from \tilde{U}_{EP} in Eq. 3.11. The resulting non-adiabatic infinitesimal time evolution operator

$$\tilde{U}_{\text{nad}}(t + dt, t) = \begin{pmatrix} \exp(+i\lambda(t)dt) \cosh(f(t)dt) & +i \sinh(f(t)dt) \\ -i \sinh(f(t)dt) & \exp(-i\lambda(t)dt) \cosh(f(t)dt) \end{pmatrix} + \mathcal{O}(t^3) \quad (3.14)$$

is exact up to orders of t^2 (without proof). Furthermore the non-adiabatic extension can be put together as infinitesimal successive steps of \tilde{U}_{ad} and \tilde{U}_{EP}

$$\tilde{U}_{\text{nad}}(t + dt, t) = \tilde{U}_{\text{ad}}\left(t + \frac{dt}{2}, t\right) \tilde{U}_{\text{EP}}(t + dt, t) \tilde{U}_{\text{ad}}\left(t + \frac{dt}{2}, t\right). \quad (3.15)$$

Although this is just an approximation for the exact infinitesimal time evolution operator, this result shows that the overall evolution consists of an adiabatic evolution \tilde{U}_{ad} mixed with a non-adiabatic coupling as if the modes were degenerate \tilde{U}_{EP} . This also explains why only one of the modes can behave adiabatic, namely when the imaginary part of λ is negative for most of the loop and the coupling is sufficiently small.

4 Generalized Hermitian form

Throughout the literature the c-product is endorsed for its comfortable properties that resemble the Dirac formalism up to some extent [1]. In fact, for symmetric Hamiltonians the dual vectors $\langle x_i^* |$ to a given basis $|x_i\rangle$ can be chosen to be the transposed vectors $\langle x_i^* | = |x_i\rangle^T$, which we denote as $\langle \hat{\cdot} | := |\cdot\rangle^T$. This formalism has to be dropped though when the Hamiltonian is not symmetric [4, 44, 45], rendering the c-product inapplicable. Moreover, the self-orthogonality of the generalized eigenbasis at the EP is another indication that the c-product is by no means a natural extension to the Dirac formalism.

In this chapter we thus take a look at the general (Dirac) Hermitian form $\langle \cdot | \cdot \rangle$ with $\langle \cdot | := |\cdot\rangle^\dagger$ and seek a way to extend this well-established formalism to the non-Hermitian domain. In particular we start with a Hamiltonian of the form

$$H = H_1 + iH_2 = \begin{pmatrix} -\omega & g \\ g & \omega \end{pmatrix} + i \begin{pmatrix} -\gamma & 0 \\ 0 & \gamma \end{pmatrix} \quad (4.1)$$

where $H_1 = H_1^\dagger$ and $H_2 = H_2^\dagger$ are real Hermitian operators, but the combined operator $H \neq H^\dagger$ is not. The more general asymmetric Hamiltonians are then discussed in [section 4.8](#).

4.1 Biorthogonality using the c-product

At first we want to show that the use of the c-product results in a biorthogonal basis for non-degenerate eigenvalues. The eigenvalue problem for H

$$(H - \lambda_i I) |x_i\rangle = 0, \quad i = -, + \quad (4.2)$$

is multiplied with $\langle \hat{x}_j |$ from the left and repeated for interchanged i and j

$$\langle \hat{x}_j | (H - \lambda_i I) |x_i\rangle = 0 \quad (4.3)$$

$$\langle \hat{x}_i | (H - \lambda_j I) |x_j\rangle = 0. \quad (4.4)$$

Now we transpose [Eq. 4.4](#) and subtract it from [Eq. 4.3](#)

$$(\lambda_j - \lambda_i) \langle \hat{x}_j | x_i \rangle = 0. \quad (4.5)$$

For non-degenerate eigenvalues $\lambda_i \neq \lambda_j$ the eigenvectors are orthogonal using the c-product. In the case of $i = j$ we can normalize each eigenvector, which gives us a

biorthogonal basis. This does not come as a surprise when we take a look at the transformation matrix S and its inverse S^{-1} from [chapter 3](#). Since S is an orthogonal matrix ($S^{-1} = S^T$) it is clear that the c-product constitutes a biorthogonal basis

$$\langle \hat{x}_j | x_i \rangle = \delta_{ji} \quad (4.6)$$

with the standard completeness relation

$$\sum_j |x_j\rangle\langle \hat{x}_j| = \mathbb{1} . \quad (4.7)$$

The projectors Π_i for each eigenstate

$$\Pi_i = |x_i\rangle\langle \hat{x}_i| . \quad (4.8)$$

that result from the c-product are in fact very useful when computing expansion coefficients for symmetric Hamiltonians.

One setback is the calculation of left state vectors $\langle \hat{\psi} |$ that are needed to calculate overlap distances. They take an unnatural form

$$|\Psi\rangle = \sum_i c_i |x_i\rangle \longrightarrow \langle \hat{\Psi}| = \sum_i c_i^* \langle \hat{x}_i| = \sum_i (\langle \hat{x}_i | \Psi \rangle)^* \langle \hat{x}_i| , \quad (4.9)$$

as they require a separate calculation of the expansion coefficients c_i .

4.2 Non-orthogonality using the Hermitian form

One might ask why adding a small complex contribution iH_2 to a Hermitian Hamiltonian H_1 should result in abandoning a well-established concept of Hermitian quantum mechanics, namely the Hermitian form. There must be a simple way to see why the standard Hermitian form is not applicable anymore in case of $\gamma \neq 0$.

This time we act with $\langle x_j |$ on the eigenvalue equation [Eq. 4.2](#)

$$\langle x_j | (H - \lambda_i I) | x_i \rangle = \langle x_j | (H_1 + iH_2 - \lambda_i I) | x_i \rangle = 0 . \quad (4.10)$$

In the next step we interchange i and j again, but this time we conjugate transpose the interchanged equation

$$\langle x_j | (H^\dagger - \lambda_j^* I) | x_i \rangle = \langle x_j | (H_1 - iH_2 - \lambda_j^* I) | x_i \rangle = 0 \quad (4.11)$$

where we have used the symmetry of H_1 and H_2 . Now we can subtract [Eq. 4.11](#) from [Eq. 4.10](#) to get

$$\langle x_j | (2iH_2 - (\lambda_i - \lambda_j^*) I) | x_i \rangle = 0 \quad (4.12)$$

or we can add the two equations

$$\langle x_j | (2H_1 - (\lambda_i + \lambda_j^*)I) | x_i \rangle = 0 , \quad (4.13)$$

so that the inner product

$$\langle x_j | x_i \rangle = 2 \frac{\langle x_j | H_1 | x_i \rangle}{\lambda_i + \lambda_j^*} = 2i \frac{\langle x_j | H_2 | x_i \rangle}{\lambda_i - \lambda_j^*} . \quad (4.14)$$

When we take [Eq. 4.12](#) and separate the cases $i \neq j$ and $i = j$ we find for $i \neq j$

$$\begin{aligned} 2i \langle x_j | H_2 | x_i \rangle + (\lambda_j + \lambda_j^*) \langle x_j | x_i \rangle &= 0 , \\ \langle x_j | H_2 | x_i \rangle + i \Re(\lambda_j) \langle x_j | x_i \rangle &= 0 . \end{aligned} \quad (4.15)$$

Finally, we can write the standard Hermitian form as

$$-i \Re(\lambda_j) \langle x_j | x_i \rangle = \langle x_j | H_2 | x_i \rangle , \quad i \neq j \quad (4.16)$$

and for the case $i = j$ it is straightforward to see that

$$\Im(\lambda_j) \langle x_j | x_j \rangle = \langle x_j | H_2 | x_j \rangle , \quad i = j . \quad (4.17)$$

These equations can be combined to yield

$$\langle x_j | (\Re(\lambda_j)(1 - \delta_{ji}) + i \Im(\lambda_j) \delta_{ji} - i H_2) | x_i \rangle = 0 . \quad (4.18)$$

At this point it becomes apparent that the standard Hermitian form is not suitable to define a biorthogonal basis as it is not possible to have $\langle x_j | x_i \rangle = \delta_{ji}$ from [Eqs. 4.16](#) and [4.17](#).

4.3 Biorthogonality using a generalized Hermitian form

The obvious natural extension to the standard Hermitian form $\langle \cdot | \cdot \rangle$ is to redefine the inner product by inserting an Hermitian operator $B = B^\dagger$ that satisfies

$$\langle x_j | B | x_i \rangle = \delta_{ji} , \quad (4.19)$$

where the Hermiticity of B ensures that $\langle x_j | (B | x_i \rangle) = (\langle x_j | B^\dagger) | x_i \rangle$. The general solution for B can be written in terms of the dual eigenvectors $|x_i^*\rangle$

$$B = \sum_i |x_i^* \rangle \langle x_i^*| . \quad (4.20)$$

This does not come as a surprise since in the finite dimensional case, the dual basis is the set of linear functionals defined by the relation $\langle x_i^* | x_j \rangle = \delta_{ij}$, given that $\langle \cdot | \cdot \rangle$ is a

bilinear map. By solving the defining equation for our specific Hamiltonian and the basis defined in Eq. 2.5 one finds that

$$B = \begin{pmatrix} \cosh(\Im(\theta)) & i \sinh(\Im(\theta)) \\ -i \sinh(\Im(\theta)) & \cosh(\Im(\theta)) \end{pmatrix} = \cosh(\Im(\theta))\sigma_0 - \sinh(\Im(\theta))\sigma_y \quad (4.21)$$

fulfills Eq. 4.19, where σ_i are the Pauli matrices. B is in fact an orthogonal Hermitian matrix that is

$$B^T = B^{-1}, \quad B = B^\dagger, \quad (4.22)$$

with $\det(B) = +1$. The form of B is independent of the exact form of the complex frequency ξ or a potential complex coupling $g \in \mathbb{C}$.

The completeness relation for the B -matrix

$$\sum_j B|x_j\rangle\langle x_j| = \sum_j |x_j\rangle\langle x_j|B = \mathbb{1} \quad (4.23)$$

follows from Eq. 4.19. By examining Eq. 4.21 we see that for vanishing damping $\gamma = 0 \Rightarrow \Im(\theta) = 0$ and the matrix B becomes the identity matrix $B|_{\gamma=0} = \mathbb{1}$ in which case Eqs. 4.19 and 4.23 describe the standard Hermitian form of quantum mechanics. This indicates that the generalized Hermitian form

$$\langle \cdot | \cdot \rangle_B := \langle \cdot | B | \cdot \rangle, \quad \langle \cdot | := | \cdot \rangle^\dagger \quad (4.24)$$

is a continuous natural extension to the Hermitian inner product for $\gamma \neq 0$. In the following chapters we will drop the subscript B and use the generalized Hermitian form implicitly, $\langle \cdot | \cdot \rangle \equiv \langle \cdot | \cdot \rangle_B$, if not stated otherwise. For growing values of $\Im(\theta)$ the off-diagonal entries of B grow indicating that the eigenvectors are non-orthogonal in the Hermitian form. When approaching the EP the imaginary part of the mixing angle θ diverges logarithmically to $+\infty$ and the eigenvectors become parallel.

Since the non-orthogonality that is described by B stems only from $\Im(\theta)$ we draw $\Im(\theta(g, \omega))$ with γ being fixed in Fig. 4.1. This figure shows that the eigenvectors are almost orthogonal far off the EP, but by getting to the EP they become more and more parallel.

A remarkable feature of the B matrix approach is that it is dependent on the Hamiltonian of the system and is not universally defined. Therefore the underlying physical system determines how orthogonality, norms, etc. are defined. This resembles a key property of general relativity where the metric has to be obtained from the same equations that also describe the dynamics of the system.

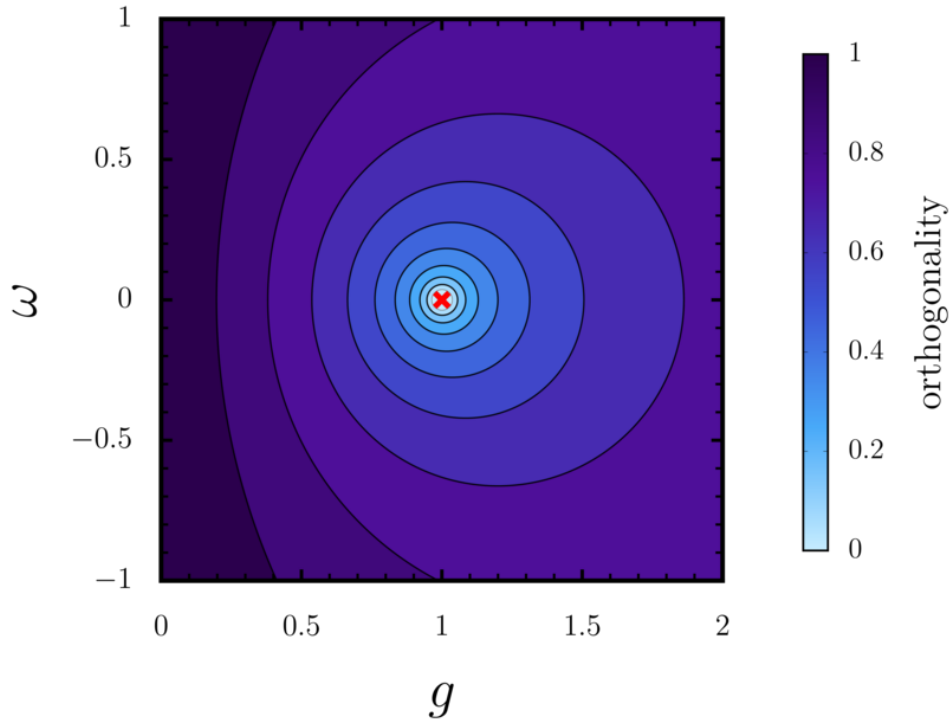


Figure 4.1: Deviation from the identity matrix of the B -matrix and the resulting non-orthogonality of the eigenvectors. The plot shows $\Im(\theta(g, \omega))$ as a function of g and ω . The red cross indicates the EP at $g_{\text{EP}} = \gamma$ and $\omega_{\text{EP}} = 0$ for $\gamma = 1$. The contour lines of $\Im(\theta)$ are circles with radius r that are centered at $\{g = \sqrt{g_{\text{EP}}^2 + r^2}, \omega = 0\}$. Dark purple regions correspond to regions where the eigenvectors $|+\rangle, |-\rangle$ are orthogonal and the light blue colors indicate that the eigenvectors are getting parallel using the standard Hermitian form.

4.3.1 Effect of B on eigenvectors

We already know that the c-product constitutes a biorthogonal basis with $\langle \hat{x}_i | x_j \rangle = \delta_{i,j}$ and it is obvious that the complex conjugate⁸ relation holds as well

$$(\langle \hat{x}_i | x_j \rangle)^* = \langle x_i | (|x_j\rangle)^* = \langle x_i | \bar{x}_j \rangle = \delta_{i,j} \quad (4.25)$$

because $\langle \hat{x}_i | = (\langle x_i |)^*$. Here we have defined $|\bar{\cdot}\rangle := |\cdot\rangle^*$. An analogous thought as before then leads to the question which operator B acts as a complex conjugate on our basis vectors

$$|\bar{x}_i\rangle = B|x_i\rangle \quad (4.26)$$

⁸Complex conjugation is designated with a surrounding superscript $|\cdot\rangle^*$ whereas dual vectors are denoted as $|\cdot^*\rangle$

and the unique solution⁹ for this is again given by the same operator B from Eqs. 4.20 and 4.21. Note that B acts only on the eigenvectors as a complex conjugate. This becomes evident when we apply B on a general state vector $|\Psi\rangle = \sum_i \Psi_i |x_i\rangle$ where the Ψ_i are complex expansion coefficients

$$B|\Psi\rangle = \sum_i \Psi_i B|x_i\rangle = \sum_i \Psi_i |\bar{x}_i\rangle \quad (4.27)$$

4.4 Inner product using generalized Hermitian form

A major benefit of the B -matrix is the calculation of inner products for state vectors $|\Psi\rangle$ as we can use the Hermitian conjugate $\langle\Psi|$

$$\begin{aligned} \langle\Psi|B|\Psi\rangle &= \left(\sum_i \langle x_i | \Psi_i^* \right) B \left(\sum_j \Psi_j |x_j\rangle \right) = \left(\sum_i \langle x_i | \Psi_i^* \right) \left(\sum_j \Psi_j |\bar{x}_j\rangle \right) \\ &= \sum_{i,j} \Psi_i^* \Psi_j \langle x_i | \bar{x}_j \rangle = \sum_{i,j} \Psi_i^* \Psi_j \delta_{i,j} = \sum_i |\Psi_i|^2. \end{aligned} \quad (4.28)$$

This also works for the inner product of two general states $|\Psi\rangle = \sum_i \Psi_i |x_i\rangle$ and $|\Phi\rangle = \sum_i \Phi_i |x_i\rangle$ that are expanded in the same basis

$$\begin{aligned} \langle\Phi|B|\Psi\rangle &= \left(\sum_i \Phi_i^* \langle x_i | \right) B \left(\sum_j \Psi_j |x_j\rangle \right) \\ &= \sum_{i,j} \Phi_i^* \Psi_j \langle x_i | \bar{x}_j \rangle = \sum_i \Phi_i^* \Psi_i. \end{aligned} \quad (4.29)$$

The absolute square of this inner product

$$|\langle\Phi|B|\Psi\rangle|^2 = \sum_i |\Psi_i|^2 |\Phi_i|^2 + \sum_{\substack{i,j \\ i \neq j}} \Psi_i^* \Phi_i \Psi_j \Phi_j^* \quad (4.30)$$

then shows the necessary interference term.

4.4.1 Inner product for different bases

In order to compare states at different points in parameter space, that is states that are expanded in different bases $|x_i\rangle, |y_i\rangle$, we need to establish how the B -matrix is related to a basis transformation matrix. We stress here that B is not a constant operator, but it depends on the specific values of g, ω and γ and is therefore only pointwise defined. This is denoted with a little subscript that specifies to which basis the operator belongs,

⁹Unique up to a constant matrix that commutes with the Hamiltonian.

e.g. B_x is connected to the basis $|x_i\rangle$.

$$\begin{aligned} \left(\sum_j B_y |y_j\rangle \langle y_j| \right) |\Psi\rangle &= \left(\sum_j B_y |y_j\rangle \langle y_j| \right) \sum_i \Psi_i^{(x)} |x_i\rangle \\ &= \sum_{i,j} \Psi_i^{(x)} |y_j\rangle \langle y_j| B_y |x_i\rangle = \sum_j \left(\sum_i \langle y_j| B_y |x_i\rangle \Psi_i^{(x)} \right) |y_j\rangle = \sum_j \Psi_j^{(y)} |y_j\rangle \end{aligned} \quad (4.31)$$

with $\Psi_j^{(y)} = \sum_i D_{ji}^{(y,x)} \Psi_i^{(x)}$ where $D_{ji}^{(y,x)} = \langle y_j| B_y |x_i\rangle$ is the coordinate transformation matrix from $|x_i\rangle$ to $|y_i\rangle$. Since the basis vectors only depend on θ we are going to label θ as well to connect it with a basis $\theta_x \leftrightarrow |x_i\rangle$. With this we can write $D_{ji}^{(y,x)}$

$$D_{ji}^{(y,x)} = \begin{pmatrix} \cos\left(\frac{\theta_y - \theta_x}{2}\right) & \sin\left(\frac{\theta_y - \theta_x}{2}\right) \\ -\sin\left(\frac{\theta_y - \theta_x}{2}\right) & \cos\left(\frac{\theta_y - \theta_x}{2}\right) \end{pmatrix}, \quad \begin{matrix} j = -, + \\ i = -, + \end{matrix} \quad (4.32)$$

which has the general form of a rotation matrix for complex rotation angles $\alpha = (\theta_y - \theta_x)/2 = \phi_r + i\phi_i$. Here for vanishing imaginary part of the mixing angle ($\Im(\theta) = 0$) the basis transformation matrix $D_{ij}^{(x,y)}$ again simply becomes a rotation matrix about a real angle $\alpha = (\theta_y - \theta_x)/2 \in \mathbb{R}$. Using the results from above we can now calculate the overlap of two different states $|\Psi\rangle = \sum_i \Psi_i^{(x)} |x_i\rangle$ and $|\Phi\rangle = \sum_i \Phi_i^{(y)} |y_i\rangle$ that are not measured in the same basis

$$\begin{aligned} \langle \Phi | B | \Psi \rangle &= \sum_{i,j} \Phi_j^{*(y)} \Psi_i^{(y)} \langle y_j | B_y | y_i \rangle = \sum_{i,j,k} \Phi_j^{*(y)} \Psi_i^{(y)} \langle y_j | B_y | x_k \rangle \langle x_k | B_x | y_i \rangle \\ &= \sum_{i,j,k} \Phi_j^{*(y)} \Psi_i^{(y)} D_{jk}^{(y,x)} D_{ki}^{(x,y)} = \sum_{j,k} \Phi_j^{*(y)} D_{jk}^{(y,x)} \Psi_k^{(x)}. \end{aligned} \quad (4.33)$$

and finally

$$|\langle \Phi | B | \Psi \rangle|^2 = \sum_j |\Phi_j^{(y)}|^2 |\Psi_j^{(y)}|^2 + \sum_{\substack{i,j \\ i \neq j}} \Phi_j^{*(y)} \Psi_j^{(y)} \Psi_i^{*(y)} \Phi_i^{*(y)} \quad (4.34)$$

obtaining a result that is independent of the basis that is used since we can replace $y \leftrightarrow x$.

Properties of $D_{ij}^{(x,y)}$

The basis transformation matrix $D_{ij}^{(x,y)}$ includes the 8π symmetry for closed loops that enclose the EP. And by taking two bases $|x\rangle, |y\rangle$ that are at opposite sides of the EP at a distance ε one finds that $\theta_y - \theta_x|_{\varepsilon \rightarrow 0} = \pi/2$. This relates exactly to the fact that the EP has to be passed eight times to be back at the exact same configuration.

4.5 Contour lines of $\Im(\theta)$

In general, a closed loop around the EP defines a path where the overlap distance between the eigenvectors varies constantly and so the coupling between the states also varies considerably. Therefore we take a look at how parameter paths look along which $\Im(\theta) = \text{const}$. For those special trajectories the coupling $f(t) = -i\dot{\theta}(t)/2$ is then going to be purely imaginary and constant.

The imaginary part of θ can be written as

$$\Im(\theta) = -\ln \left(\frac{\sqrt{(g-\gamma)^2 + \omega^2}}{\sqrt[4]{4\gamma^2\omega^2 + (g^2 - \gamma^2 + \omega^2)^2}} \right) \quad (4.35)$$

and by setting Eq. 4.35 to be constant one finds the defining equation

$$(g - \gamma \cosh(k))^2 + \omega^2 = \gamma^2 \sinh^2(k), \quad k > 0. \quad (4.36)$$

In $\{g, \omega\}$ space this is a circle with radius $r = \gamma \sinh(k)$ and center at $\{\gamma \cosh(k), 0\}$. EP-centered circles with a small radius ($k \ll 1$) are actually trajectories for which the imaginary part of θ stays (almost) constant. With growing radius the center of these circles shifts to larger values of g , which means that such degeneracy-centered circles do not correspond to trajectories with a constant imaginary part of θ and constant coupling f . When fixing the radius of the circle to be r the center of the circle with $\Im(\theta) = \text{const}$ lies at $\{g, \omega\} = \{\sqrt{\gamma^2 + r^2}, 0\}$. The value of $\Im(\theta)$ for such a circular trajectory becomes

$$\Im(\theta) = \ln \left(\frac{\sqrt{2r \left(r + \sqrt{\gamma^2 + r^2} \right)}}{r - \gamma + \sqrt{\gamma^2 + r^2}} \right) = \text{const} \quad (4.37)$$

which is depicted in Fig. 4.2 as a function of the ratio r/γ . At the EP ($r/\gamma \rightarrow 0$) the imaginary part of θ diverges and for very large radii¹⁰ r the imaginary part of θ goes to 0. The real part, however is linearly dependent on time and on the initial starting point on the circle ϕ , but completely independent on r and γ

$$\Re(\theta) = \frac{\pi t}{T} + \frac{\phi - \pi}{2}, \quad -\pi \leq \phi < \pi \quad \wedge \quad 0 \leq t \leq T \quad (4.38)$$

where the range for ϕ stems from the fact that we always take the principal value of complex functions.

Now that we know which trajectories fulfill $\Im(\theta) = \text{const}$ we can take a look at some special properties of such parameter paths. To start, we can take a look at the coordinate

¹⁰Since the center of these circles lies at $\sqrt{r^2 + \gamma^2}$ it is possible for the ratio r/γ to get greater than 1 and it is in fact not limited.

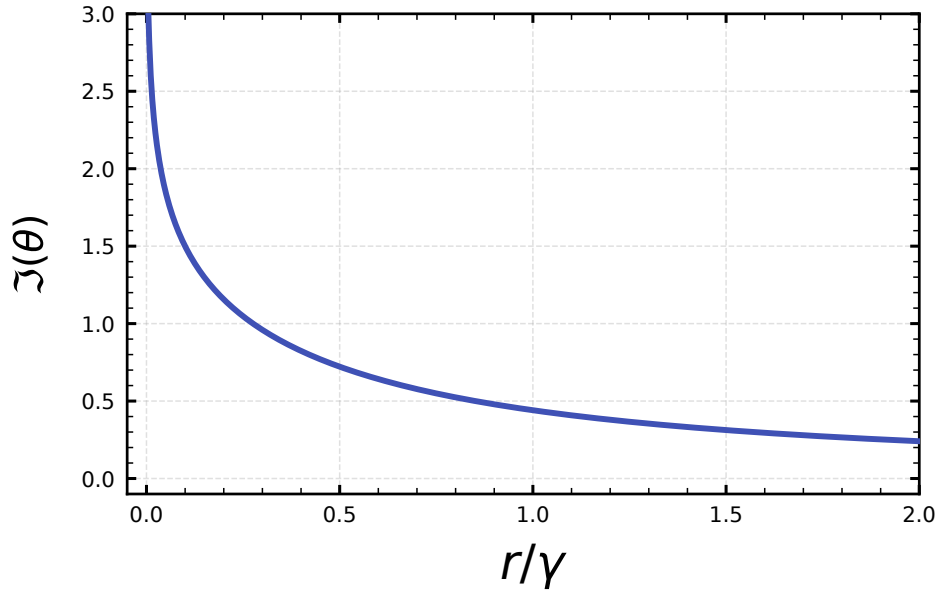


Figure 4.2: Imaginary part of the mixing angle θ as a function of the ratio r/γ for circular trajectories with center at $\{g, \omega\} = \{\sqrt{r^2 + \gamma^2}, 0\}$. The function $\Im(\theta)$ corresponds to the non-orthogonality of the eigenvectors under the standard Hermitian form $\langle \cdot | \cdot \rangle$. It diverges at the EP (eigenvectors become parallel) and goes to zero for $r \rightarrow \infty$ (eigenvectors are orthogonal).

transformation matrix $D_{ij}^{(y,x)}$. The argument of the cosine and sine functions appearing in $D_{ij}^{(y,x)}$ contains the term $(\theta_y - \theta_x)/2$. If the imaginary part of θ does not change this means that $\theta_y - \theta_x = \theta_r \in \mathbb{R}$ and therefore the coordinate transformation matrix $D_{ij}^{(y,x)}$ describes only a rotation.

The derivative of θ simplifies in this special case to $\dot{\theta} = \pi/T$ and since $f = -i\dot{\theta}/2$ we find that $f = -i\pi/(2T)$. The coupling f between the eigenvectors is therefore constant along those parameter loops.

We have shown that there are special parameter loops along which the coupling for the eigenvectors stays constant and only depends on the inverse loop time $1/T$. This means that in the quasi-adiabatic regime ($T \gg 1$) the only time dependent function in the dynamics of the eigenvector populations ($c_-(t), c_+(t)$) or the corresponding time evolution operator $\tilde{U}(t)$ is $\lambda(t)$. This fact has been implicitly used before without consideration [26, 30, 31]. Also, the reason why EP-centered small circles ($r \ll 1$) give particularly easy solutions is exactly due to this effect.

4.6 B -pseudo-Hermiticity

In recent works [5, 46] it has been shown that to every \mathcal{PT} -symmetric time-independent Hamiltonian there exists an operator V that relates H with its adjoint matrix H^\dagger

$$VHV^{-1} = H^\dagger, \quad (4.39)$$

which is called a pseudo-Hermiticity relation with respect to V . In this case the corresponding norm related to V is preserved in time $d_t(\langle \cdot | V | \cdot \rangle) = 0$.

As our operator B is defined for non-Hermitian (time dependent) Hamiltonians with complex energies relation Eq. 4.39 does not hold anymore. Instead we find a more general result

$$BHB^{-1} = \tau H^\dagger \quad (4.40)$$

with

$$\tau = e^{2i \arg \lambda}. \quad (4.41)$$

In the case of real eigenvalues $\lambda \in \mathbb{R} \Rightarrow \tau = 1$ the pseudo-Hermiticity condition is fulfilled. With the help of Eq. 4.40 it follows for the eigenvectors $|x_i\rangle$ with $B|x_i\rangle = |\bar{x}_i\rangle$

$$H^\dagger|\bar{x}_i\rangle = \lambda_i^*|\bar{x}_i\rangle \quad (4.42)$$

where we used $\lambda_i^* = \lambda_i/\tau$. The derivative of the B -norm for an arbitrary time dependent state then yields

$$d_t(\langle \psi | B | \psi \rangle) = i(1 - \tau)\langle \psi | H^\dagger B | \psi \rangle = 2\Im(\lambda) (|c_+|^2 - |c_-|^2) \quad (4.43)$$

for our Hamiltonian with $\lambda = \lambda_+ = -\lambda_-$. The right side of Eq. 4.43 vanishes for $\lambda \in \mathbb{R}$, that is in the \mathcal{PT} -symmetric phase of the model Hamiltonian independent of the initial state. This relation can also be used to define the population inversion p_I in terms of the B -norm since $\langle \psi | B | \psi \rangle = \sum_i |c_i|^2$

$$\frac{d_t \log(\langle \psi | B | \psi \rangle)}{2\Im(\lambda)} = \frac{|c_+|^2 - |c_-|^2}{|c_+|^2 + |c_-|^2} = p_I, \quad (4.44)$$

for parameter regions with $\Im(\lambda) \neq 0$. The B -norm can therefore be used to describe the dynamical evolution of the state vector $\psi_{EB} = (c_-, c_+)^T$ on the Riemann sheets of the eigenvalues as

$$d_t \log \left(\sqrt{\langle \psi | B | \psi \rangle} \right) = \Im(\lambda) \frac{|c_+|^2 - |c_-|^2}{|c_+|^2 + |c_-|^2}, \quad (4.45)$$

where it then comes as no surprise that the B -norm is only preserved for $\Im(\lambda) = 0$.

4.7 B -norm for time dependent Hamiltonians

As our "metric" B is also valid for time dependent Hamiltonians we are now deriving an expression for the time dependence of the B -norm for $H = H(t)$ and $B = B(t)$. The difference to the former case becomes immediately apparent when we expand the derivative of the B -norm

$$d_t (\langle \psi | B | \psi \rangle) = (d_t \langle \psi |) B | \psi \rangle + \langle \psi | B (d_t | \psi \rangle) + \langle \psi | d_t B | \psi \rangle = \quad (4.46)$$

$$= i(1 - \tau) \langle \psi | H^\dagger B | \psi \rangle + \langle \psi | \dot{B} | \psi \rangle \quad (4.47)$$

which now has an additional term $\langle \psi | d_t B | \psi \rangle$ that acts as an interference term. To evaluate it we need to calculate $d_t B$ first

$$d_t B = 2\Re(f) \begin{pmatrix} \sinh(\Im(\theta)) & i \cosh(\Im(\theta)) \\ -i \cosh(\Im(\theta)) & \sinh(\Im(\theta)) \end{pmatrix} \quad (4.48)$$

with $f = -i\theta/2$ being the coupling of the eigenvectors of H (see Eq. 3.6). The effect of $d_t B$ on the eigenvectors is

$$\langle \pm | d_t B | \pm \rangle = 0, \quad \langle \pm | d_t B | \mp \rangle = \mp 2i\Re(f) \quad (4.49)$$

which enables us to rewrite Eq. 4.46 in terms of the eigenbasis as

$$d_t (\langle \psi | B | \psi \rangle) = 2\Im(\lambda) (|c_+|^2 - |c_-|^2) + 2i\Re(f) (c_+ c_-^* - c_-^* c_+) . \quad (4.50)$$

By using the Hamiltonian H_{EB} and the coefficient vector ψ_{EB} in the eigenbasis

$$\psi_{\text{EB}} = (c_-, c_+)^T, \quad H_{\text{EB}} = \begin{pmatrix} -\lambda & -f \\ f & \lambda \end{pmatrix}, \quad (4.51)$$

the normalized B -norm can be written as

$$d_t \log (\langle \psi | B | \psi \rangle) = -i \frac{\psi_{\text{EB}}^\dagger (H_{\text{EB}} - H_{\text{EB}}^\dagger) \psi_{\text{EB}}}{\psi_{\text{EB}}^\dagger \psi_{\text{EB}}} \quad (4.52)$$

which is only zero if $H_{\text{EB}} = H_{\text{EB}}^\dagger$. As Hermiticity is not a property that is preserved under a similarity transformation¹¹ the eigenbasis serves a distinct role here. The result of Eq. 4.52 is also compliant with the preservation of the B -norm for static \mathcal{PT} -symmetric parameter regions with $f = 0$ and $\lambda \in \mathbb{R}$. As a final remark we stress here that in this derivation we have made use of the fact that our eigenbasis is parallel-transported ($\langle \dot{x}_i | B | x_i \rangle = 0$, $i = \pm$).

¹¹To preserve Hermiticity under a similarity transformation accomplished by P it must hold that $P^\dagger = P^{-1}$ which is generally not the case for the transformation to the eigenbasis $S^\dagger \neq S^{-1}$.

4.8 Asymmetric Hamiltonians

To show the universality of the B -matrix approach for the general Hermitian form we apply the same principle to the asymmetric Hamiltonian that is used in [3]

$$H = \begin{pmatrix} re^{i\theta} & s \\ t & re^{-i\theta} \end{pmatrix} \quad (4.53)$$

where r, s, t, θ are real parameters. The eigenvalues and (right) eigenvectors of this Hamiltonian are

$$\lambda_{\pm} = r \cos \theta \pm \sqrt{st - r^2 \sin^2 \theta} = r \cos \theta \pm \sqrt{st} \cos \alpha, \quad (4.54)$$

$$|x_{+}\rangle = \frac{1}{\sqrt{2\sqrt{st} \cos \alpha}} \begin{pmatrix} \sqrt{s} e^{i\alpha/2} \\ \sqrt{t} e^{-i\alpha/2} \end{pmatrix}, \quad |x_{-}\rangle = \frac{1}{\sqrt{2\sqrt{st} \cos \alpha}} \begin{pmatrix} \sqrt{s} e^{-i\alpha/2} \\ -\sqrt{t} e^{i\alpha/2} \end{pmatrix} \quad (4.55)$$

with $r \sin \theta = \sqrt{st} \sin \alpha$. In addition to not being symmetric this Hamiltonian has also non-vanishing trace $\text{Tr}(H) = 2r \cos \theta$. The eigenvalues of H therefore appear only in complex conjugate pairs (λ, λ^*) in the \mathcal{PT} -symmetry broken phase and in real pairs $(\lambda, -\lambda)$ for $\theta = \pi/2, 3\pi/2$ in the \mathcal{PT} -symmetric phase.

By asking which Hermitian operator B satisfies

$$\langle x_i | B | x_j \rangle = \delta_{ij}, \quad (4.56)$$

it follows immediately that the answer can be written in terms of the dual vectors $|x_{\pm}^*\rangle$ as

$$B = |x_{+}^*\rangle \langle x_{+}| + |x_{-}^*\rangle \langle x_{-}| \quad (4.57)$$

if we derive $|x_i^*\rangle$ from the relation $\langle x_i | x_j^* \rangle = \delta_{ij}$. The inverse is then given as $B^{-1} = |x_{+}\rangle \langle x_{+}| + |x_{-}\rangle \langle x_{-}|$. For the sample Hamiltonian one finds that

$$\langle x_{+}^* | = \frac{1}{\sqrt{2\sqrt{st} \cos \alpha}} \begin{pmatrix} \sqrt{t} e^{i\alpha/2} \\ \sqrt{s} e^{-i\alpha/2} \end{pmatrix}, \quad \langle x_{-}^* | = \frac{1}{\sqrt{2\sqrt{st} \cos \alpha}} \begin{pmatrix} \sqrt{t} e^{-i\alpha/2} \\ -\sqrt{s} e^{i\alpha/2} \end{pmatrix} \quad (4.58)$$

so that the left eigenstates are again the transpose of the right ones if $s = t \Rightarrow \alpha \in \mathbb{R}$, that is for a symmetric Hamiltonian. The asymmetry of the Hamiltonian is hence responsible for the necessity of left eigenstates (biorthogonal basis). With the left eigenstates from Eq. 4.58 the B matrix results in

$$B = \frac{1}{\sqrt{\frac{1}{2} (\cosh(2\alpha_i) + \cos(2\alpha_r))}} \begin{pmatrix} \sqrt{\left|\frac{t}{s}\right|} \cosh(\alpha_i) & -i\kappa \sin(\alpha_r) \\ i\kappa^* \sin(\alpha_r) & \sqrt{\left|\frac{s}{t}\right|} \cosh(\alpha_i) \end{pmatrix} \quad (4.59)$$

with $\kappa = e^{\frac{i}{2}(\arg(s) - \arg(t))}$ and $\alpha = \alpha_r + i\alpha_i$. Again, for a Hermitian Hamiltonian ($\alpha = 0$) the matrix B becomes the identity $B = \mathbb{1}$.

The next step is to look at the pseudo-Hermiticity condition

$$BHB^{-1} = \lambda_+ |x_+^* \rangle \langle x_+| + \lambda_- |x_-^* \rangle \langle x_-| = \tilde{H} , \quad (4.60)$$

so the eigenvectors of \tilde{H} are the conjugate transpose left eigenvectors for the same eigenvalues λ_{\pm}

$$\tilde{H} |x_{\pm}^* \rangle = \lambda_{\pm} |x_{\pm}^* \rangle . \quad (4.61)$$

For the comparison of \tilde{H} and H in this more general case where the eigenvalues do not necessarily appear in pairs we introduce an operator C that relates \tilde{H} with H^{\dagger}

$$CH^{\dagger} = (\tau_+ |x_+^* \rangle \langle x_+| + \tau_- |x_-^* \rangle \langle x_-|) (\lambda_+^* |x_+^* \rangle \langle x_+| + \lambda_-^* |x_-^* \rangle \langle x_-|) = \tilde{H} \quad (4.62)$$

with $\tau_j = e^{2i \arg \lambda_j}$. For the traceless Hamiltonian τ was the same for both eigenvalues and so $C = \tau \mathbb{1}$. The B -pseudo Hermiticity relation finally takes the form

$$BHB^{-1} = CH^{\dagger} \quad (4.63)$$

and we see that also in the case of non-symmetric Hamiltonians the pseudo-Hermiticity is only upheld for a purely real eigenvalue spectrum since for $\lambda_{\pm} \in \mathbb{R} \Rightarrow \tau_{\pm} = 1 \Rightarrow C = \mathbb{1}$. The operators C and H^{\dagger} have the same eigenvectors as \tilde{H} so it holds that

$$C |x_{\pm}^* \rangle = \tau_{\pm} |x_{\pm}^* \rangle , \quad H^{\dagger} |x_{\pm}^* \rangle = \lambda_{\pm}^* |x_{\pm}^* \rangle . \quad (4.64)$$

To better show that the pseudo-Hermiticity is only satisfied for a real eigenvalue spectrum we calculate the derivative of the B -norm

$$\begin{aligned} d_t (\langle \psi | B | \psi \rangle) &= i \langle \psi | H^{\dagger} B - B H | \psi \rangle = i \langle \psi | (\mathbb{1} - C) H^{\dagger} B | \psi \rangle \\ &= 2 (\Im(\lambda_+) |c_+|^2 + \Im(\lambda_-) |c_-|^2) = 2 \Im(\lambda_+) (|c_+|^2 - |c_-|^2) \end{aligned} \quad (4.65)$$

and the result again implies that only for $\Im(\lambda_+) = -\Im(\lambda_-) = 0$ the B -norm is preserved. However, even for this general Hamiltonian, the dynamical evolution of the state vector on the Riemann sheet of $\Im(\lambda_+)$ can be represented by

$$d_t \log \left(\sqrt{\langle \psi | B | \psi \rangle} \right) = \Im(\lambda_+) \frac{|c_+|^2 - |c_-|^2}{|c_+|^2 + |c_-|^2} . \quad (4.66)$$

In this chapter we have shown that instead of using the c-product that does not preserve biorthogonality with a simultaneous \mathcal{PT} -symmetry, needs special considerations at the EP and is not applicable for asymmetric Hamiltonians, it is better to calculate the B matrix that is composed of the dual basis $B = \sum_i |x_i^* \rangle \langle x_i^*|$. This approach then allows to maintain the formalism of Hermitian quantum mechanics simply by introducing a new inner product $\langle \cdot | B | \cdot \rangle$. The c-product is then a special case of the B matrix inner product as the dual basis for symmetric Hamiltonians is obtained by complex conjugation $H = H^T \Rightarrow |x^* \rangle = |x \rangle^* = |\hat{x} \rangle$.

Finally, we have used the generalized Hermitian form to show that for asymmetric non-Hermitian Hamiltonians the norm of an arbitrary state vector is only preserved when the eigenvalue spectrum is real ($\Im(\lambda_+) = 0$).

5 Time evolution at the EP

In [section 3.3](#) we have analyzed some special solutions for the time evolution operator in the eigenbasis of the Hamiltonian. At the EP itself the Hamiltonian is not diagonalizable anymore and can only be transformed into a Jordan normal form with one 2×2 Jordan block with eigenvalue $\lambda = 0$. At this point the geometric multiplicity $\text{gmul}_J \lambda = 1$ and the algebraic multiplicity $\text{amul}_J \lambda = 2$. As the Jordan normal form has only one nonzero entry the time evolution of the state-vector expanded in the generalized eigenbasis is easy to integrate.

5.1 Stationary time evolution

To understand the general dynamics around an EP better we will analyze the stationary time evolution at the EP_+ ($g = +\gamma/2$) with constant damping $\gamma = \text{const.}$ The TDSE at the EP

$$\dot{\Psi}(t) = -iH_{\text{EP}_+} \Psi(t) = -i\frac{\gamma}{2} \begin{pmatrix} -i & 1 \\ 1 & i \end{pmatrix} \Psi(t), \quad \Psi(t) = \begin{pmatrix} \Psi_a(t) \\ \Psi_b(t) \end{pmatrix} \quad (5.1)$$

can be transformed into the generalized eigensystem ($|v\rangle, |h\rangle$) at the EP using X , X^{-1} and J from [Eq. 2.18](#). With $\tilde{\Psi}(t) = X^{-1}\Psi(t) = (\Psi_v(t), \Psi_h(t))^T$ the transformed TDSE becomes

$$\dot{\tilde{\Psi}}(t) = -iJ\tilde{\Psi}(t). \quad (5.2)$$

As the Jordan normal form of the traceless Hamiltonian has only one nonzero entry $J_{12} = \gamma$ the evolution at the EP follows

$$\frac{d}{dt} \begin{pmatrix} \Psi_v(t) \\ \Psi_h(t) \end{pmatrix} = \begin{pmatrix} -i\gamma\Psi_h(t) \\ 0 \end{pmatrix}. \quad (5.3)$$

The solution to this equation can be given in the mode basis $\Psi(0) = (\Psi_a, \Psi_b)^T$ or the generalized eigenbasis $\tilde{\Psi}(0) = (\Psi_v, \Psi_h)^T = X^{-1}\Psi(0)$ as

$$\Psi_h(t) = \Psi_h = -\frac{i}{\sqrt{2}}(\Psi_a + i\Psi_b) \quad (5.4)$$

$$\Psi_v(t) = \Psi_v - i\gamma\Psi_h t = \frac{1}{\sqrt{2}}(\Psi_a - i\Psi_b) - \frac{\gamma}{\sqrt{2}}(\Psi_a + i\Psi_b)t \quad (5.5)$$

which means that the population of $|h\rangle$ remains constant whereas $\Psi_v(t)$ changes linearly with time at the rate of the initial population of $|h\rangle$ times the damping γ . A state that is

initialized only in the eigenvector $\tilde{\Psi}(0) = (\Psi_v, \Psi_h)^T = (1, 0)^T$ therefore remains in this state. If $|h\rangle$ is initially populated then its population stays constant, but the ratio of the populations is linearly approaching zero $(\Psi_h(t)/\Psi_v(t))|_{t \rightarrow \infty} = 0$ as $\Psi_v(t)$ is outgrowing $\Psi_h(t)$. This long time behavior despite seeming trivial entails a far reaching conclusion. The fact that there is a generalized eigenbasis at the EP represented by $|v\rangle, |h\rangle$ ensures that the time-reversal symmetry is upheld for all times. Still, as the ratio Ψ_h/Ψ_v tends towards a constant value for $t \rightarrow \infty$ this must happen in every other (well defined) basis as well. In the mode basis the time dependent ratio of the population behaves like

$$\frac{a(t)}{b(t)} = \frac{a_0 - (a_0 + ib_0)\frac{\gamma}{2}t}{b_0 - i(a_0 + ib_0)\frac{\gamma}{2}t} \quad (5.6)$$

with a Taylor expansion

$$\left. \frac{a(t)}{b(t)} \right|_{t \rightarrow \infty} = -i + i\frac{2}{\gamma t} + \mathcal{O}\left(\frac{1}{t^2}\right) \quad (5.7)$$

that is to first order independent of a_0, b_0 and approaches linearly the fixed ratio $-i$ where the damping γ of course sets the pace for this process. For completeness we also write down explicitly the time evolution operator at the EP in the generalized eigenbasis

$$U_{\text{EP}}(t) = \begin{pmatrix} 1 & -i\gamma t \\ 0 & 1 \end{pmatrix}. \quad (5.8)$$

5.2 Dynamical time evolution at the EP

As our general 2×2 model consists of three real parameters the EP is actually a one parameter family of EPs that can be parametrized by γ . By making $\gamma = \gamma(t)$ time dependent the EP is not stationary in parameter space and we want to calculate the evolution of the population of the generalized eigenbasis ($|v(t)\rangle, |h(t)\rangle$) along a curve that connects EPs.

The general similarity transformation for the Hamiltonian in [Eq. 5.1](#) into its (time dependent) eigenbasis

$$\tilde{H}(t) = H_{\text{EP}}(t) + i\frac{dX^{-1}(t)}{dt}X(t) \quad (5.9)$$

shows that the choice of a static basis ($X \neq X(t)$) is preferable in this case leading to the Schrödinger equation

$$\frac{d}{dt} \begin{pmatrix} \Psi_v(t) \\ \Psi_h(t) \end{pmatrix} = -i \begin{pmatrix} 0 & \gamma(t) \\ 0 & 0 \end{pmatrix} \begin{pmatrix} \Psi_v(t) \\ \Psi_h(t) \end{pmatrix} \quad (5.10)$$

in the eigenbasis $|v(t)\rangle, |h(t)\rangle$. The resulting equation of course differs only in the time dependence of $\gamma(t)$. The population of $\Psi_h(t) = \Psi_h(0)$ is still static but the solution for

$\Psi_v(t)$ now depends on the path of $\gamma(t)$

$$\begin{aligned}\Psi_h(t) &= \Psi_h(0) \\ \Psi_v(t) &= \Psi_v(0) - i\Psi_h(0) \int_0^t \gamma(t') dt'\end{aligned}\tag{5.11}$$

so that the effective damping rate is given by the accumulated damping rates $\gamma_{\text{eff}} = \int_0^t \gamma(t') dt'$. The time evolution for the expansion coefficient of the eigenvector, $\Psi_v(t) = \Psi_v(0) - i\gamma_{\text{eff}}(t)\Psi_h(0)$, has then the same form as before.

6 Transfer efficiency and chirality

In the eigenbasis of the Hamiltonian the dynamical equations for the wave function and the time evolution operator only depend on the eigenvalues λ and on the non-adiabatic coupling f . The latter is proportional to $1/T$, which makes it necessary to distinguish two regimes of dynamical encircling: rapid loops and quasi-adiabatic loops.

When a periodic parameter path is completed rapidly the final state is always equivalent to the initial one. The further analysis therefore only covers the quasi-adiabatic regime. In the context of non-Hermitian physics, quasi-adiabaticity describes the regime where parameter changes are slow enough so that the dynamical solution can follow either one of the eigenvectors with the exceptional non-adiabatic transitions. A loose condition for quasi-adiabaticity is that the coupling between the modes should be much smaller than the difference between the eigenvalues $|f(t)/(2\lambda(t))| \ll 1$ [30]. This implies that the loop time T is sufficiently large so that the state vector can follow either one of the two Riemann sheets. In this case one finds that at the end of the loop ($t = T$) the system is mostly in one of the two eigenvectors. Depending on the initial conditions - that is initial parameter configuration $(g(0), \omega(0), \gamma(0))$ and initial state $(c_-(0), c_+(0))$ - it is possible to have up to two non-adiabatic transitions during one revolution. This is depicted in Fig. 6.1 where we show typical numerical solutions of the SE that are projected onto their eigenspectrum for a ccw circular loop around the EP. The initial conditions have been chosen in a way to get either zero (Fig. 6.1a), one (Fig. 6.1b) or two (Fig. 6.1c) non-adiabatic transitions. These images also reveal that for an initial eigenstate an even number of jumps (a) lead to the opposite final state whereas an odd number of jumps (b) brings the state back to itself after a closed loop.

6.0.1 Transfer efficiency

To effectively compare the solutions for different initial conditions we introduce the transfer efficiency t_E in the same way as in [33]. Given an initial configuration where the system is in either one of the eigenvectors ($|\psi(0)\rangle = |+(0)\rangle = \psi_+ \vee |\psi(0)\rangle = |-(0)\rangle = \psi_-$), the transfer efficiency is defined as the normalized eigenvector population of the mode that is initially unoccupied

$$t_E^\pm(t) := \frac{|c_\mp(t)|^2}{|c_-(t)|^2 + |c_+(t)|^2} \quad , \quad t_E \in [0, 1] \quad , \quad (6.1)$$

where the superscript represents the initial state. Although possible, we will not dynamically track the transfer efficiency during the evolution, instead we are interested in the transfer efficiency after one (or more) cycle(s). To avoid problems with a swap of the instantaneous eigenvectors that occurs during the propagation it is easier to

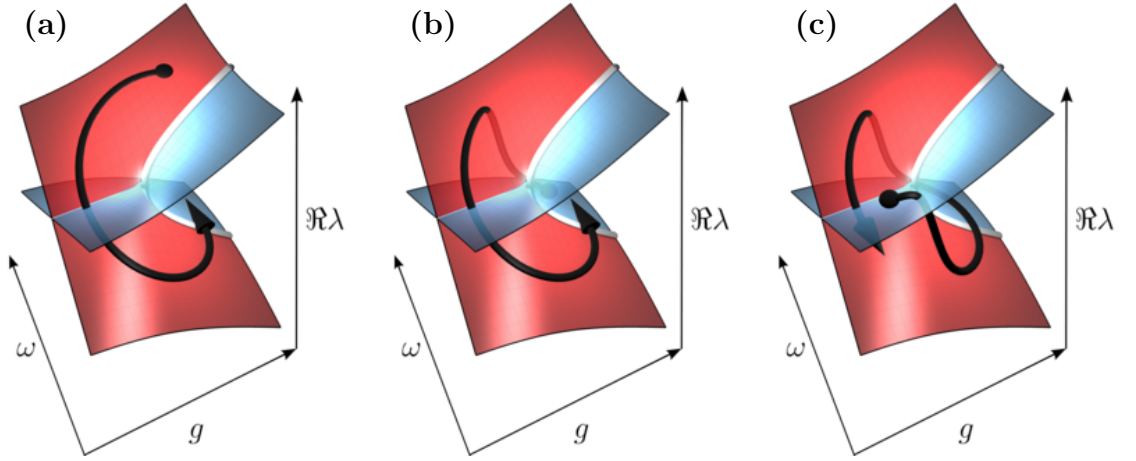


Figure 6.1: Time dependent eigenvector populations in the quasi-adiabatic regime projected onto the respective real eigenspectrum (red and blue surfaces correspond to the eigenvalues with gain and loss respectively), i.e. $\Re(\lambda(t))(|c_+(t)|^2 - |c_-(t)|^2)/(|c_+(t)|^2 + |c_-(t)|^2)$. The black line indicates the numerical solution of the Schrödinger equation in the eigenbasis of the Hamiltonian using an EP-centered circular path $\{g(t), \omega(t), \gamma(t)\} = \{\gamma/2 + r \cos(\phi(t)), r \sin(\phi(t)), \gamma\}$ with $\phi(t) = 2\pi t/T + \phi_0$, $\gamma = 1$. The starting positions along the loop ϕ_0 and the initial states have been chosen so that the solution has either zero (a), one (b) or even two (c) non-adiabatic transitions from the loss to the gain state.

calculate the transfer efficiency at the end of the loop using the initial eigenbasis. The resulting transfer efficiency is unaltered when we calculate the coefficients according to $c_{\mp}^0(T) = \langle \mp(0) | \psi(T) \rangle$. Another important feature of dynamical encircling an EP is the dependence on the rotational direction. To discern cw (\odot) from ccw (\ominus) revolutions an additional arc is introduced in the superscript so that the transfer efficiency for an initial ψ_+ state for a ccw loop is denoted as

$$t_E^{\odot}(T) = \frac{|c_-^0(T)|^2}{|c_-^0(T)|^2 + |c_+^0(T)|^2} . \quad (6.2)$$

6.0.2 Population inversion

The population inversion $p_I \in [-1, 1]$

$$p_I(t) := \frac{|c_+(t)|^2 - |c_-(t)|^2}{|c_+(t)|^2 + |c_-(t)|^2} \quad (6.3)$$

is a time dependent measure of the current normalized population distribution during the propagation. The two extreme cases are

$$\begin{aligned} p_I(t) = -1 &\Rightarrow |\psi(t)\rangle = |-(t)\rangle, \\ p_I(t) = +1 &\Rightarrow |\psi(t)\rangle = |+(t)\rangle. \end{aligned}$$

The population inversion vanishes only if the population of the eigenvectors is equal, e.g. as observed at the EP

$$p_I(t) = 0 \Leftrightarrow |c_-(t)|^2 = |c_+(t)|^2. \quad (6.4)$$

An additional superscript denotes again the initial state, such that $p_I^+(0) = +1$ and $p_I^-(0) = -1$.

6.0.3 Chirality

As the transfer efficiency $t_E \in [0, 1]$ is a number that specifies how much population has been transferred to the other mode, a value $t_E > 1/2$ at the end of a loop can be interpreted as a transition of the system to the other mode. Based on this, we define the chirality of a loop starting in either one ψ_{\pm} as the combined transfer efficiency for a cw and a ccw loop

$$c_Y^{\pm} := 4 \left(t_E^{\oplus} - \frac{1}{2} \right) \left(t_E^{\ominus} - \frac{1}{2} \right), \quad c_Y \in [-1, 1]. \quad (6.5)$$

A value $c_Y < 0$ characterizes a chiral loop, which means that the cw and ccw propagation lead to different final states. This phenomenon is mostly referred to as an asymmetric switch [29, 31, 32] and our definition of chirality is an elegant way to quantify this effect. In the quasi-adiabatic regime most of the loops are either completely chiral ($c_Y \approx -1$) or completely non-chiral ($c_Y \approx 1$).

Chirality from population inversion

There is another expression for the chirality in terms of the population inversion at the end of the loop that follows from Eq. 6.5

$$c_Y^{\pm} := p_I^{\oplus} p_I^{\ominus}, \quad c_Y \in [-1, 1]. \quad (6.6)$$

Both definitions Eqs. 6.5 and 6.6 give the same result whether the initial eigenbasis ($c_{\mp}^0(T) = \langle \mp(0) | \psi(T) \rangle$) or the final eigenbasis ($c_{\mp}(T) = \langle \mp(T) | \psi(T) \rangle$) is used to determine the expansion coefficients as long as the eigenvector flip is properly taken into account.

6.1 Relations with the time evolution operator

All the analytical solutions of the TDSE that are derived in the following are using the time evolution operator instead of a state vector. A convenient way to get the population

inversion for pure initial states ψ_{\pm} is by taking the diagonal elements of the matrix R defined as

$$R := -\frac{\tilde{U}^{\dagger} \boldsymbol{\sigma}_z \tilde{U}}{\tilde{U}^{\dagger} \tilde{U}} = \begin{pmatrix} p_1^- & \Phi^- \\ \Phi^+ & p_1^+ \end{pmatrix}, \quad (6.7)$$

where Φ^- and Φ^+ carry information about the phase relation between the two distinct initial states. Following the definition from [Eq. 6.6](#) the chirality can be obtained from R via

$$c_Y^- = R_{1,1}^{\mathbb{C}} R_{1,1}^{\mathbb{G}}, \quad c_Y^+ = R_{2,2}^{\mathbb{C}} R_{2,2}^{\mathbb{G}}, \quad (6.8)$$

that is solely calculated from $\tilde{U}^{\mathbb{C}}$ and $\tilde{U}^{\mathbb{G}}$.

7 Analytical solutions for special parameter paths

In this chapter we derive the analytical solutions for general straight parameter paths and EP-centered circular paths in the $\{g, \omega\}$ -plane with constant γ . Even though there are (approximate) analytical solutions available for circular paths for another choice of parameters [26, 30, 31], none of them include an angle ϕ_0 . The basis functions for the centered-circles in the $\{g, \omega\}$ -plane are Bessel functions, which are very well suited to derive results for asymptotic loop times T .

The analytical solutions for general straight paths are not present in the literature up to this point and they will serve to extract analytical predictions in the cavity-optomechanical (COM) setup in [33]. The basis functions for these paths are either parabolic cylinder functions also called Weber functions or confluent hypergeometric functions called Kummer functions.

The coupled first order Schrödinger equations in the mode basis $(a(t), b(t))^T$ can be solved by transforming it to a set of second order ordinary differential equations (ODEs). The obtained circular solutions are then used in the following chapters to dissect the chiral behavior (asymmetric mode switch) of closed contours in the vicinity of an EP. The general straight paths are useful to analyze the behavior of the eigenvectors upon dynamically passing through an EP and to show that deformed contours yield the same asymmetric switch.

7.1 Uncoupled second order differential equations

The TDSE that describes the time evolution of the modal populations $(a(t), b(t))^T$ using our traceless, symmetric model Hamiltonian is given by

$$\begin{pmatrix} \dot{a}(t) \\ \dot{b}(t) \end{pmatrix} = -i \begin{pmatrix} -\xi(t) & g(t) \\ g(t) & \xi(t) \end{pmatrix} \begin{pmatrix} a(t) \\ b(t) \end{pmatrix}, \quad (7.1)$$

where we generally allow $\xi, g \in \mathbb{C}$. This set of coupled first order ODEs can be transformed to a set of uncoupled second order ODEs for the two coefficients $a(t), b(t)$. Omitting all t

dependencies, the second order differential equations are

$$\ddot{a} - \frac{\dot{g}}{g} \dot{a} + \left[g^2 + \xi^2 + i \left(\frac{\dot{g}}{g} \xi - \dot{\xi} \right) \right] a = 0 \quad (7.2)$$

$$\ddot{b} - \frac{\dot{g}}{g} \dot{b} + \left[g^2 + \xi^2 - i \left(\frac{\dot{g}}{g} \xi - \dot{\xi} \right) \right] b = 0 . \quad (7.3)$$

The initial conditions are linked to the Schrödinger equation

$$a(0) = a_0 \quad \wedge \quad \dot{a}(0) = \bar{a}_0 = +i (\xi(0)a_0 - g(0)b_0) , \quad (7.4)$$

$$b(0) = b_0 \quad \wedge \quad \dot{b}(0) = \bar{b}_0 = -i (\xi(0)b_0 + g(0)a_0) . \quad (7.5)$$

The initial conditions in Eqs. 7.4 and 7.5 include four constants a_0, b_0, \bar{a}_0 and \bar{b}_0 but only two of them can be set independently. All choices are interchangeable and are related to each other via a matrix relation which we illustrate in an example by connecting the pair (a_0, b_0) with (a_0, \bar{a}_0)

$$\begin{pmatrix} a_0 \\ \bar{a}_0 \end{pmatrix} = \begin{pmatrix} 1 & 0 \\ i\xi(0) & -ig(0) \end{pmatrix} \begin{pmatrix} a_0 \\ b_0 \end{pmatrix} . \quad (7.6)$$

7.2 Analytical solutions for straight parameter paths

We seek the analytical solution to Eqs. 7.4 and 7.5 for a non-periodic, straight parameter path in the $\{g, \omega\}$ -plane. The path can be parametrized as

$$\begin{aligned} g(t) &= g_c + \cos(\alpha) \frac{r}{2} \left(1 - \frac{2t}{T} \right) , \\ \omega(t) &= \omega_c + \sin(\alpha) \frac{r}{2} \left(1 - \frac{2t}{T} \right) , \\ \gamma(t) &= \gamma . \end{aligned} \quad (7.7)$$

This path has length r and an angle¹² $\alpha \in [0, \pi)$ about the g -axis. This is exemplified in Fig. 7.1 for a path with $\{g_c, \omega_c\} = \{0.2, 0\}$, $r = 0.5$ and $\alpha = \pi/3$.

The initial values of a general straight path are defined already here because we will need them throughout the following derivation

$$\begin{aligned} g_0 &= g(0) = g_c + \frac{r}{2} \cos(\alpha) , & \omega_0 &= \omega(0) = \omega_c + \frac{r}{2} \sin(\alpha) , \\ \gamma &= \gamma(0) , & \xi_0 &= \xi(0) = \omega_0 + i \frac{\gamma}{2} , \\ \varepsilon_0 &= g_0 \cos(\alpha) + \xi_0 \sin(\alpha) , & \varphi_0 &= g_0 \sin(\alpha) - \xi_0 \cos(\alpha) . \end{aligned} \quad (7.8)$$

¹²The choice $\alpha \in [0, \pi)$ and $r \in \mathbb{R} \setminus 0$ defines every path uniquely.

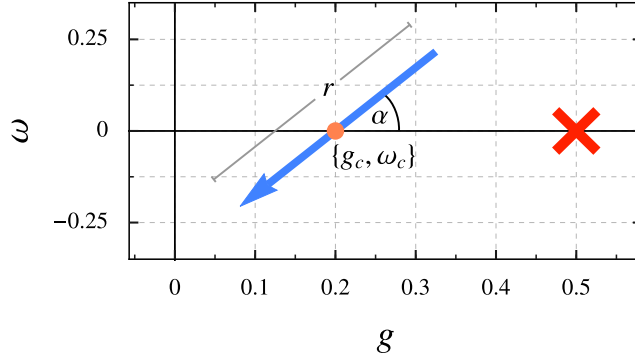


Figure 7.1: Sample straight parameter path in the $\{g, \omega\}$ -plane parametrized according to Eq. 7.7 with $\{g_c, \omega_c\} = \{0.2, 0\}$ (orange dot), $r = 0.5$ and $\alpha = \pi/3$. The beginning and end of the arrow correspond to $t = 0$ and $t = T$ respectively. The EP_+ is marked with a red cross.

The second order ODEs would take a much simpler form if there was no term (\dot{g}/g) . This is achieved by a similarity transformation that makes the off-diagonal elements in the Hamiltonian constant. The transformation we seek is of the form

$$P(\beta) = \left(\cos \frac{\beta}{2} \sigma_0 - i \sin \frac{\beta}{2} \sigma_y \right), \quad (7.9)$$

with a real angle β . After applying the similarity transformation $\tilde{H}(\beta) = P^{-1}(\beta) H P(\beta)$, we find that the off-diagonal is now

$$\tilde{H}_{1,2}(\beta) = -\frac{rt}{T} \cos(\alpha - \beta) + g_0 \cos(\beta) + \xi_0 \sin(\beta), \quad (7.10)$$

which is time-independent for $\beta = \alpha + (2n + 1)\pi/2$, $n \in \mathbb{Z}$. The values ε_0 and φ_0 that were defined in Eq. 7.8 are the diagonal and off-diagonal elements of the transformed Hamiltonian \tilde{H} at $t = 0$. For $n = -1$ the differential equations become

$$\ddot{\chi}_{\pm}(t) + \left[\left(\frac{r^2}{T^2} \right) t^2 - \left(\frac{2r\varepsilon_0}{T} \right) t + \left(\xi_0^2 + g_0^2 \pm \frac{ir}{T} \right) \right] \chi_{\pm}(t) = 0 \quad (7.11)$$

with

$$\begin{pmatrix} \chi_+(t) \\ \chi_-(t) \end{pmatrix} = P^{-1}(\alpha - \pi/2) \begin{pmatrix} a(t) \\ b(t) \end{pmatrix}. \quad (7.12)$$

The coefficient in Eq. 7.11 is a second order polynomial in t . In general, a second order ODE of the form

$$\ddot{w}(t) + (at^2 + bt + c) w(t) = 0, \quad (7.13)$$

with constant coefficients a, b, c belongs to the class of a so called *Weber differential equation*. Its solution can be expressed in terms of *parabolic cylinder functions* $D_\nu(z)$ (see (19.) of [47]). Every Weber differential equation can be brought to either one of the forms

$$\begin{aligned} \ddot{w}(z) - \left(\frac{z^2}{4} + d \right) w(z) &= 0 & (1) \\ \ddot{w}(z) + \left(\frac{z^2}{4} - d \right) w(z) &= 0 & (2) \end{aligned} \quad (7.14)$$

by completing the square. There are linearly independent even and odd solutions to the form (1) that are given by

$$\begin{aligned} w_{\text{even}}(d, z) &= e^{-\frac{z^2}{4}} {}_1F_1 \left(\frac{d}{2} + \frac{1}{4}; \frac{1}{2}; \frac{z^2}{2} \right), \\ w_{\text{odd}}(d, z) &= ze^{-\frac{z^2}{4}} {}_1F_1 \left(\frac{d}{2} + \frac{3}{4}; \frac{3}{2}; \frac{z^2}{2} \right), \end{aligned} \quad (7.15)$$

where ${}_1F_1(a; b; z)$ are *confluent hypergeometric functions*.

We continue to solve Eq. 7.11 by identifying

$$a = \frac{r^2}{T^2}, \quad b = -\frac{2r\varepsilon_0}{T}, \quad c_{\pm} = g_0^2 + \xi_0^2 \pm \frac{ir}{T}$$

and completing the square

$$\ddot{\chi}_{\pm}(t) + \left[\left(\frac{rt}{T} - \varepsilon_0 \right)^2 + \left(\varphi_0^2 \pm \frac{ir}{T} \right) \right] \chi_{\pm}(t) = 0. \quad (7.16)$$

After applying a variable transformation $\kappa = \sqrt{\frac{2iT}{r}} \left(\frac{rt}{T} - \varepsilon_0 \right)$, the ODEs are finally of the form

$$\ddot{\chi}_{\pm}(\kappa) + \left[\pm \frac{1}{2} - \nu - \frac{\kappa^2}{4} \right] \chi_{\pm}(\kappa) = 0, \quad (7.17)$$

with the solution

$$\begin{aligned} \chi_{+}(\kappa) &= c_1 D_{-\nu}(\kappa) + c_2 D_{-1+\nu}(i\kappa) \\ \kappa(t) &= \sqrt{\frac{2iT}{r}} \left(\frac{rt}{T} - \varepsilon_0 \right) = \eta \left(\frac{rt}{T} - \varepsilon_0 \right), \quad \nu = \frac{\eta^2 \varphi_0^2}{4}, \quad \eta = \sqrt{\frac{2iT}{r}}. \end{aligned} \quad (7.18)$$

The full solution for $(\chi_+(\kappa), \chi_-(\kappa))^T$ can be inferred from the SE for κ

$$\chi_-(\kappa) = -\frac{\kappa}{\eta\varphi_0}\chi_+(\kappa) - \frac{2}{\eta\varphi_0}\dot{\chi}_+(\kappa) \quad (7.19)$$

to give

$$\begin{pmatrix} \chi_+(\kappa) \\ \chi_-(\kappa) \end{pmatrix} = M(\kappa) \begin{pmatrix} c_1 \\ c_2 \end{pmatrix} = \begin{pmatrix} D_{-\nu}(\kappa) & D_{-1+\nu}(i\kappa) \\ \frac{2}{\eta\varphi_0}(D_{1-\nu}(\kappa) - \kappa D_{-\nu}(\kappa)) & \frac{2i}{\eta\varphi_0}D_{\nu}(i\kappa) \end{pmatrix} \begin{pmatrix} c_1 \\ c_2 \end{pmatrix}. \quad (7.20)$$

Some sumptuous calculations involving the Wronskian lead to the determinant and hence to the inverse of $M(\kappa)$ that is needed to substitute the coefficients $(c_1, c_2)^T$ by the initial conditions at time $t = 0 \Leftrightarrow \kappa(0) = \kappa_0 = -\eta\varepsilon_0$

$$\begin{pmatrix} c_1 \\ c_2 \end{pmatrix} = \frac{\eta\varphi_0}{2ie^{\frac{i\pi\nu}{2}}} \begin{pmatrix} \frac{2i}{\eta\varphi_0}D_{\nu}(i\kappa_0) & -D_{-1+\nu}(i\kappa_0) \\ -\frac{2}{\eta\varphi_0}(D_{1-\nu}(\kappa_0) - \kappa_0 D_{-\nu}(\kappa_0)) & D_{-\nu}(\kappa_0) \end{pmatrix} \begin{pmatrix} \chi_+(\kappa_0) \\ \chi_-(\kappa_0) \end{pmatrix}. \quad (7.21)$$

In order to relate this back to the original basis $(a(t), b(t))^T$ we undo the similarity transformation

$$\begin{pmatrix} a(t) \\ b(t) \end{pmatrix} = PM(\kappa(t))M(\kappa_0)^{-1}P^{-1} \begin{pmatrix} a_0 \\ b_0 \end{pmatrix} = U(t) \begin{pmatrix} a_0 \\ b_0 \end{pmatrix} \quad (7.22)$$

where

$$P = \begin{pmatrix} \cos\left(\frac{\pi}{4} - \frac{\alpha}{2}\right) & \sin\left(\frac{\pi}{4} - \frac{\alpha}{2}\right) \\ -\sin\left(\frac{\pi}{4} - \frac{\alpha}{2}\right) & \cos\left(\frac{\pi}{4} - \frac{\alpha}{2}\right) \end{pmatrix},$$

which satisfies the necessary initial condition $U(0) = \mathbb{1}$ by definition. This result can also be presented in the eigenbasis of the Hamiltonian by acting with $S(\theta(0))$, $S^{-1}(\theta(t))$ from [section 3.2](#) on [Eq. 7.22](#)

$$\begin{pmatrix} c_-(t) \\ c_+(t) \end{pmatrix} = S^{-1}(\theta(t)) U(t) S(\theta(0)) \begin{pmatrix} c_-(0) \\ c_+(0) \end{pmatrix} = \tilde{U}(t) \begin{pmatrix} c_-(0) \\ c_+(0) \end{pmatrix}. \quad (7.23)$$

The solutions shown in [Eqs. 7.20](#) and [7.21](#) are valid for every straight path in the $\{g, \omega\}$ -plane and can also be used to define a closed loop operator $K(T, 0)$ in any basis that evolves a state from $t = 0$ to $t = T$ along n connected paths. Every time evolution is then carried out by the respective time evolution operator in that basis ($U_i(t_1, t_0)$), e.g. [Eq. 7.22](#) or [Eq. 7.23](#), and the closed loop operator is then given as

$$K(T, 0) = \prod_{i=1}^n U_i(T_i, T_{i-1}), \quad (7.24)$$

with the overall loop time $T = \sum_{i=1}^n (T_i - T_{i-1}) = T_n - T_0$.

The parabolic cylinder function $D_\nu(z)$ is entire in $\nu \in \mathbb{C}$ and $z \in \mathbb{C}$ and has no branch cut discontinuities making this solution extremely versatile.

7.3 Analytical solutions for EP-centered circular paths

As we have seen before a suitable similarity transformation can lead to a second order ODE that is analytically solvable. There is another similarity transformation that allows a general analytical solution for EP-centered circles in the $\{g, \omega\}$ -plane which uses the basis

$$P = \frac{1}{\sqrt{2}} \begin{pmatrix} 1 & 1 \\ i & -i \end{pmatrix}, \quad P^{-1} = \frac{1}{\sqrt{2}} \begin{pmatrix} 1 & -i \\ 1 & i \end{pmatrix} \quad (7.25)$$

to transform the Hamiltonian to a form with solely off-diagonal elements¹³

$$\tilde{H}(t) = P^{-1}H(t)P = \begin{pmatrix} 0 & -ig(t) - \xi(t) \\ ig(t) - \xi(t) & 0 \end{pmatrix} = \begin{pmatrix} 0 & h_{12}(t) \\ h_{21}(t) & 0 \end{pmatrix}. \quad (7.26)$$

The second order ODEs that follows from this in the new basis $(\alpha(t), \beta(t))^T$

$$\begin{pmatrix} \alpha(t) \\ \beta(t) \end{pmatrix} = P^{-1} \begin{pmatrix} a(t) \\ b(t) \end{pmatrix} = \frac{1}{\sqrt{2}} \begin{pmatrix} a(t) - ib(t) \\ a(t) + ib(t) \end{pmatrix} \quad (7.27)$$

are given as

$$\ddot{\alpha}(t) - \frac{\dot{h}_{12}(t)}{h_{12}(t)}\dot{\alpha}(t) + h_{12}(t)h_{21}(t)\alpha(t) = 0, \quad (7.28)$$

$$\ddot{\beta}(t) - \frac{\dot{h}_{21}(t)}{h_{21}(t)}\dot{\beta}(t) + h_{12}(t)h_{21}(t)\beta(t) = 0. \quad (7.29)$$

The path parametrization for EP-centered circular paths

$$\begin{aligned} g(t) &= \frac{\gamma}{2} + r \cos\left(\frac{2\pi t}{T} + \phi_0\right), \\ \omega(t) &= r \sin\left(\frac{2\pi t}{T} + \phi_0\right), \\ \gamma(t) &= \gamma, \end{aligned} \quad (7.30)$$

¹³As $\xi \in \mathbb{C}$ the elements $h_{12}(t)$ and $h_{21}(t)$ are not proportional to one another.

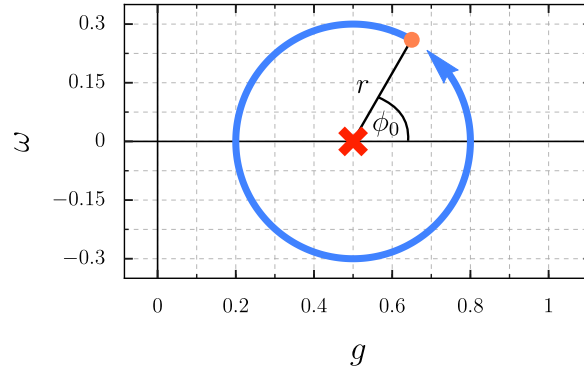


Figure 7.2: Sample ccw EP-centered circular parameter path in the $\{g, \omega\}$ -plane parametrized according to Eq. 7.30 with $\phi_0 = \pi/3$ and $r = 0.3$. The initial parameter configuration at $t = 0$ ($\{g_0, \omega_0\}$) is represented by the orange dot and the EP_+ is marked with a red cross.

is depicted in Fig. 7.2 for a sample loop with $\phi_0 = \pi/3$ and $r = 0.3$.

After we insert the path parametrization, the coefficients in Eqs. 7.28 and 7.29 become

$$\frac{\dot{h}_{12}(t)}{h_{12}(t)} = -\frac{2\pi i}{T} \frac{1}{1 + \frac{\gamma}{r} e^{i(\frac{2\pi t}{T} + \phi_0)}} , \quad \frac{\dot{h}_{21}(t)}{h_{21}(t)} = \frac{2\pi i}{T} , \quad (7.31)$$

$$h_{12}(t)h_{21}(t) = r^2 \left(1 + \frac{\gamma}{r} e^{i(\frac{2\pi t}{T} + \phi_0)} \right) .$$

For EP_+ -centered circles the coefficient \dot{h}_{21}/h_{21} takes a very simple form, which reduces the equation for $\beta(t)$ (Eq. 7.29) to

$$\ddot{\beta}(t) - \frac{2\pi i}{T} \dot{\beta}(t) + r^2 \left(1 + \frac{\gamma}{r} e^{i(\frac{2\pi t}{T} + \phi_0)} \right) \beta(t) = 0 . \quad (7.32)$$

Now using the variable substitution $t \rightarrow \eta(t)$

$$\eta = \frac{\gamma}{r} e^{i(\frac{2\pi t}{T} + \phi_0)}$$

$$\frac{d}{dt} = \left(\frac{2\pi i}{T} \right) \eta \frac{d}{d\eta} , \quad \frac{d^2}{dt^2} = \left(\frac{2\pi i}{T} \right)^2 \left(\eta^2 \frac{d^2}{d\eta^2} + \eta \frac{d}{d\eta} \right) \quad (7.33)$$

transforms the equation to

$$\eta^2 \frac{d^2 \beta(\eta)}{d\eta^2} - \left(\frac{rT}{2\pi} \right)^2 (1 + \eta) \beta(\eta) = 0 . \quad (7.34)$$

This is a form of the *Bessel differential equation* and its solution is given by [Eq. 10.13.2](#) in [\[48\]](#) as

$$\beta(\eta) = \sqrt{\eta} (c_1 I_{-\nu}(2a\sqrt{\eta}) + c_2 I_{\nu}(2a\sqrt{\eta})) \quad (7.35)$$

$$\eta = \frac{\gamma}{r} e^{i(\frac{2\pi t}{T} + \phi_0)}, \quad \nu = \sqrt{1 + 4a^2}, \quad a = \frac{rT}{2\pi} \quad (7.36)$$

where $I_{\nu}(z)$ represents the *modified Bessel functions* of the first kind of order $\nu \in \mathbb{R}$ with argument $z \in \mathbb{C}$.

From this result the solution for $\alpha(\eta)$ is inferred by converting $t \rightarrow \eta(t)$ in the SE for $\alpha(t)$ and taking the recurrence relation $I_{\nu-1}(z) - I_{\nu+1}(z) = \frac{2\nu}{z} I_{\nu}(z)$ to simplify the result to

$$\begin{aligned} \alpha(\eta) = \frac{2\pi i \gamma}{Tr^2} \frac{d\beta(\eta)}{d\eta} = \\ \frac{i\gamma}{r} \left[c_1 \left(I_{-\nu-1}(2a\sqrt{\eta}) + \frac{\nu+1}{2a\sqrt{\eta}} I_{-\nu}(2a\sqrt{\eta}) \right) + \right. \\ \left. c_2 \left(I_{\nu-1}(2a\sqrt{\eta}) - \frac{\nu-1}{2a\sqrt{\eta}} I_{\nu}(2a\sqrt{\eta}) \right) \right] . \quad (7.37) \end{aligned}$$

Finally, we can write down the time evolution operator $U(\eta)$ in the basis $(\alpha(t), \beta(t))^T$ as

$$U(\eta) = M(\eta) M^{-1}(\eta_0) \quad (7.38)$$

with

$$\begin{aligned} M(\eta) = \frac{i\gamma}{r} \begin{pmatrix} I_{-(\nu+1)}(2a\sqrt{\eta}) + \frac{\nu+1}{2a\sqrt{\eta}} I_{-\nu}(2a\sqrt{\eta}) & I_{\nu-1}(2a\sqrt{\eta}) - \frac{\nu-1}{2a\sqrt{\eta}} I_{\nu}(2a\sqrt{\eta}) \\ \frac{r\sqrt{\eta}}{i\gamma} I_{-\nu}(2a\sqrt{\eta}) & \frac{r\sqrt{\eta}}{i\gamma} I_{\nu}(2a\sqrt{\eta}) \end{pmatrix} \\ \eta(t) = \frac{\gamma}{r} e^{i(\frac{2\pi t}{T} + \phi_0)}, \quad \eta_0 = \frac{\gamma}{r} e^{i\phi_0}, \quad \nu = \sqrt{1 + 4a^2}, \quad a = \frac{rT}{2\pi} . \quad (7.39) \end{aligned}$$

The only thing left to do is to connect the coefficients $(c_1, c_2)^T$ with the initial condition $(\alpha_0, \beta_0)^T$ at $\eta(0) = \eta_0$

$$\begin{pmatrix} \alpha_0 \\ \beta_0 \end{pmatrix} = M(\eta_0) \begin{pmatrix} c_1 \\ c_2 \end{pmatrix} . \quad (7.40)$$

The inverse of $M(\eta_0)$ simplifies considerably as

$$\det(M(\eta_0)) = -\frac{i\gamma_0 \sin(\pi\nu)}{\pi ar}, \quad \text{adj}(M^{2 \times 2}) = \begin{pmatrix} M_{22} & -M_{12} \\ -M_{21} & M_{11} \end{pmatrix} . \quad (7.41)$$

which leads to

$$\begin{pmatrix} c_1 \\ c_2 \end{pmatrix} = M^{-1}(\eta_0) \begin{pmatrix} \alpha_0 \\ \beta_0 \end{pmatrix} = \frac{i\pi ar}{\gamma_0 \sin(\pi\nu)} \begin{pmatrix} M_{22} & -M_{12} \\ -M_{21} & M_{11} \end{pmatrix} \begin{pmatrix} \alpha_0 \\ \beta_0 \end{pmatrix}. \quad (7.42)$$

As $a > 0 \Rightarrow \nu > 1$ the order of the appearing Bessel functions is always a nonzero real number. From this the time evolution operator in the eigenbasis (EB) of $H(t)$ can be obtained by

$$U_{\text{EB}}(t) = S^{-1}(\theta(t)) P U(t) P^{-1} S(\theta(0)) \quad (7.43)$$

with P from Eq. 7.25 and S consisting of the eigenvectors $(|-\rangle, |+\rangle)$.

7.3.1 Analytic continuation

As the Bessel functions $I_\nu(z)$ have a branch cut discontinuity in the complex plane along the negative real axis at $z \in (-\infty, 0]$ we have to use analytic continuation whenever we cross that line, e.g. when we want to define a one-cycle evolution operator $U(\eta(T))$ (that always passes the branch cut once). The analytic continuation formula for the $I_\nu(z)$ reads (Eq. 10.34.1 in [48])

$$I_\nu(z e^{im\pi}) = e^{im\pi\nu} I_\nu(z), \quad (7.44)$$

where we have to use $m = 1$ for one cycle.

In front of the Bessel functions there is a factor $\sqrt{\eta}$. The principal value of the square root function has also a branch cut along the negative real axis $z \in (-\infty, 0]$ so for one cycle we define

$$\sqrt{z e^{2i\pi}} = e^{i\pi} \sqrt{z} \quad (7.45)$$

to make the square root continuous.

7.3.2 Uniform asymptotic expansion

The asymptotic expansion of $I_\nu(z), K_\nu(z)$ for large order $\nu \rightarrow \infty$ with $z (\neq 0)$ fixed and for a uniform expansion of Bessel functions of the form $I_\nu(\nu z), K_\nu(\nu z)$ with $0 < z < \infty$ is only valid if $\nu \rightarrow \infty$ through the positive real values. This requires the use of the connection formula

$$I_{-\nu}(z) = I_\nu(z) + \frac{2}{\pi} \sin(\pi\nu) K_\nu(z) \quad (7.46)$$

to transform the negative orders to positive ones.

The uniform asymptotic expansion for the Bessel functions $I_\nu(z)$ and $K_\nu(z)$ is then

given by Eq. 10.41(ii) in [48] using $\eta = \sqrt{1+z^2} + \ln\left(\frac{z}{1+\sqrt{1+z^2}}\right)$

$$\begin{aligned} I_\nu(\nu z) &\sim \frac{1}{\sqrt{2\pi\nu}} \frac{e^{\nu\eta}}{(1+z^2)^{1/4}} , \\ K_\nu(\nu z) &\sim \sqrt{\frac{\pi}{2\nu}} \frac{e^{-\nu\eta}}{(1+z^2)^{1/4}} , \\ I'_\nu(\nu z) &\sim \frac{1}{\sqrt{2\pi\nu}} \frac{e^{\nu\eta}(1+z^2)^{1/4}}{z} , \\ K'_\nu(\nu z) &\sim -\sqrt{\frac{\pi}{2\nu}} \frac{e^{-\nu\eta}(1+z^2)^{1/4}}{z} . \end{aligned} \tag{7.47}$$

7.3.3 Floquet basis and the one-cycle evolution operator

In [26] it has been shown that the one-cycle evolution operator can be expressed in terms of Floquet states, that is the states that return to themselves after one loop up to a complex factor. Analytic continuation of the modified Bessel function immediately shows that the eigenvalues of the one-cycle evolution operator are unimodular $\lambda_{1,2} = -\exp(\pm i\pi\nu)$ and that the corresponding Floquet states at $t = 0$ are

$$\begin{aligned} |F_\pm(0)\rangle &= \begin{pmatrix} \frac{c}{2\kappa} \partial_\kappa (\kappa I_{\pm\nu}(2a\kappa)) \\ \kappa I_{\pm\nu}(2a\kappa) \end{pmatrix} , \\ \langle F_\pm(0)| &= (-\kappa I_{\mp\nu}(2a\kappa) , \quad \frac{c}{2\kappa} \partial_\kappa (\kappa I_{\mp\nu}(2a\kappa))) , \\ \kappa &= \sqrt{\eta_0} = \sqrt{\frac{\gamma}{r}} e^{i\frac{\phi_0}{2}} , \quad c = \frac{i\gamma}{ar} . \end{aligned} \tag{7.48}$$

The respective biorthogonal normalization for those states evaluates to

$$\begin{aligned} \langle F_\pm | F_\mp \rangle &= 0 , \\ \langle F_\pm | F_\pm \rangle &= \mp \frac{c}{\pi} \sin(\pi\nu) . \end{aligned} \tag{7.49}$$

A formal closed expression for the one-cycle evolution operator in terms of the Floquet states is hence

$$U(T) = -e^{i\pi\nu} \frac{|F_+\rangle\langle F_+|}{\langle F_+ | F_+ \rangle} - e^{-i\pi\nu} \frac{|F_-\rangle\langle F_-|}{\langle F_- | F_- \rangle} . \tag{7.50}$$

The two eigenvalues are unimodular ($|\lambda_i| = 1$) and come in complex conjugate pairs ($\lambda_- \lambda_+ = 1$). The fact that the eigenvalues are unimodular can be seen from Liouville's formula [49], which states that for traceless, periodic Hamiltonians with period T

$$\det [U(0)] = \det [U(T)] , \tag{7.51}$$

which entails $\det[U(T)] = \lambda_- \lambda_+ = 1$ in our case. If $\nu \in \mathbb{C}$ (which is not possible for EP-centered circles) then the eigenvalues are not unimodular anymore but still reciprocal. We can use Eqs. 7.48 and 7.50 and define $G_{\pm} = \kappa I_{\pm\nu}(2a\kappa)$ to give a very compact expression for the one-cycle evolution operator

$$U(T) = \begin{pmatrix} -\frac{i\pi}{2\kappa}(G_+ \dot{G}_-) - \cos(\pi\nu) & \frac{i\pi c}{2\kappa^2} \dot{G}_+ \dot{G}_- \\ -\frac{2\pi i}{c} G_+ G_- & \frac{i\pi}{2\kappa}(G_+ \dot{G}_-) - \cos(\pi\nu) \end{pmatrix} \quad (7.52)$$

that is also valid for integer values of ν . The dot in Eq. 7.52 represents the derivative with respect to κ ($(*) = \partial_{\kappa}(*)$).

The representation of $U(T)$ in Eq. 7.50 discloses that the time evolution operator is degenerate at integer values of ν . We will show that this degeneracy leads to leveled eigenvector populations after $m \gg 1$ rounds.

Since the Floquet states are biorthogonal (for integer values ν the Floquet states are even self-orthogonal) the m -cycle evolution operator $U(mT) = (U(T))^m$ with $m \in \mathbb{N}$ has the same structure as the one-cycle operator $U(T)$ but the eigenvalues of $U(mT)$ are $\lambda_{\pm} = (-1)^m \exp(\pm i\pi m\nu)$. If ν is not an integer, but an integer fraction of the form $\nu = n/m$ with $n, m \in \mathbb{N}$ and $n > m$ then the m -cycle evolution operator has the following properties

$$\nu = \frac{n}{m} \Rightarrow \begin{cases} U(mT) = \mathbb{1}(-1)^{m+1} \\ U(2mT) = \mathbb{1} & n \text{ odd} \\ U(mT) = \mathbb{1}(-1)^m \\ U(2mT) = \mathbb{1} & n \text{ even} \end{cases} \quad (7.53)$$

that are independent of the starting position ϕ_0 . The simplest instance of this fact is visible for half-integer values of $\nu = n + 1/2$, $n \in \mathbb{N}$ that we are going to explore in the following chapters in detail. Those half-integer solutions fall into the n odd category of Eq. 7.53 with even m values so if $\nu = n + 1/2$ then $U(2T) = -\mathbb{1}$ and $U(4T) = +\mathbb{1}$.

7.3.4 Reversing the loop direction

A reversal of the propagation direction is generally performed by $\tilde{H}(t) \rightarrow \tilde{H}(-t)$. In the case of EP-centered circular loops the inverse direction (cw) is directly related to the ccw propagation direction. This relation is inferred from the Schrödinger equation for circular parametrization.

At first we rewrite the forward propagation with reference to the path parametrization from Eq. 7.30

$$\dot{\alpha}(t) = -(r\bar{z}e^{-i\phi(t)} + \gamma)\beta(t) \quad (7.54)$$

$$\dot{\beta}(t) = (rze^{i\phi(t)})\alpha(t) \quad (7.55)$$

using $\phi(t) = 2\pi t/T$ and $z = e^{i\phi_0}$, where the bar (\bar{z}) denotes complex conjugation. The differential equations for the amplitudes in the reverse direction $(\alpha_{\text{rev}}, \beta_{\text{rev}})^T$ are then obtained by $\phi(t) \rightarrow \phi(-t) = -\phi(t)$. To relate the reverse equations with the forward ones we additionally complex conjugate the reverse equations

$$\dot{\bar{\alpha}}_{\text{rev}}(t) = -(r z e^{-i\phi(t)} + \gamma) \bar{\beta}_{\text{rev}}(t) \quad (7.56)$$

$$\dot{\bar{\beta}}_{\text{rev}}(t) = (r \bar{z} e^{+i\phi(t)}) \bar{\alpha}_{\text{rev}}(t) \quad (7.57)$$

and finally single out factors of z and \bar{z} respectively

$$\dot{\bar{\alpha}}_{\text{rev}}(t) = -(r \bar{z} e^{-i\phi(t)} + \gamma \bar{z}^2) z^2 \bar{\beta}_{\text{rev}}(t) \quad (7.58)$$

$$\dot{\bar{\beta}}_{\text{rev}}(t) = (r z e^{+i\phi(t)}) \bar{z}^2 \bar{\alpha}_{\text{rev}}(t) . \quad (7.59)$$

Equation 7.58 reveals that the populations in the reverse direction cannot simply be obtained by a complex conjugation and an additional phase factor z^2 . For the case of $z \neq 1 \Leftrightarrow \phi_0 \neq (0 \wedge \pi)$ the reverse propagation rather corresponds to a forward propagation with a modified damping $\gamma = \gamma \bar{z}^2 \in \mathbb{C}$. The correspondence between forward and backward propagation can be written as

$$\begin{pmatrix} \alpha_{\text{rev}}(t) \\ \beta_{\text{rev}}(t) \end{pmatrix} = \begin{pmatrix} \bar{\alpha}(t) \\ e^{+2i\phi_0} \bar{\beta}(t) \end{pmatrix} \Big|_{\gamma=\gamma e^{-2i\phi_0}} \quad (7.60)$$

with correspondingly adapted initial conditions $(\alpha_{\text{rev}}(0), \beta_{\text{rev}}(0))^T = (\bar{\alpha}(0), e^{+2i\phi_0} \bar{\beta}(0))^T$ that stress the non-trivial aspect of the reverse loop for arbitrary ϕ_0 even further. In the special case of $\phi_0 = 0, \pi \Rightarrow (\alpha_{\text{rev}}(t), \beta_{\text{rev}}(t))^T = (\bar{\alpha}(t), \bar{\beta}(t))^T$, the reverse loop can simply be obtained by complex conjugation.

Reverse loop for the time evolution operator

The time evolution operator always fulfills the same differential equation as the state vector in a given basis (Eq. 7.25). Therefore the result in Eq. 7.60 can be readily applied to reverse the loop direction also for $U(t)$

$$U_{\text{rev}}(t) = \begin{pmatrix} 1 & 0 \\ 0 & e^{+2i\phi_0} \end{pmatrix} \bar{U}(t, \gamma = \gamma e^{-2i\phi_0}) \begin{pmatrix} 1 & 0 \\ 0 & e^{-2i\phi_0} \end{pmatrix} \quad (7.61)$$

where the first and the third matrix on the right hand side cancel each other out at $t = 0$ so that $U_{\text{rev}}(0) = \mathbb{1}$ fulfills the initial condition for a time evolution operator. For $\phi_0 = 0, \pi$ the reverse time evolution operator is then again given by the complex conjugate of the forward one $U_{\text{rev}}(t) = \bar{U}(t)$.

8 Results for EP-centered circles

In the previous chapters we have set up the main tools to analyze dynamical parameter variations in the vicinity of an EP. In this chapter we start with the analytical equations for EP-centered circles with arbitrary starting angle ϕ_0 . We are especially interested in identifying the regions in parameter space where chirality occurs given that a single EP is encircled or not. We show that neither is chirality (asymmetric mode switching) a compulsory property of EP-enclosing loops nor is it limited to loops that only include exactly one EP.

8.1 Single round

In Eqs. 7.38 and 7.39 we have established the analytical solution for EP-centered circles and by showing the relation between the cw and ccw time evolution operator (section 7.3.4) we are able to efficiently calculate the transfer efficiency and chirality for every starting position $\{g_0, \omega_0\} = \{\gamma/2 + r \cos(\phi_0), r \sin(\phi_0)\}$ using arbitrary loop time T , damping rate γ , radius r and initial angle ϕ_0 . By fixing T and γ we can evaluate t_E and c_Y after one circular loop for every starting point $\{g_0, \omega_0\}$ and draw two individual maps for each initial state ψ_+ and ψ_- , called a *transfer efficiency/chirality map*.

For the specific values $T = 20$ and $\gamma = 1$ these maps are shown in Fig. 8.1 for $r < \gamma/2$ (enclosing only the EP₊). The left column displays an initial ψ_- and the right column an initial ψ_+ state. In Figs. 8.1a and 8.1b the transfer efficiency map is shown for a ccw and cw loop respectively. The third row (Fig. 8.1c) represents the chirality map that is calculated from (a) and (b). As expected, most of the loops are chiral ($c_Y \approx -1$) and the only non-chiral region is located around $\phi_0 = \pi$. We will see that the spread of this non-chiral region decreases if we increase the loop time T . The distinct non-chiral features (spikes) that are evident for an initial ψ_+ state (right column) are located at the half-integer values of the order ν (dashed, white circles) of the underlying Bessel functions. The relation between ν and the radius r of the loop is given by

$$r = \frac{\pi}{T} \sqrt{\nu^2 - 1}, \quad (8.1)$$

so that the exact position and number of the non-chiral features depend also on the loop time T .

When we increase the loop time to $T = 50$ in Fig. 8.2, the half-integer and integer values of ν are packed more densely leading to more non-chiral spikes around $\phi_0 = \pi$.

Also, the angle ϕ_0^* that separates chiral from non-chiral regions gets closer to π decreasing the non-chiral sector around $\phi_0 = \pi$. We see that chirality does not simply depend on quasi-adiabaticity $|f(t)/(2\lambda(t))| \ll 1$, which is already fulfilled for $T = 20$. Instead, chirality is a subtle effect that is to a great extent related to the starting position ϕ_0 of a loop.

To elaborate on these features of the asymmetric switching behavior (chirality), we particularly analyze the initial positions $\phi_0 = 0$ (real crossing) and $\phi_0 = \pi$ (imaginary crossing), where the latter is also the only \mathcal{PT} -symmetric parameter region in the $\{g, \omega\}$ -plane. We also allow $r > \gamma$, so that both EPs (EP_+ , EP_-) can be enclosed in the loop. The results for $\phi_0 = 0$ are shown in Fig. 8.3 for an initial ψ_- (blue, dashed line) and an initial ψ_+ (red, solid line) state. When the loop is too small $r \ll 1$, the absolute value of $f(t)$ is comparable to the absolute value of $\lambda(t)$ and so the loop is not in the quasi-adiabatic regime ($T = 20$ is fixed) and as a result non-chiral. As we increase the radius of the loop, chirality sets in as expected. At $r = \gamma = 1$ the loop starts to enclose also the EP_- and still, even if both EPs are encircled, the loop continues to be chiral. This is the complementary effect to an asymmetric switch for a loop that encloses no EP that was recently reported in [50]. The effect was however falsely described to depend on the loop time T at an arbitrary distance to the EP due to numerical errors and analytical inaccuracies. Redoing the numerical and analytical calculations ourselves, we were able to provide the authors with our insights, i.e. the necessary conditions for chirality, partially included in this work, leading to the recent publication of an extended erratum [51]. At a certain radius $r^* \approx 2.277$, this chiral behavior breaks down ($c_Y(r^*) = 0$). The analytical derivation for r^* are given in section 8.4. We see that an asymmetric mode switching behavior is not solely obtainable by encircling a single EP but also when both EPs or no EP at all are enclosed given that a certain distance to the EPs is not exceeded. We will analyze this dependence on the distance below.

In the case of $\phi_0 = \pi$ (Fig. 8.4) we observe that every loop that encloses a single EP is non-chiral. The initial gain state ψ_+ is thereby fully non-chiral ($c_Y \approx 1$) at the half-integer values of ν (dashed, vertical lines), i.e. at the position of the sharp peaks. Since the initial configuration ψ_- is also fully non-chiral, both initial states transfer their population to the other state. However, as the evolution of the initial loss state ψ_- at those peaks includes two non-adiabatic jumps this does not contradict the statement that only one of the two states can behave adiabatically (here the initial ψ_+ state does).

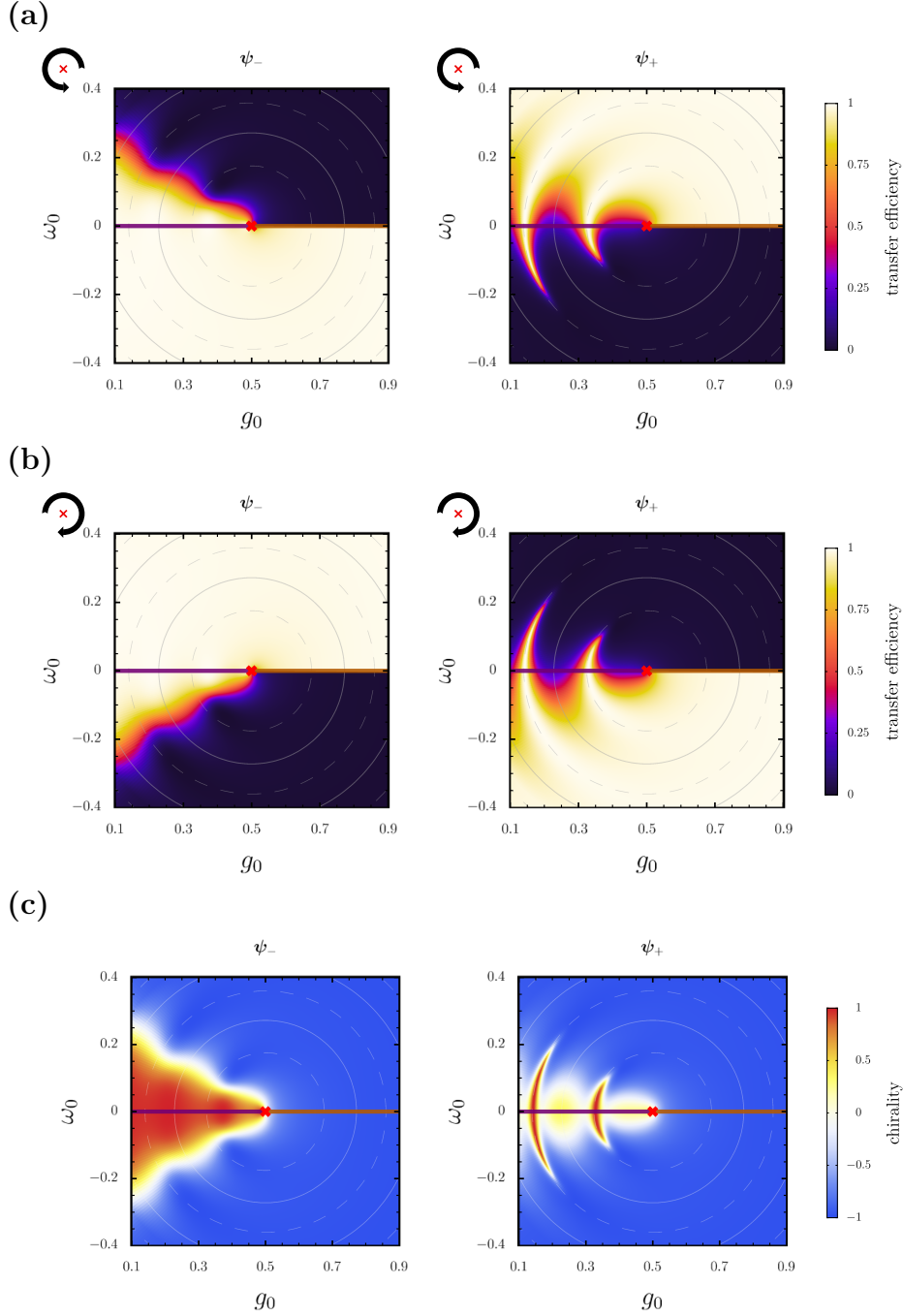
$$T = 20$$


Figure 8.1: Transfer efficiency (ccw in (a), cw in (b)) and chirality (c) for circular loops with starting points at $\{g_0, \omega_0\}$ that are centered around the EP (red cross) which is located at $\{g_{\text{EP}}, \omega_{\text{EP}}\} = \{0.5, 0\}$, hence $\gamma = 1$. The left column displays initial ψ_- states and the right column ψ_+ states at the respective initial position. A loop time $T = 20$ is for most starting points already in the quasi-adiabatic regime yielding a chiral loop. The prominent features in the right panel (initial gain state) are located at radii where the order ν is a half-integer (dashed, white circles) or integer (solid white circles).

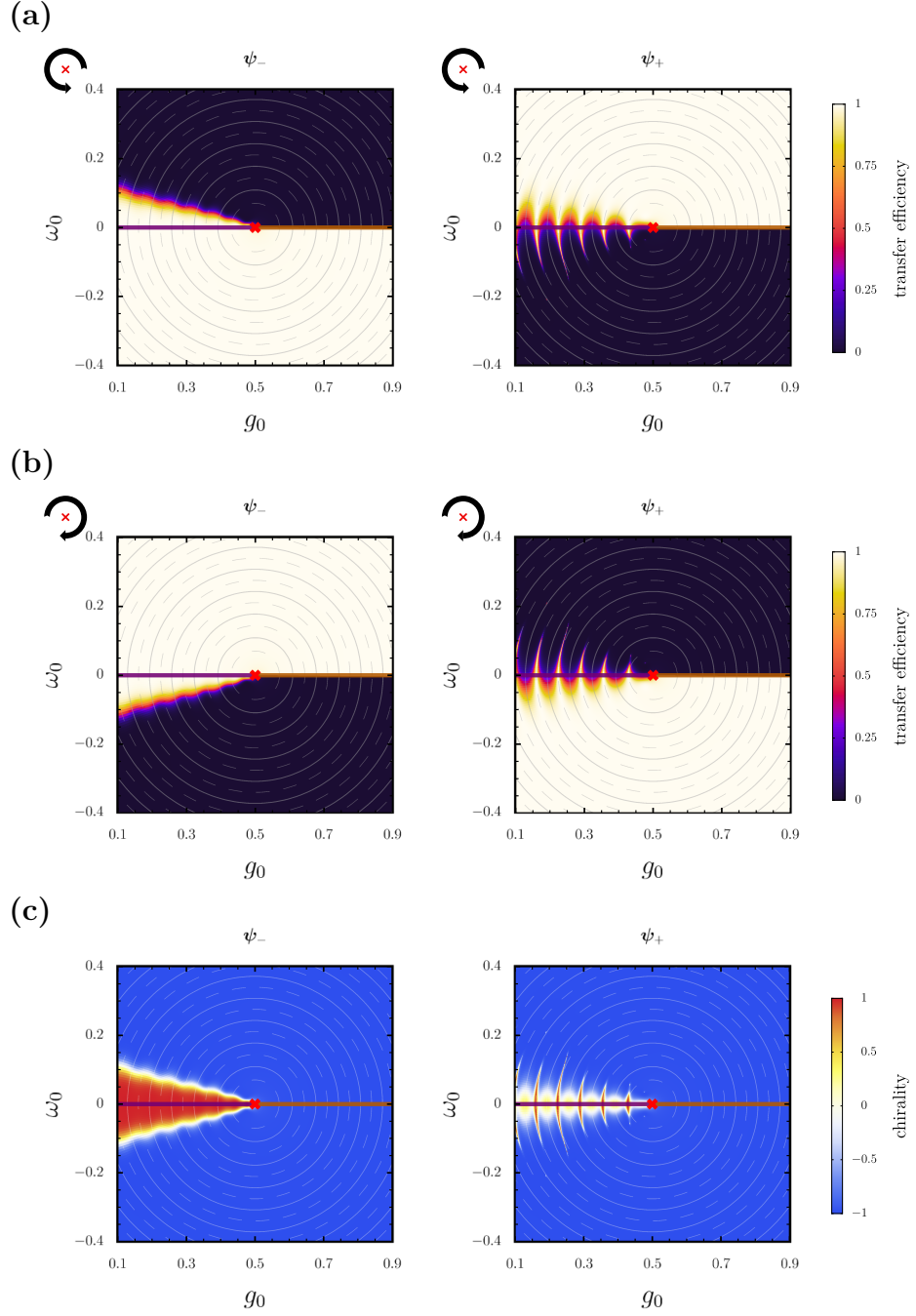
$$T = 50$$


Figure 8.2: Transfer efficiency (ccw in (a), cw in (b)) and chirality (c) for circular loops with starting points at $\{g_0, \omega_0\}$ that are centered around the EP (red cross) which is located at $\{g_{\text{EP}}, \omega_{\text{EP}}\} = \{0.5, 0\}$, hence $\gamma = 1$. The left column displays initial ψ_- states and the right column ψ_+ states at the respective initial position. For a rather large loop time $T = 50$ the non-chiral region around $\phi_0 = \pi$ is smaller. The prominent features in the right panel (initial gain state) are packed denser and they are narrower. They are located at radii where the order ν is a half-integer (dashed, white circles) or integer (solid white circles).

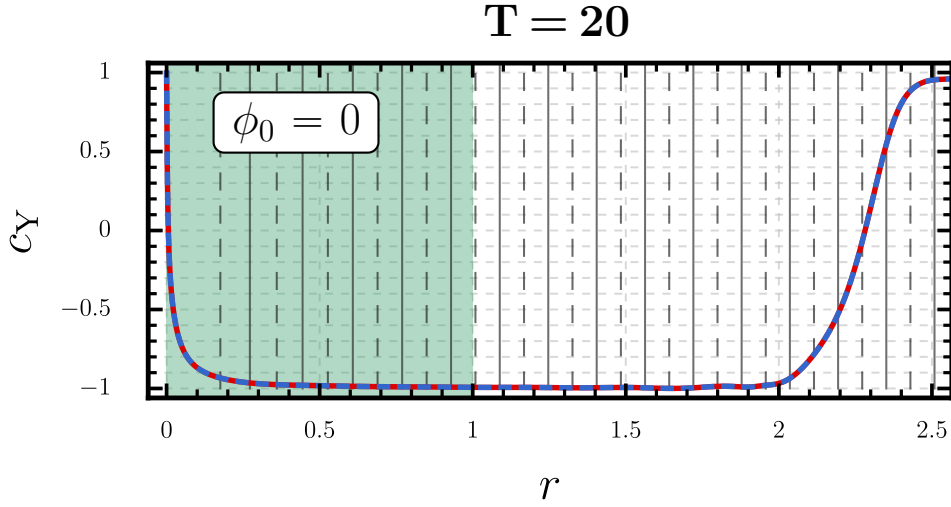


Figure 8.3: Chirality c_Y for EP-centered circular loops starting at $\phi_0 = 0$ given an initial loss state ψ_- (blue, dashed) or an initial gain state ψ_+ (red, solid) as a function of the radius r . The loop time is set at $T = 20$ and the damping at $\gamma = 1$. The gray vertical lines mark the half-integer (dashed) and integer (solid) values of ν . The loop needs a minimal radius to be chiral and stays chiral whenever only the EP_+ is enclosed in the loop (green shaded area). Chirality sustains also when the EP_- ($r > 1$) is enclosed, up to a radius r^* where a transition sets in ($c_Y(r^*) = 0$) and all loops become non-chiral.

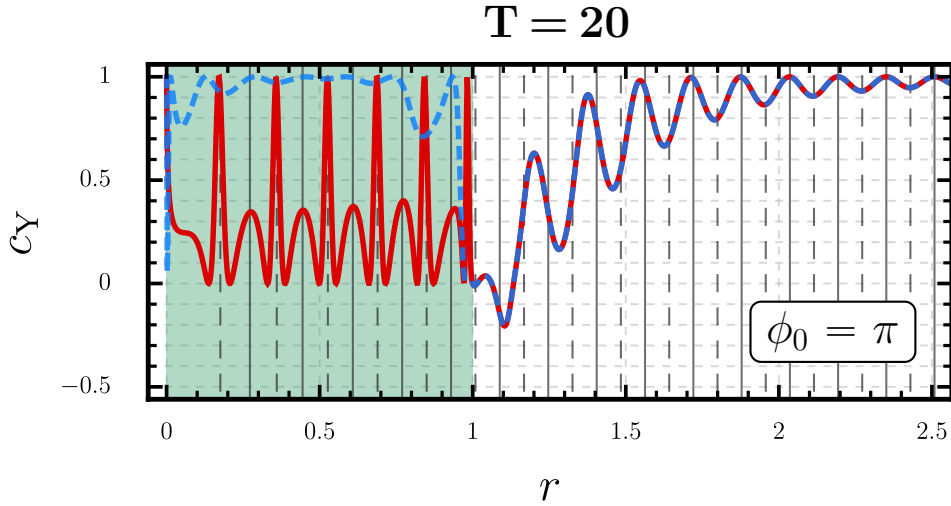


Figure 8.4: Chirality c_Y for EP-centered circular loops starting at $\phi_0 = \pi$ given an initial loss state ψ_- (blue, dashed) or an initial gain state ψ_+ (red, solid) as a function of the radius r . The loop time is set at $T = 20$ and the damping at $\gamma = 1$. The gray vertical lines mark the half-integer (dashed) and integer (solid) values of ν . If $r < 1$ only the EP_+ is enclosed in the loop (green shaded area) and the result is always non-chiral showing the sharp peaks at the half-integer orders ν for ψ_+ . When the EP_- is also enclosed ($r > 1$) all loops converge towards being non-chiral.

8.2 Multiple rounds

Due to the unimodular eigenvalues of the one-cycle evolution operator $U(T)$ and its resulting behavior for multiple loops around the EP (see Eq. 7.53) the chiral behavior becomes more complex for $m > 1$ rounds. As all the appearing effects for multiple rounds already show up for $m = 2$ we restrict our analysis to this case. According to Eq. 7.53, $U(2T) = -\mathbb{1}$ at the half-integer values of ν independent on the initial position ϕ_0 . So every loop with $\nu = n + 1/2$, $n \in \mathbb{N}$ is non-chiral even for $\phi_0 = 0$. The chirality after two loops starting at $\phi_0 = 0$ is shown in Fig. 8.5. We see that the non-chiral peaks are extremely narrow and located exactly at the half-integer values of ν . The general behavior of the chirality is almost the same as for one cycle, i.e. still chiral up to a certain radius where the chirality breaks down.

For starting points at $\phi_0 = \pi$ the chirality after two consecutive loops is depicted in Fig. 8.6. At the half-integer values of ν both modes do not transfer as $U(2T) = -\mathbb{1}$ and $c_Y = 1$. The additional peaks that appear only for the ψ_+ state are located at $\nu = n \pm 1/3$, $n \in \mathbb{N}$ and correspond to a perfect transfer to the other eigenvector at the end of the loop.

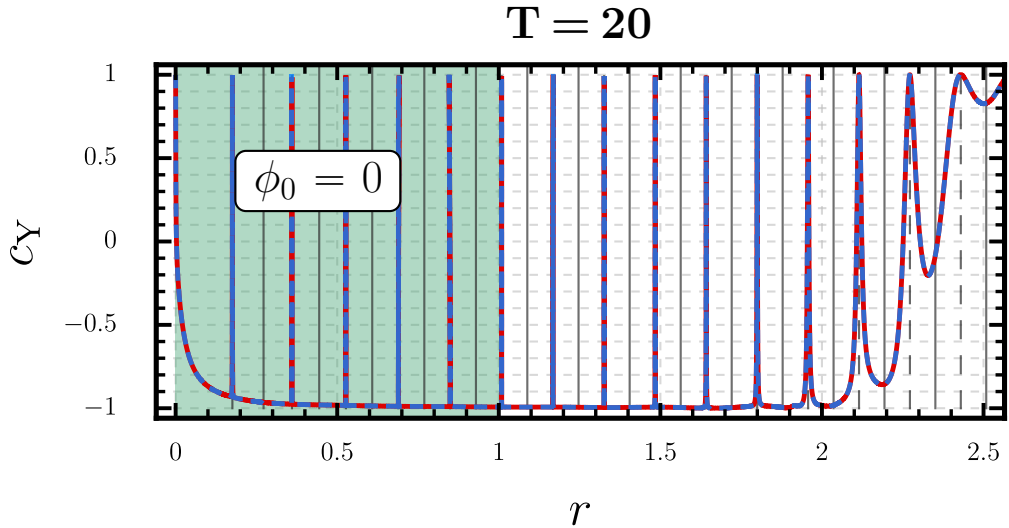


Figure 8.5: Chirality c_Y at $\phi_0 = 0$ of an initial loss state ψ_- (blue, dashed) and an initial gain state ψ_+ (red, solid) as a function of the radius r when the same EP-centered circular loop is performed twice. The loop time is set at $T = 20$ and the damping at $\gamma = 1$. The gray vertical lines mark the half-integer (dashed) and integer (solid) values of ν . As the two-cycle evolution operator yields $U(2T) = -\mathbb{1}$ at the half-integer values of ν , the chirality has very sharp peaks at those positions whereas the overall behavior is very similar to the one-cycle case with the non-chiral transition at $r^* \approx 2$.

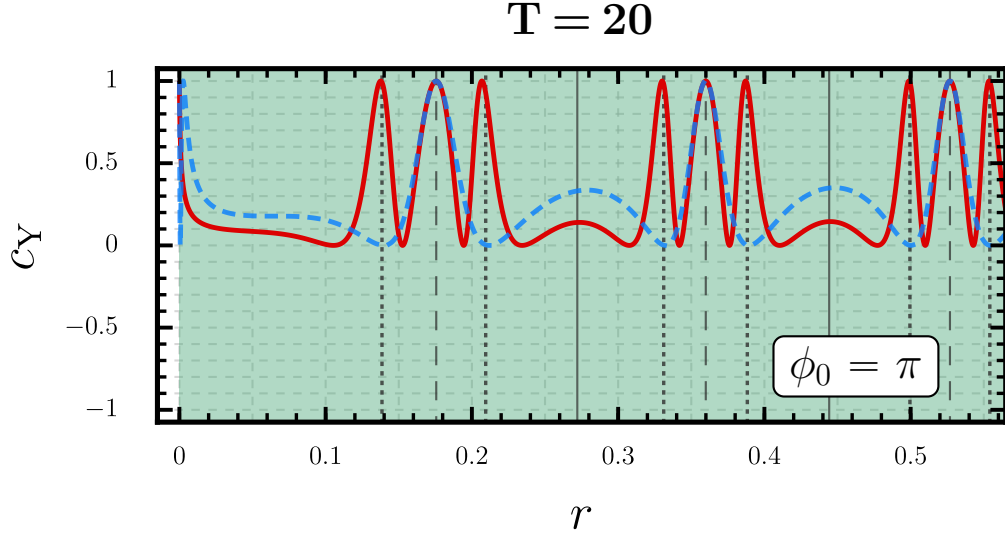


Figure 8.6: Chirality c_Y at $\phi_0 = \pi$ of an initial loss state ψ_- (blue, dashed) and an initial gain state ψ_+ (red, solid) as a function of the radius r when performing the same EP-centered circular loop twice. The loop time is set at $T = 20$ and the damping at $\gamma = 1$. The gray vertical lines mark the half-integer values (dashed), integer values (solid) and integer thirds (dotted) of ν . If $r < 1$ only the EP $_+$ is enclosed in the loop (green shaded area) and the result is always non-chiral. The additional peaks at $\nu = n \pm 1/3$ appear only for the ψ_+ state and correspond to $t_E \approx 1$ in both directions.

8.3 Half-integer order ν

As the Bessel functions of half-integer order $\nu = n + 1/2, n \in \mathbb{N} \setminus \{0\}$ reduce to trigonometric (hyperbolic) functions, we can analyze those solutions in detail to show their chiral behavior. In particular we study the starting positions $\phi_0 = 0$ and $\phi_0 = \pi$.

For a given loop time T the half-integer solutions are located at

$$r = \frac{\pi}{2T} \sqrt{4n(n+1) - 3} \quad (8.2)$$

where $n \geq 1$ for $r > 0$. For every half-integer order the Bessel function can be expanded in the hyperbolic functions $\cosh(z)$ and $\sinh(z)$ as

$$I_{n+1/2}(z) = s_n(z) \sinh(z) + p_n(z) \cosh(z). \quad (8.3)$$

By factoring out the $\cosh(z)$, the remaining expression only contains a $\tanh(z)$

$$I_{n+1/2}(z) = \cosh(z) [p_n(z) + s_n(z) \tanh(z)], \quad (8.4)$$

where the functions $s_n(z)$ and $p_n(z)$ are then Laurent polynomials over the field of rational numbers.

First case: $\phi_0 = 0$

According to the previous results an EP-centered loop starting at $\phi_0 = 0$ should give a chiral result as long as it is in the quasi-adiabatic regime.

The mixing angle θ for the transformation from $U(T)$ to the eigenbasis of $H(T)$ reads

$$\theta(\phi_0 = 0) = -\frac{\pi}{2} + \frac{i}{2} \log(1 + \tilde{s}) , \quad (8.5)$$

with $\tilde{s} = \gamma/r = \gamma T/(2a\pi)$. The exact expression for the ccw one-cycle time evolution operator $U_{\text{EB}}(T)|_{\nu=n+1/2}$ can be written as

$$U_{\text{EB}}^{\text{G}}(T) = \frac{\cosh(4a\sqrt{\tilde{s}})}{\tilde{s}^\nu \sqrt{1 + \tilde{s}}} \begin{pmatrix} -iA_\nu & B_\nu \\ C_\nu & iA_\nu \end{pmatrix} , \quad (8.6)$$

where $A_\nu, B_\nu, C_\nu \in \mathbb{R}$. Any multiplier in U_{EB} will drop out when we calculate the chirality. The remaining hyperbolic tangent with real argument x (see Eq. 8.4) in A_ν, B_ν, C_ν is bound $x \geq 0 : \tanh(x) \in [0, 1]$. It can be easily shown that the cw operator in the eigenbasis is then given by

$$U_{\text{EB}}^{\text{C}}(T) = \left(U_{\text{EB}}^{\text{G}}(T) \right)^T \quad (8.7)$$

that is the transpose of the ccw one-cycle operator. The chirality takes on an easy form as well in this case and is exactly the same for both initial states

$$c_{Y\nu}^\pm = \left(\frac{|A_\nu|^2 - |B_\nu|^2}{|A_\nu|^2 + |B_\nu|^2} \right) \left(\frac{|A_\nu|^2 - |C_\nu|^2}{|A_\nu|^2 + |C_\nu|^2} \right) . \quad (8.8)$$

In the analysis of Eq. 8.8 three different regimes for $\tilde{s} = \gamma/r$ have to be distinguished: for $\tilde{s} < 1$ the loop encloses both exceptional points (EP₊ and EP₋). At $\tilde{s} = 1$ the EP₋ at $g = -\gamma/2$ is passed through and for $\tilde{s} > 1$ only the EP₊ is encircled. Of course the expression for $c_Y^\pm(\tilde{s})$ is cumbersome, but the hyperbolic tangent can be set to $\tanh(4a\sqrt{\tilde{s}}) \rightarrow 1$, which is a good approximation for $\tilde{s} \gtrsim 1$ already. The chirality function can then be expanded in a Taylor series for $\tilde{s} \rightarrow \infty$ that gives a compact form for $c_{Y\nu}^\pm(\tilde{s})$

$$c_{Y\nu}^\pm(\tilde{s}) = -1 + \frac{1}{2\tilde{s}(\nu+1)} + \frac{2}{(2\tilde{s}(\nu+1))^{3/2}} + \frac{4\nu^2}{(2\tilde{s}(\nu+1))^2} + \mathcal{O}\left(\tilde{s}^{5/2}\right) \quad (8.9)$$

that nicely shows the fact that the solution at $\phi_0 = 0$ is always chiral as long as only one EP is encircled. The approximation in Eq. 8.9 is of course only valid for $\tilde{s} \geq 1$.

At $\tilde{s} = 1$ when the EP₋ is passed through the exact solution for the lowest half-integer order $\nu = 3/2$ is already chiral $c_{Y\nu=3/2}^\pm(\tilde{s} = 1) = -0.17$. The exact behavior of c_Y with a starting position $\phi_0 = 0$ for half-integer $\nu = \{3/2, 5/2, 7/2\}$ is depicted in Fig. 8.7. For

loops that are encircling both EPs ($\tilde{s} = \gamma/r < 1$) the chirality oscillates, but as soon as only one EP is encircled ($\tilde{s} > 1$) the solution is always chiral and tends towards $c_Y = -1$ for $\tilde{s} \gg 1$. For the half-integer solutions the loop time T depends on the radius r and on the order ν via

$$T(r) = \frac{\pi}{r} \sqrt{\nu^2 - 1}, \quad (8.10)$$

which means that at a given radius r a larger order ν entails a larger loop time T . This accounts for the fact that the higher orders converge faster towards $c_Y \rightarrow -1$.

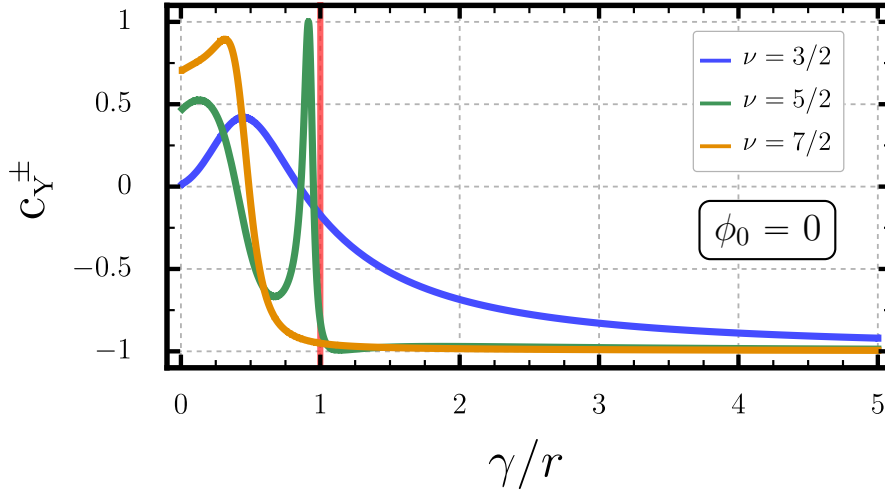


Figure 8.7: Chirality c_Y of an initial ψ_- or ψ_+ eigenstate for EP-centered circles with a starting position $\phi_0 = 0$ (imaginary crossing) as a function of the ratio $\gamma/r = \tilde{s}$ in the case of the three lowest half-integer orders of the Bessel functions ($\nu = 3/2, 5/2, 7/2$). For $\gamma/r < 1$ both EPs are encircled and the chirality oscillates. As soon as only one EP is enclosed ($\gamma/r \geq 1$) the solution is however always chiral in accordance with Eq. 8.9. The vertical, red line indicates the loop that exactly passes through the EP₋.

Second case: $\phi_0 = \pi$

By starting the loop at $\phi_0 = \pi$ we should find that every loop that encloses only one EP is non-chiral. For the mixing angle one has to distinguish between loops that enclose both EPs ($0 < \tilde{s} < 1$) and only one EP ($\tilde{s} > 1$)

$$\begin{aligned} \theta(\phi_0 = \pi) &= \frac{\pi}{2} + \frac{i}{2} \log(1 - \tilde{s}) , \quad 0 < \tilde{s} < 1 \\ \theta(\phi_0 = \pi) &= \quad + \frac{i}{2} \log(\tilde{s} - 1) , \quad 1 < \tilde{s} . \end{aligned} \quad (8.11)$$

The case $\tilde{s} = 1$ has to be excluded as θ is ill-defined at the EP.

For $1 < \tilde{s}$ the calculation for the chirality follows the same procedure as before if we adapt the prefactor of the time evolution operator

$$U_{\text{EB}}^{\text{G}}(T) = \frac{\cos(4a\sqrt{\tilde{s}})}{\tilde{s}^\nu \sqrt{1-\tilde{s}}} \begin{pmatrix} -iA_\nu & B_\nu \\ C_\nu & iA_\nu \end{pmatrix} \quad (8.12)$$

where $A_\nu \in \mathbb{R}$ but $B_\nu, C_\nu \in \mathbb{C}$. Figure 8.8 shows for $\phi_0 = \pi$ the three lowest half-integer

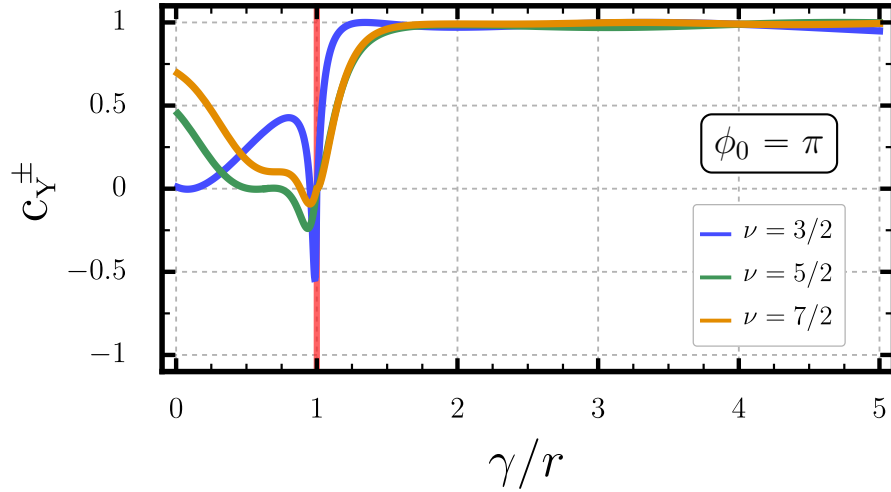


Figure 8.8: Chirality c_Y of an initial ψ_- or ψ_+ eigenstate for centered circles with a starting position $\phi_0 = \pi$ (real crossing) as a function of the ratio $\gamma/r = \tilde{s}$ in the case of the three lowest half-integer orders of the Bessel functions ($\nu = 3/2, 5/2, 7/2$). For $\gamma/r < 1$ both EPs are encircled and the chirality varies. At $\gamma/r \geq 1$ the solution is however always non-chiral. The vertical, red line indicates the loop where the EP₋ is start and end point of the loop.

orders $\nu = 3/2, 5/2, 7/2$ as a function of the ratio $\tilde{s} = \gamma/r$. Again, if both EPs are encircled ($0 < \tilde{s} < 1$) then the chirality oscillates. But in the case of $\gamma/r = \tilde{s} = 1$, when the second EP is the starting and end point of the loop, the chirality has to vanish because $p_I^{\text{G}} = 0$ and $p_I^{\text{C}} = 0$. This happens as the eigenvector populations are evened out at the EP. Whenever the ratio $\tilde{s} > 1$, every loop encircles only one EP and the solution is always non-chiral and stays that way for every evolution time T . This can be seen by neglecting the oscillatory terms in the exact expression for the population inversion and approximating the result for $\tilde{s} \rightarrow \infty$

$$\text{PI}_\nu^{\oplus} = \text{PI}_\nu^{\oplus} \approx \frac{\tilde{s}(\tilde{s} - 1)}{\left(\tilde{s} - \frac{1}{2} \left(\frac{5-\nu^2}{1-\nu^2}\right)\right)^2}, \quad \tilde{s} \geq 1 \quad (8.13)$$

where the chirality is then of course always a positive number $c_{Y\nu}^\pm = \left(\text{pr}_\nu^\oplus\right)^2, \forall \nu$. The validity of this approximation is displayed in Fig. 8.9 where it is clearly visible that the amplitude of the oscillations in c_Y falls off rapidly with increasing \tilde{s} for which reason the approximation in Eq. 8.13 is very accurate even for rather small \tilde{s} .

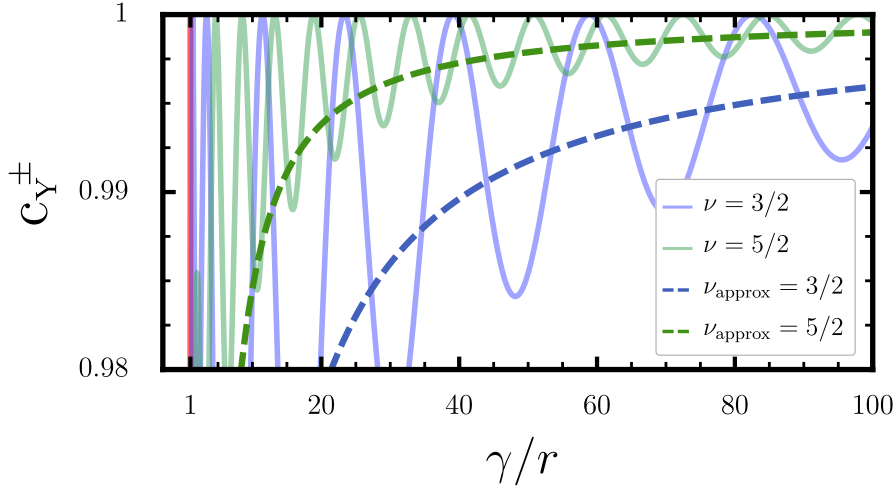


Figure 8.9: Exact (solid) and approximate (dashed) solution for the chirality c_Y of an initial ψ_+ or ψ_- eigenstate for EP-centered circles with a starting position $\phi_0 = \pi$ as a function of the ratio $\gamma/r = \tilde{s} > 1$ for $\nu = 3/2, 5/2$. The narrow range on the y -axis shows that the amplitude of the oscillations in c_Y decreases quickly with \tilde{s} and the approximation in Eq. 8.13 is therefore very accurate. The $\nu = 7/2$ solution has been neglected for visibility reasons.

Third case: $0 < \phi_0 < \pi$

In the case of an arbitrary starting position $0 < \phi_0 < \pi$ we need to make use of the general relation for the reverse time evolution operator (see Eq. 7.61) in the basis constituted by P . The relation between the ccw and the cw one-cycle time evolution operator in the eigenbasis is still the same $U_{\text{EB}}^{\text{C}}(T) = \left(U_{\text{EB}}^{\text{G}}(T)\right)^T$.

As the long time limit $T \rightarrow \infty$ suggests that every loop for EP-centered circles is chiral (except $\phi_0 = \pi$) there must be a finite time T^* at which a solution starting at ϕ_0 becomes chiral. The time T^* at which chirality sets in ($c_Y \leq 0$) fulfills

$$p_{\text{I}}^{\text{C}}(T^*) = 0 \quad \vee \quad p_{\text{I}}^{\text{G}}(T^*) = 0 \Rightarrow c_Y(T^*) = 0. \quad (8.14)$$

This definition can thus be used to calculate T^* for every initial position ϕ_0 , which is shown in Fig. 8.10 for the three lowest half-integer values $\nu = \{3/2, 5/2, 7/2\}$. If $\tilde{s} > 1$ then only the positive EP is encircled and for $\tilde{s} > 2$ it holds furthermore that $g > 0$ during the evolution. A distinction is therefore made between loops with $1 < \tilde{s} < 2$ (dashed

lines) and $2 < \tilde{s}$ (solid lines) where $\tilde{s} = \gamma/r$. The lines shown in Fig. 8.10 therefore separate the chiral (below) from the non-chiral (above) regions.

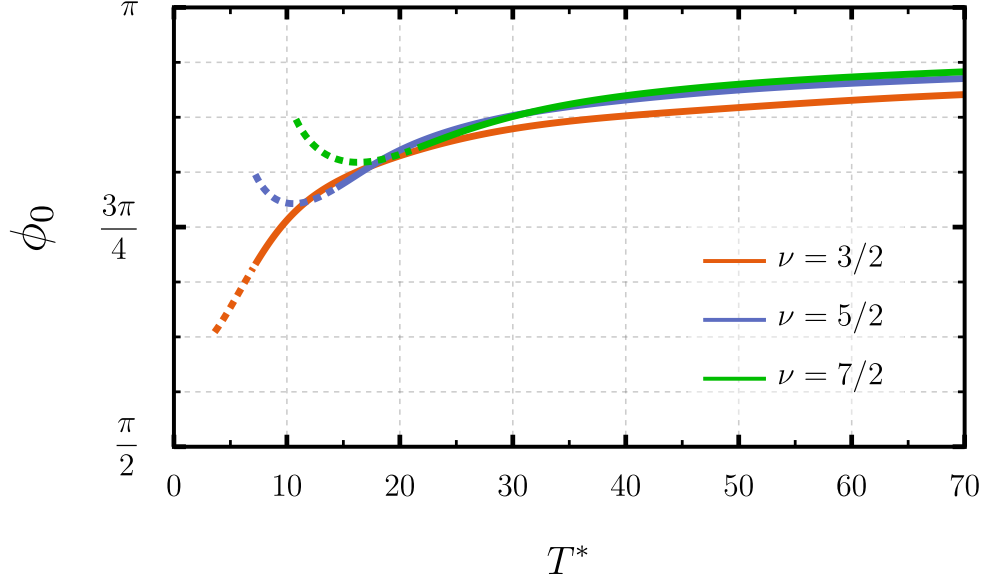


Figure 8.10: Transition time T^* where chirality sets in ($c_Y(T^*) = 0$) for the half-integer order solutions as a function of the starting position ϕ_0 for EP-centered circles with $\gamma = 1$. The dashed lines display loops with $1 < \tilde{s} < 2$ where only one EP is encircled but g is not strictly positive throughout the whole loop. The solid lines correspond to loops with $g > 0$ during the entire propagation.

8.4 Asymptotic expansion of $U(T)$ at $\phi_0 = 0$

We have shown in Fig. 8.3 that circular loops starting at the imaginary crossing $\phi_0 = 0$ are chiral even when both EPs are enclosed ($r > \gamma = 1$) up to a certain radius ($r^* \approx 2.277$) where chirality breaks down. In order to verify the robust chiral behavior for $r < r^*$ and to get an analytical expression for this chiral boundary we asymptotically expand the exact one-cycle time evolution operator in the mode basis $U_{\text{MB}}(T) = PU(T)P^{-1} \leftrightarrow (a(T), b(T))^T$.

The one-cycle operator in the $(\alpha(t), \beta(t))$ basis was given in Eq. 7.52 as

$$U(T) = \begin{pmatrix} -\frac{i\pi}{2\kappa}(G_+\dot{G}_-) - \cos(\pi\nu) & \frac{i\pi c}{2\kappa^2}\dot{G}_+\dot{G}_- \\ -\frac{2\pi i}{c}G_+G_- & \frac{i\pi}{2k}(G_+\dot{G}_-) - \cos(\pi\nu) \end{pmatrix}$$

with $G_{\pm} = \kappa I_{\pm}(2a\kappa)$, $\nu = \sqrt{1 + 4a^2}$, $a = rT/(2\pi)$ and $\kappa = \sqrt{\gamma/r} \exp(i\phi_0/2)$. At $\phi_0 = 0$ we find $\kappa = \sqrt{\gamma/r} =: s$. Above we had $\tilde{s} = \gamma/r$ where now we use $s = \sqrt{\gamma/r}$. A key

observation here is that the condition for quasi-adiabaticity is $\nu^2 \gg 1$ so that it is valid to say $a \approx \nu/2$. Then all the appearing Bessel functions and their derivatives have order $\pm\nu$ and argument νs , which has exactly the right form so that we can use the uniform asymptotic expansion for the Bessel functions (Eq. 7.47), with $z = s \Rightarrow \eta = \sqrt{1+s^2} + \ln(s/(1+\sqrt{1+s^2}))$. We need to substitute the negative orders $-\nu$ using the connection formula

$$I_{-\nu}(z) = I_{\nu}(z) + (2/\pi) \sin(\nu\pi) K_{\nu}(z)$$

for positive ones though. It is apparent in the uniform asymptotic expansion that if $\nu\eta \gg 1 \Rightarrow I_{\nu}(\nu s) \gg K_{\nu}(\nu s) \wedge I'_{\nu}(\nu s) \gg K'_{\nu}(\nu s)$. Hence we can drop all the K_{ν} in favor of the I_{ν} (and corresponding derivatives) and then apply the asymptotic expansion. The final result for the approximate transfer efficiency given initial eigenstates ψ_- or ψ_+ in the ccw direction

$$t_{\text{E}}^{\ominus} = \frac{1}{1 + \left(1 + \frac{2}{s^2} + \frac{4\gamma T \sqrt{s^2+1}}{\pi s^4}\right)^2}, \quad (8.15)$$

$$t_{\text{E}}^{\oplus} = \frac{1}{1 + \left(\frac{\pi s^2}{2\gamma T \sqrt{s^2+1}}\right)^2}, \quad (8.16)$$

nicely shows that in the long time limit an initial loss state returns to itself $t_{\text{E}}^{\ominus}|_{T \rightarrow \infty} = 0$ and initial gain state transfers its population $t_{\text{E}}^{\oplus}|_{T \rightarrow \infty} = 1$. Equations 8.15 and 8.16 are however only valid if $\nu \approx 2a$ and $\nu\eta \gg 1$.

The first condition can always be fulfilled by choosing a large enough loop time so that $rT \gg 1$. As η depends only on $s = \sqrt{\gamma/r}$, the second condition is not satisfiable when η becomes negative, which is exactly the point where chirality breaks down. This is demonstrated in Fig. 8.11 where the transfer efficiency of the exact analytical solution (circles and squares) is displayed together with the approximate solution from above for an initial gain state (ψ_+ , red) and initial loss state (ψ_- , blue). For radii $r \lesssim 0.2$ the condition $\nu \approx 2a$ is not fulfilled so the approximation deviates from the exact result. When we increase the radius, the results coincide up to the value r^* where η has a root (black, vertical line), $\eta(r^*) = 0$. There, the overall behavior of t_{E}^{\oplus} reverses and no population is transferred anymore. The position of the root of η , so the position of the breakdown of chirality, does not depend on the loop time T but only on $s = \sqrt{\gamma/r}$. The width of this transition (two vertical, dotted lines) however is determined by the product $\nu\eta$ and therefore depends on T . The lower boundary r_l is located at $\nu\eta = 1$ and upper boundary r_u at $\nu\eta = -1$. A robust chiral state conversion for loops that encircle both EPs is only obtained for $\gamma < r < r_l$. The transcendental equation that determines r^* reads

$$\sqrt{1 + \frac{\gamma}{r^*}} - \ln \left(\frac{1 + \sqrt{1 + \frac{\gamma}{r^*}}}{\sqrt{\frac{\gamma}{r^*}}} \right) = 0, \quad (8.17)$$

with the numerical solution $r^* \approx 2.277\gamma$. The width of the transition $|r_l - r_u|$ can be made arbitrarily small by increasing the loop time T . We can therefore say that r^* constitutes a phase boundary in terms of chirality. The fact that it is not possible to have chiral loops for $r > r^*$ is clearly visible in Fig. 8.12 where we extended the range of starting points $\{g_0, \omega_0\}$ in the chirality map of Fig. 8.1 for $T = 20$. The loops are again centered at the EP₊ (red cross). All the chiral loops (blue region) have a radius $r < r^*$. Interestingly, starting to the left of the EP₋ ($\phi_0 = \pi, r > \gamma$) does not yield a chiral loop even for $r < r^*$. This is because the general derivation uses $s = \sqrt{\gamma/r} \exp(i\phi_0/2)$ and it is exactly this phase that we did not include in the calculations for r^* . A natural generalization for the phase boundary is then $r^* = 2.277\gamma \cos(\phi_0/2)$ that resembles the exact demarcation in Fig. 8.12 up to a very good degree.

At this point we conclude the analysis of the EP₊-centered circles. We have rigorously shown that chirality is strongly influenced by the starting position ϕ_0 and that quasi-adiabaticity is also only locally defined and needs to be adjusted for every starting point. Then we established that every quasi-adiabatic loop that encircles one EP at $\phi_0 = 0$ is always chiral whereas $\phi_0 = \pi$ does not admit a chiral solution. Although it is possible to have an asymmetric switching behavior of the modes even when both EPs are encircled, we proved that the chiral effect is still inseparably linked to closed contours in the vicinity of an EP. This was demonstrated by showing that there is a sharp demarcation at a radius r^* that separates chiral from non-chiral regions.

Finally, the asymptotic expansion for $\phi_0 = \pi$ has not been carried out because we already know that it has an oscillatory behavior. This can be comprehended by analyzing the appearing Bessel functions at $\phi_0 = \pi$. There the solution consists of Bessel functions of the first kind $J_\nu(z)$ with the connection formula

$$J_{-\nu}(z) = J_\nu(z) \cos(\nu\pi) - Y_\nu(z) \sin(\nu\pi)$$

to get rid of negative orders of ν like before. Now due to the sine and cosine the overall solution oscillates. Also if $s < 1$ (only EP₊ inside the loop) neither one of the $J_\nu(z), Y_\nu(z)$ can be neglected in favor of the other.

The clear cut between EP-enclosing and non-enclosing loops (see Fig. 8.4) is however evident in the asymptotic expansion when $s > 1$, that is when both EPs are encircled. The asymptotic behavior changes from oscillatory to exponentially amplified/damped leading inevitably to non-chiral solutions.

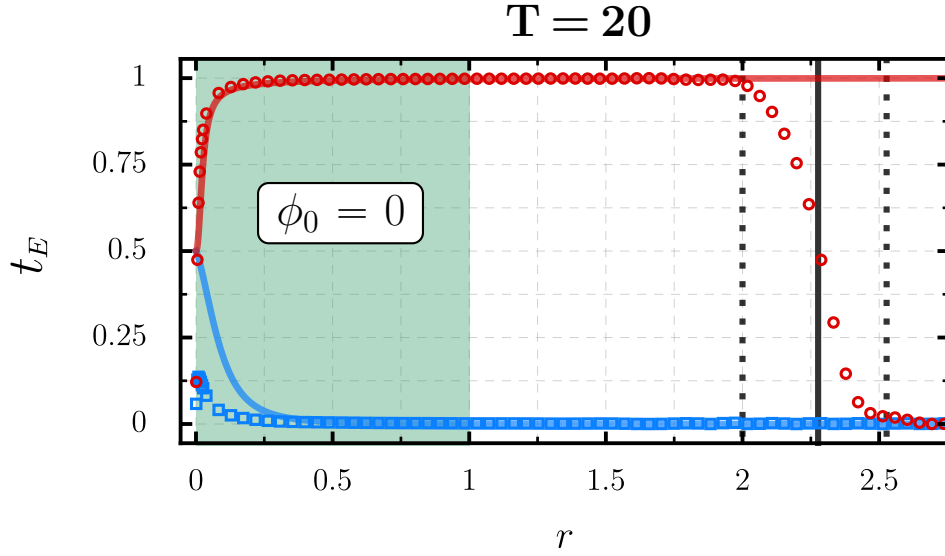


Figure 8.11: Transfer efficiency t_E at $\phi_0 = 0$ of an initial loss state ψ_- (blue) and an initial gain state ψ_+ (red) for an EP-centered circle with radius r . The loop time is set at $T = 20$ and the damping at $\gamma = 1$. The (blue and red) solid lines are the approximations that stem from the asymptotic expansion and the markers (circles and squares) correspond to the respective exact values obtained from the full analytical solution. The black vertical lines (dotted and solid) are positioned at the radii where $\nu\eta = \{1, 0, -1\}$ and confine the region where the transition from chiral to non-chiral loops occurs.

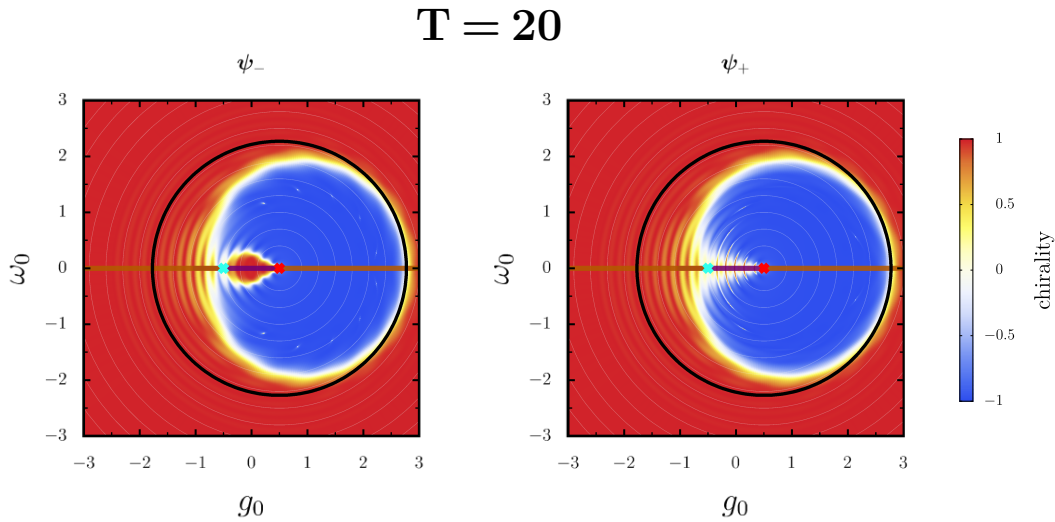


Figure 8.12: Chirality for circular loops with starting points at $\{g_0, \omega_0\}$ that are centered around the EP₊ (red cross) with $\gamma = 1$. The left column displays initial ψ_- states and the right column ψ_+ states at the respective initial position. The EP₋ is marked with a cyan cross. The radius of the black circle is $r^* = 2.277$ so it constitutes the demarcation between the chiral and non-chiral regions. The orange/purple line shows the imaginary/real crossing of the eigenvalues.

9 Results for general circular paths

In the case of EP-centered circles we have rigorously shown that chirality is not limited to contours that enclose a single EP. In fact, there is no indication in the transfer efficiency or in the chirality that points out how many EPs are enclosed in the loop. The EP-centered loops from the previous chapters, however, do not allow to investigate the case where no EP is encircled and therefore we extend the loop parametrization

$$\begin{aligned} g(t) &= g_c + r \cos\left(\frac{2\pi t}{T} + \phi_0\right) \\ \omega(t) &= \omega_c + r \sin\left(\frac{2\pi t}{T} + \phi_0\right) \\ \gamma(t) &= \gamma \end{aligned} \tag{9.1}$$

so that the center of the circle $\{g_c, \omega_c\}$ can be moved in the $\{g, \omega\}$ -plane. We set $\omega_c = 0$ throughout this chapter as it is obvious that chirality is only obtainable if the imaginary crossing is passed at least once and the analysis of the influence of ω_c is therefore trivial. Although there is an analytical solution for general circular loops (not necessarily EP-centered) in the $\{\omega, \gamma\}$ -plane [31], there is no known analytical solution for general circles in the $\{g, \omega\}$ -plane. As it would go beyond the scope of this work to derive another analytical solution for a different choice of parameters we refrain from doing so and switch to solely numerical solutions instead.

There are in general two interesting cases to examine:

1. When we fix the radius ($r < \gamma$)¹⁴ and move the center of the circle g_c along the g -axis, we are interested in determining the phase boundaries of the chiral phase especially when no EP is enclosed in the loop.
2. The alternative way is to fix the center g_c at $g_c > g_{\text{EP}+}$ and successively increase the radius to explore the chiral regions there and to compare the efficiency of the asymmetric switch for loops that include zero, one or two EPs.

9.1 Fixed radius, variable center

To tackle the first point we consider a circular loop with radius $r < \gamma$ so that at most one EP is enclosed in the loop. This is demonstrated in Fig. 9.1 for a circular path with $r = 0.3$ and $T = 20$. In the lower panel of this plot we show the chirality as a function of

¹⁴In this case at most one EP is enclosed in the loop.

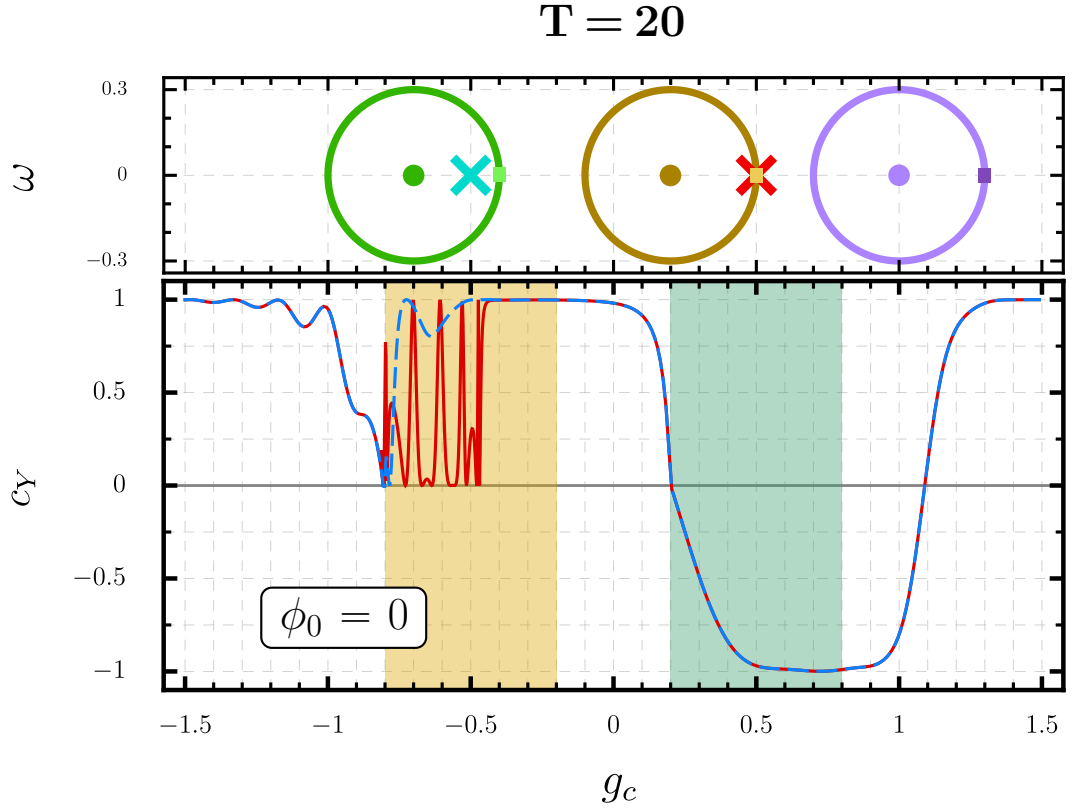


Figure 9.1: Three illustrative circular loops with center $\{g, \omega\} = \{g_c, 0\}$ and a start position $\phi_0 = 0$ (small rectangles). The EP_- and EP_+ are displayed as cyan and red crosses respectively (top panel). Chirality c_Y at $\phi_0 = 0$ of an initial loss state ψ_- (blue, dashed line) and an initial gain state ψ_+ (red, solid line) for circular loops with $r = 0.3$ and center at $\{g, \omega\} = \{g_c, 0\}$ (bottom panel). The loop time is set at $T = 20$ and the damping at $\gamma = 1$. The circle encloses the EP_+ for $g_c - r < \gamma/2 < g_c + r$ (green shaded area) and the EP_- for $g_c - r < -\gamma/2 < g_c + r$ (yellow shaded area). Chirality sets in when the EP_+ is start and end point of the loop and prevails up to a value $g_c^* > \gamma/2 + r$, where no EP is encircled.

the circle's center g_c on the g -axis for an initial ψ_+ (red, solid line) and an initial ψ_- state (blue, dashed line). The green and yellow shade indicate that the loop encloses the EP_+ or EP_- respectively. The upper panel illustrates three exemplary circular paths along with the EP_- (cyan cross) and the EP_+ (red cross). As we already know that chirality is contingent on a certain closeness to the EP, it is not surprising that contours are not chiral if $g_c \gg g_{\text{EP}_+}$ or $g_c \ll g_{\text{EP}_-}$. We observe however, that for $\phi_0 = 0$ a chiral phase is only present in the vicinity of the EP_+ . Similar to the case above where chirality persisted even when both EPs were enclosed, the asymmetric switch continues to occur even when the loop does not contain the EP_+ (purple circle in top panel). At a certain distance $g_c^* \approx 1.1$ chirality breaks down ($c_Y(g_c^*) = 0$).

The behavior for $\phi_0 = 0$ around the EP_- is the same as for $\phi_0 = \pi$ at the EP_+ as they are mirror images of one another. Interestingly, a starting point at the real crossing does not admit a chiral phase and distinct non-chiral peaks for ψ_+ appear only if $g_c \lesssim -\gamma/2$.

9.2 Fixed center, variable radius

The second case is examined for circular loops with fixed center $g_c = 1.5$ where we vary the circle's radius r for a starting point $\phi_0 = 0$. In [Fig. 9.2](#) the top panel exhibits three exemplary loops with radii $r = \{0.2, 1.0, 2.0\}$. By fixing the center at $g_c \gg g_{\text{EP}_+}$ we find again that chirality (bottom panel) sets in already when no EP is enclosed at a distance $g_c^*(r)$. Whenever only one EP is encircled the loop is perfectly chiral and at a radius $r^* \approx 3.75$ where the distance to both EPs is large chirality breaks down.

The onset of chirality for non-enclosing loops with $g_c - r > \gamma/2$ is shown in [Fig. 9.3](#). The critical position of the circle's center $g_c^* \geq g_{\text{EP}_+}$ at which the chiral phase is entered, $c_Y(g_c^*) = 0$, is plotted as a function of the loop's radius with $\phi_0 = 0$. The values have been obtained numerically (orange squares) and a least squares fit using a quadratic polynomial (green, solid line) gives

$$g_c^* = 0.500 + 2.140 r - 0.548 r^2, \quad (9.2)$$

for $r \leq 0.7$. The fact that the defining equation for g_c^* is quadratic in r admitting two solutions (r_0, r_2 - encircling zero/two EPs) is clearly visible in the chirality map in [Fig. 9.4](#). We show again the chirality as a function of the initial position $\{g_0, \omega_0\}$ but for circles with center at $\{g_c, \omega_c\} = \{1.5, 0\}$. The EPs are marked with a red (EP_+) and cyan (EP_-) cross. The two numerically obtained solutions for the chiral phase boundary $r_0 = 0.543$ and $r_2 = 3.362$ are drawn on the map as black and white circles respectively. We notice that the second value r_2 is significantly higher than the value $r^* = 2.277$ for EP-centered circles. This is because the distance to the EP_- is the decisive factor for chirality once both EPs are enclosed. By shifting the circle's center g_c to larger values of g the distance to the EP_- shrinks for a given radius and the loop is still chiral.

Also it is apparent that around $\phi_0 = 0$, the chiral phase starts before a single EP is encircled.

We conclude the analysis for general circular loops by emphasizing again that chirality is in fact related to exceptional points, but we have rigorously shown that an asymmetric mode switch does not strictly rely on encircling a single EP. In fact, the asymmetric switch is obtainable in the quasi-adiabatic regime for zero, one or two EPs inside the closed contour. The necessary condition for chirality is an interplay between the circle's radius and its center so that a certain distance to the EP is not exceeded. Like for EP-centered circles, the position of the phase boundary does not depend on the loop time T (not shown in [Fig. 9.3](#)) given that the quasi-adiabaticity condition is met. Only the width of the transition is determined by T (see [section 8.4](#)).

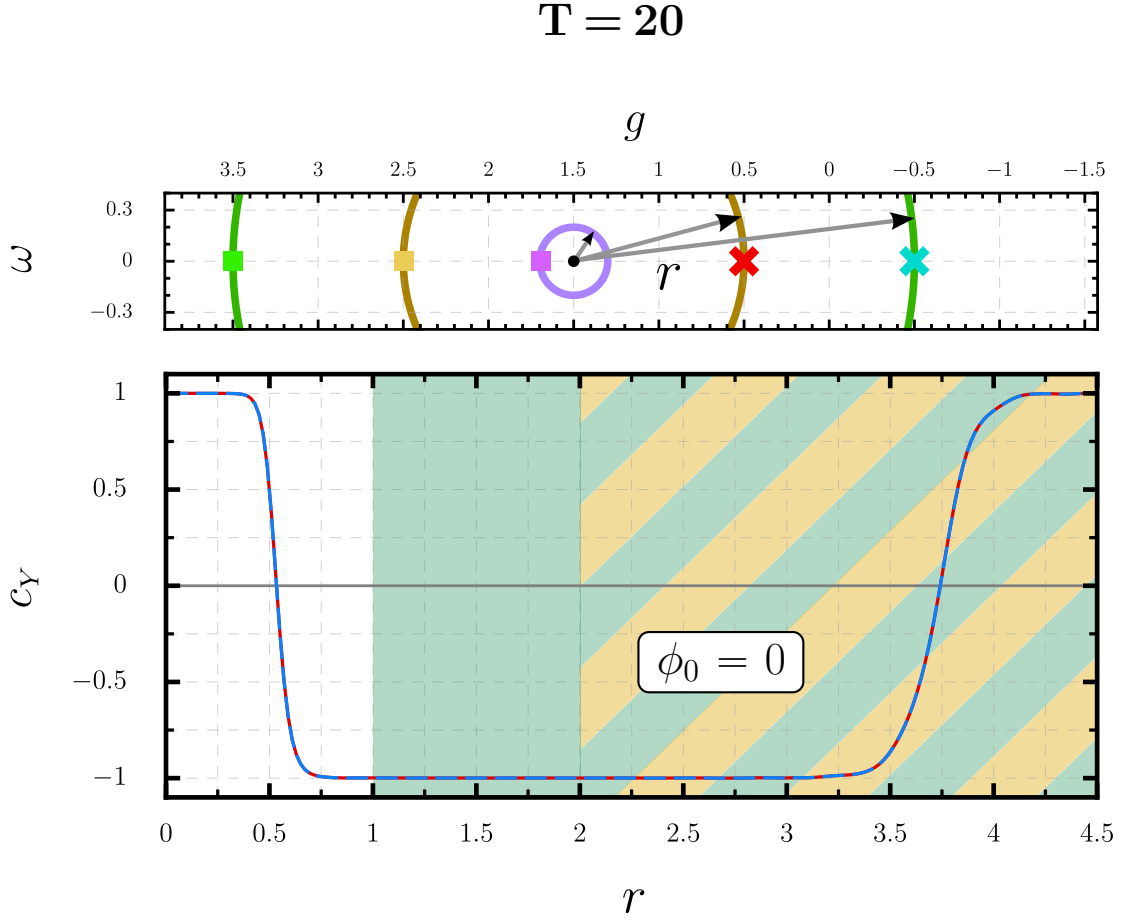


Figure 9.2: Three illustrative circular loops with center at $\{g, \omega\} = \{1.5, 0\}$, start position $\phi_0 = 0$ (small rectangles) and radii $r = \{0.2, 1.0, 2.0\}$. The EP₋ and EP₊ are displayed as cyan and red crosses respectively (top panel). Chirality c_Y at $\phi_0 = 0$ of an initial loss state ψ_- (blue, dashed line) and an initial gain state ψ_+ (red, solid line) for circular loops with center at $\{g, \omega\} = \{1.5, 0\}$ and radius r (bottom panel). The loop time is set at $T = 20$ and the damping at $\gamma = 1$. The circle encloses the EP₊ for $g_c - r < \gamma/2$ (green shaded area) and additionally the EP₋ for $g_c - r < -\gamma/2$ (yellow and green striped area). Chirality sets in even before the EP₊ is encircled and prevails even when both EPs are enclosed in the loop.

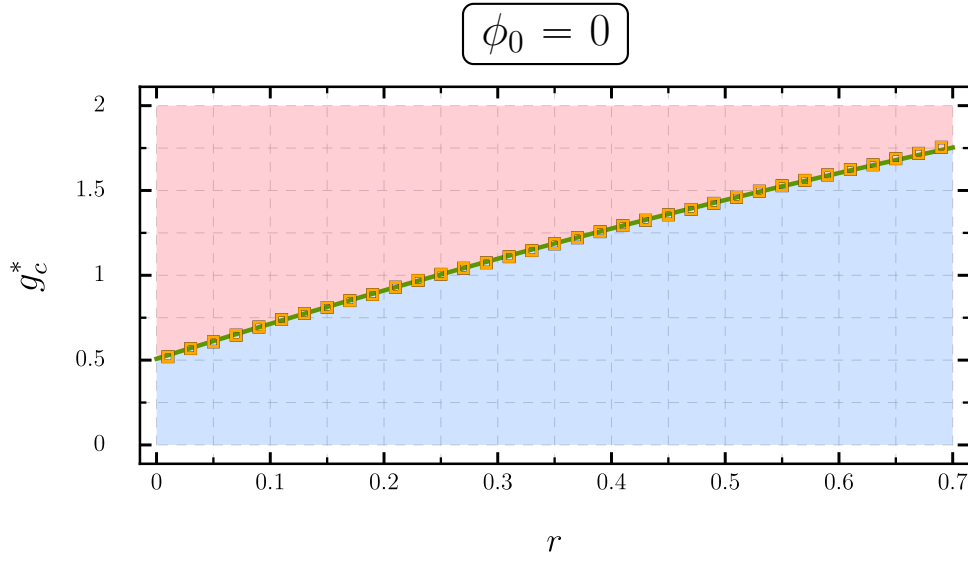


Figure 9.3: Critical position of a circular loop's center g_c^* , where chirality sets in $c_Y(g_c^*) = 0$, as a function of the radius r . The values for g_c^* have been obtained by numerically solving the TDSE for successive values g_c until the condition $c_Y(g_c^*) = 0$ is met using $T = 20$. The green solid lines shows the result of a least squares fit $g_c^* = 0.500 + 2.140r - 0.548r^2$. The red and blue shade correspond to the non-chiral and chiral phase respectively.

T = 20

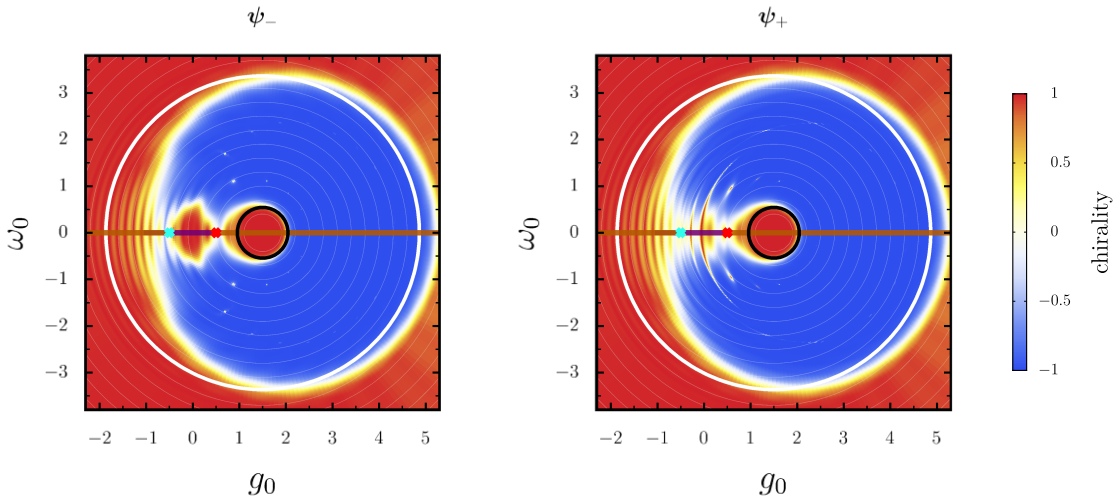


Figure 9.4: Chirality for circular parameter paths with starting points at $\{g_0, \omega_0\}$ that are centered at $\{g_c, \omega_c\} = \{1.5, 0\}$. The left column displays initial ψ_- states and the right column ψ_+ states at the respective initial position. The EP_- and the EP_+ are marked with a cyan and a red cross respectively. The black and white circles mark the approximate phase boundaries of the chiral phase obtained from Eq. 9.2. Chirality is achievable for zero, one or two EPs inside the cyclic path.

10 Results for straight paths

The analytical solution for general straight paths that was given in [chapter 7](#) is extremely versatile as it allows us to concatenate arbitrary parameter paths to form a closed contour, dissect each part of a loop itself or even go through the EP using various different parameter configurations. The prevailing EP related efforts concern mostly dynamical parameter loops around an EP [26, 30–33], but the question of what happens when going through an EP has been left unstudied so far.

10.1 Going into an EP

Up to this point we have only discussed the time-evolution for static parameters at the EP and the projection of a state vector onto the generalized eigenbasis of the EP. In [chapter 5](#) we have shown that $c_h(t)/c_v(t)$, the ratio of the populations of the generalized eigenbasis, linearly converges towards zero at the EP at a pace that is solely determined by the damping rate γ .

We have also demonstrated that the ratio of the eigenvectors becomes $c_-/c_+ = \pm i$ independent of the pace at which the EP is passed. This universal behavior for any path into the EP is illustrated in [Fig. 10.1](#) for a straight path that ends at the EP_+ . We draw the components of the Stokes vector

$$\mathbf{r} = \frac{1}{(1 + |R_-|^2)} (2\Re(R_-), 2\Im(R_-), 1 - |R_-|^2)^T, \quad R_- = \frac{c_-}{c_+} \quad (10.1)$$

for an initial 'gain' state ψ_+ ([Fig. 10.1a](#)) and an initial 'loss' state ψ_- ([Fig. 10.1b](#)) using the straight path parametrization drawn in [Fig. 10.1c](#). The Stokes vector is usually used to describe optical polarization states [27], but it is also convenient to present general mixed states where the first two components carry the information about the relative phase between the expansion coefficients and the third component is equal to the population inversion.

As the parameter path in [Fig. 10.1](#) ends at the EP the value of the Stokes vector must become $\mathbf{r}(t_{\text{EP}}) = (0, 1, 0)^T$ symbolizing the universal ratio $c_-(t_{\text{EP}})/c_+(t_{\text{EP}}) = i$. Although this fixes one of the components and the relative phase, this only happens in the eigenbasis since the eigenvectors are degenerate at the EP. It is important to stress that the behavior of the eigenbasis at the EP does not entail a loss of information as there are no restrictions imposed on the coefficients in any other complete, biorthogonal basis, as e.g. the generalized eigenbasis at the EP. As we did not include any non-linearities (or other time-reversal symmetry breaking mechanisms) throughout this work, time-reversal symmetry must be upheld for any solution of the Schrödinger equation at any time,

which forbids a sudden loss of information.

There is, however, a linear convergence towards a fixed ratio exactly at the EP and we are interested if this convergence sets in already in the vicinity of the EP. We use our analytical solutions for straight parameter paths to look at the expansion coefficients in the Euclidean basis (mode basis) when an EP is approached and reached. In Fig. 10.2 the ratio of the coefficients in the mode basis $a(t_{\text{EP}})/b(t_{\text{EP}})$ at the EP is displayed for increasing total evolution times $T = t_{\text{EP}}$ (indicated by the black arrows) in the range $T \in [0.01, 1000]$. At some time T^* the two initial states $(a_0, b_0)^T = (1, 0)$ and $(a_0, b_0)^T = (0, 1)$ are almost indistinguishable ($T^* \approx 7.5$) as the system has undergone a non-adiabatic transition. For slightly longer times $T \gtrsim 10$ the ratio starts to linearly converge towards its fixed point $a/b = -i$ (red dot) that corresponds to $c_h/c_v = 0$. We conclude that the linear convergence of $c_h/c_v \rightarrow 0$ can also be achieved by dynamically (by)passing an EP. The rate of convergence is however still only determined by the damping $\gamma = 1$ and, for example, cannot be influenced by a different choice for the angle α at which the EP is approached.

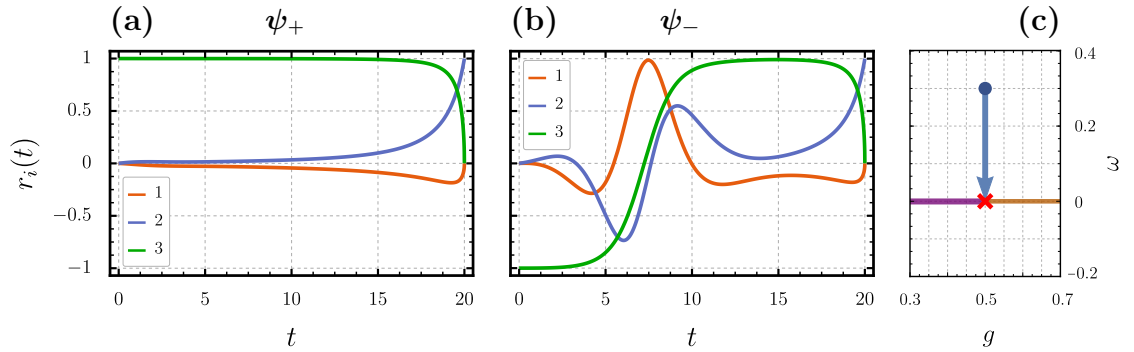


Figure 10.1: Time dependent components of the Stokes vector $r_i(t)$ using a straight parameter path (c) that ends at the EP (red cross) for (a) an initial ψ_+ and (b) an initial ψ_- state. The Stokes vector for the instantaneous eigenbasis is given as $\mathbf{r} = (2\Re(R_-), 2\Im(R_-), 1 - |R_-|^2)^T / (1 + |R_-|^2)$. At the end of the propagation ($t_{\text{EP}} = T$), that is at the EP, the Stokes vector for the eigenbasis takes the value $\mathbf{r}(t_{\text{EP}}) = (0, 1, 0)^T \leftrightarrow c_-/c_+ = i$. The path parametrization follows Eq. 7.7 with $T = 20$, $r = 0.3$, $\{g_0, \omega_0\} = \{0.5, 0.3\}$, $\gamma = 1$ and $\alpha = \pi/2$.

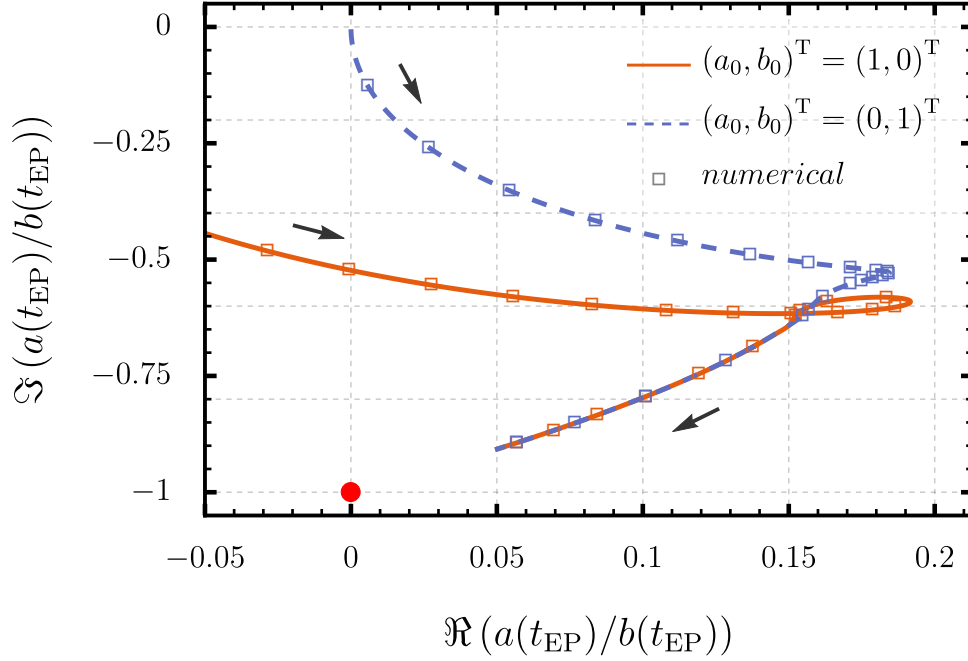


Figure 10.2: Comparison of the analytical (solid and dashed lines) and the numerical result (empty squares) of the ratio $\frac{a(t_{\text{EP}})}{b(t_{\text{EP}})}$ in the complex plane for propagation times $T \in [0.01, 1000]$ for two different initial states. The black arrows point towards increasing evolution times $T = t_{\text{EP}}$. Both results agree perfectly and converge towards $a(t_{\text{EP}})/b(t_{\text{EP}}) \xrightarrow{T \rightarrow \infty} -i$ (red dot), which corresponds to $c_h/c_v = 0$. The parametrization of the path is given by Eq. 7.7 for which $t_{\text{EP}} = T$, $\gamma = 1$, $\alpha = \pi/2$, $r = 1/2$, $\omega_c = r/2$ and $g_c = \gamma/2$.

10.2 Going through an EP

We have established that the eigenvector populations are evened out perfectly at the EP but as the basis is defective, no information loss is connected with this effect. In the mode basis $(a(t), b(t))^T$, for example, the EP is not a special point and the dynamical evolution shows no evidence that an EP has been passed through.

In the eigenbasis though, the EP is clearly visible in the temporal evolution of the expansion coefficients as it is the point in time where $c_-/c_+ = \pm i$. Once the EP is passed the eigenvectors are subject to a distinct gain and loss again and the system therefore undergoes a transition to the gain state destroying the perfectly mixed state. There is a path though that preserves the equalizing property of the EP. We know from chapter 4 that the imaginary crossing is the only norm-preserving parameter region. So by going to the EP and then away from it along the imaginary crossing, the eigenvector coefficients stay perfectly leveled. This is demonstrated in Fig. 10.3 for a straight path that reaches

from the real to the imaginary crossing (Fig. 10.3c). In panel (a) and (b) we display the components of the Stokes vector again. The EP is passed at the midpoint of the propagation ($t = T/2 = 30$) and after that the third component of the Stokes vector, i.e. the population inversion, stays zero, which corresponds to $|c_-| = |c_+|$.

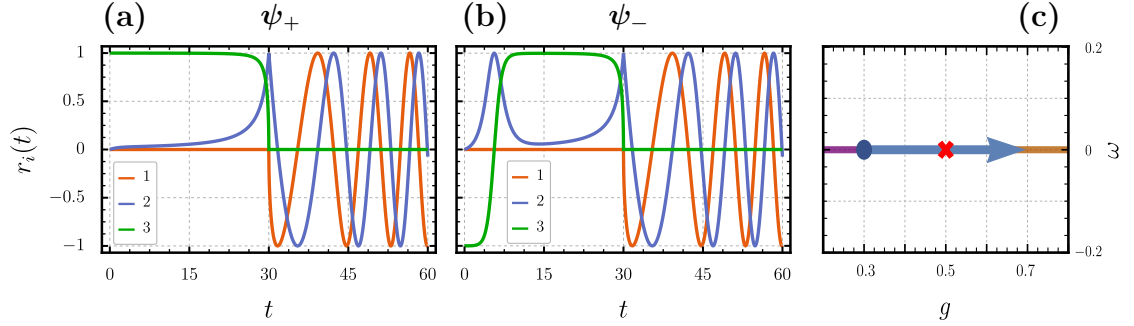


Figure 10.3: Time dependent components of the Stokes vector $r_i(t)$ using a straight parameter path (c) that goes through the EP from the real crossing to the imaginary crossing (\mathcal{PT} -symmetric phase) for (a) an initial ψ_+ and (b) an initial ψ_- state. The Stokes vector for the instantaneous eigenbasis is given as $\mathbf{r} = (2\Re(R_-), 2\Im(R_-), 1 - |R_-|^2)^T / (1 + |R_-|^2)$. The parameters are set at $T = 60$, $r = 0.4$, $\gamma = 1$ and $\alpha = \pi$. The EP is passed at $t = T/2$ where the Stokes vector takes on the value $\mathbf{r}(t_{\text{EP}}) = (0, 1, 0)^T \leftrightarrow c_-/c_+ = i$. After the EP has been crossed the eigenvector populations are perfectly level and stay that way because the eigenvalues are purely real on the imaginary crossing.

10.3 Experimental predictions for EP-centered squares

In the cavity optomechanics group of Harris *et al.* at Yale University it was recently demonstrated that the transfer of energy between two vibrational modes of a cryogenic silicon nitride membrane upon encircling an EP shows also the same chiral behavior [33]. The experimental setup consists of an almost square membrane ($1 \text{ mm} \times 1 \text{ mm} \times 50 \text{ nm}$) with nearly degenerate natural frequencies at 788.024 kHz and 788.487 kHz that are well separated from other resonances of the system. A laser that is coupled into the cavity generates an intra-cavity field that drives the membrane via radiation pressure. At the same time the displacement of the membrane detunes the cavity and hence modulates the intra-cavity field. By precisely adjusting the laser power P and the mean detuning Δ between the laser and the cavity it is possible to bring the system to an EP and perform closed loops around an EP in $\{P, \Delta\}$ -space. The time evolution of population of the two almost degenerate modes can be accurately modeled as a Schrödinger-type equation with a Hamiltonian similar to Eq. 2.2. The parameter variations that are used in the experiment resemble a rectangle in the parameters $\{P, \Delta\}$.

However, the effective Hamiltonian that describes the experiment is not the same as our model Hamiltonian and therefore also the rectangular paths in $\{P, \Delta\}$ are not equivalent to rectangles in the $\{g, \omega\}$ -plane. We have seen earlier though that chirality is inseparably connected to the initial configuration $\{g_0, \omega_0\}$ with respect to the position of the real and imaginary crossing. The overall chiral behavior in an experimental setup can therefore be qualitatively mapped onto the model simply by choosing the right starting point with respect to the chosen EP. This was discussed above where we stated that the EP_- is the parity inverted EP_+ and by properly adapting the starting point as well, e.g. $\phi_0 = 0 \leftrightarrow \phi_0 = \pi$, the result in terms of chirality is the same for both EPs. The exact shape of the contour is therefore not important as long as other criteria are matched, such as the starting point with respect to the real/imaginary crossing and with respect to the position of the EP.

With this in mind we draw another chirality map for square parameter loops in Fig. 10.4. The squares are centered at the EP with $T = 40$. The result looks similar to the EP_+ -centered circular case except that the result for an initial ψ_+ and an ψ_- state are the same. Also, the non-chiral region form a repeating pattern, but it takes almost half of the displayed parameter space. A major difference to the former EP-centered circular loops is that the non-chiral regions close to the real crossing are stationary, i.e. independent on the loop time T , provided that the loop is in the quasi-adiabatic regime in the first place. Very similar stationary non-chiral patterns are found for elliptical parameter paths (not shown).

We conclude that in terms of chirality, only the EP-centered circular trajectories have a special symmetry that reduces the possible non-chiral starting configurations $\{g_0, \omega_0\}$ to lie at the real crossing. Once the circular loops were not EP-centered anymore the equation for the chiral phase boundary became a quadratic one leading to a (second) static non-chiral region close to the EP (see Fig. 9.4). Although this second non-chiral parameter region was not enclosing an EP, we state without proof that the same can be obtained for loops that enclose a single EP.¹⁵

For the experimental loops this symmetry is definitely broken and the resulting chirality therefore shows a stationary phase boundary for loops that only encircle one EP (not shown). This phase boundary is actually a physical manifestation of an *anti-Stokes line*, where some term in the asymptotic expansion changes from increasing to decreasing (or vice versa). However, this is an ongoing investigation and the conclusions are hence not technically matured.

¹⁵Given that they are not EP-centered circular loops.

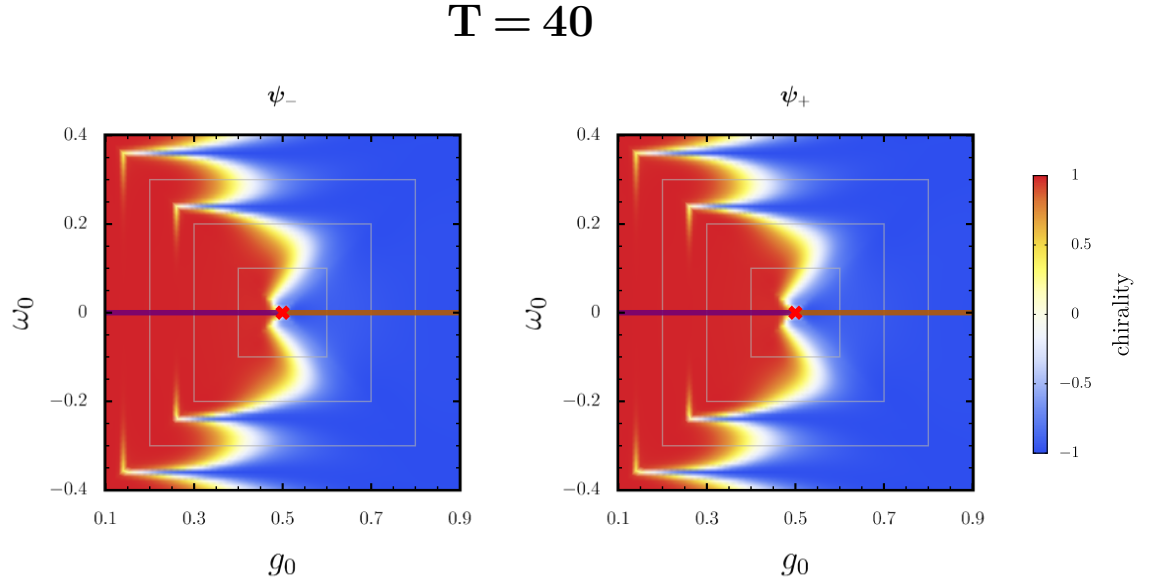


Figure 10.4: Chirality for EP_+ -centered square loops with starting points at $\{g_0, \omega_0\}$. The EP_+ is marked with a red cross and the real/imaginary crossing of the eigenvalues with a purple/orange line respectively. The left column displays initial ψ_- states and the right column ψ_+ states at the respective initial position. The gray, square mesh is drawn to symbolize the corresponding parameter paths used in this plot. The non-chiral region is confined to loops that start close to the real crossing.

11 Conclusion and Outlook

In conclusion, this work sheds a new light on the asymmetric mode switch that is connected to non-Hermitian branch points when performing closed loops in parameter space around them.

We first outlined the basic concepts of non-Hermitian dynamics and its interesting kind of branch point, the exceptional point. A consequence of the non-Hermiticity of the Hamiltonian is the non-orthogonality of its eigenvectors. This led us to the necessity of introducing a generalized Hermitian form, which is applicable for any Hamiltonian in contrast to the c-product. We outlined for a general non-Hermitian Hamiltonian that only the \mathcal{PT} -symmetric phase preserves the norm of a state vector.

To facilitate an analytical understanding of chirality, we derived the analytical solutions of the Schrödinger equation for EP_+ -centered circles and general straight paths. Especially the latter solutions are so far unreported to the best of our knowledge.

The EP-centered circular paths have been solved using a variable starting point ϕ_0 that allowed us to access the whole $\{g, \omega\}$ parameter space. We discovered that chirality is inevitably linked to an exceptional point but the essential requisite is proximity of the parameter loop to an EP and not necessarily including the EP in the contour. Independent of the number of EPs that are enclosed, chirality can only be obtained in the vicinity of an exceptional point. In the case of EP-centered circles, the radius of the loop must not exceed a critical value $r^* \approx 2.277\gamma$, that was inferred analytically. This critical radius does not depend on the loop time T , which emphasizes its phase boundary characteristics.

When we moved the center of the circle g_c so that the parameter path is not EP-centered anymore, we numerically found a new chiral phase boundary equation $g_c^* = 0.500 + 2.140r - 0.548r^2$ that serves as the necessary condition for chirality. The two solutions of this equation give a minimal and maximal radius of the loop depending on the center g_c .

As we investigated the chiral behavior for the EP_+ - and the EP_- -centered circular paths we discovered that they behave as if they were the parity-reflected image of one another. This settles the question of comparability of different sets of parameters [27, 31, 32]. Only the position of the real and imaginary crossing of the eigenvalues together with the initial parameter configuration¹⁶ decide upon chirality. This allows us to switch from the parameters $\{g, \omega\}$ to $\{\gamma, \omega\}$ when we discuss chirality. In the $\{\gamma, \omega\}$ plane, it is possible to derive a more general analytical solution for circles with arbitrary center $\{\gamma_c, \omega_c\}$ that grants the possibility for a general analytical phase boundary condition.

¹⁶We saw that starting on the real crossing does not admit a chiral phase whereas starting on the imaginary crossing gives always a chiral solution.

The new class of general straight paths solutions were used to explore the effects of the EP itself and to perform square parameter paths that are centered around the EP. It will be interesting to see the phase boundaries for different shapes of the closed contours. Also, as we have established that chirality only necessitates a certain closeness of the loop this opens up the way to examine closed contours in the vicinity of higher order exceptional points. This is particularly interesting since higher order EPs cannot be unambiguously encircled, but proximity is still well-defined.

Finally, EP-centered square parameter paths showed a chiral phase boundary for loops that start close to the real crossing. The distinctive feature of this boundary is its independence of the loop time T in contrast to the EP-centered circular loops, where the non-chiral region decreased for larger loop times. This property could be used to define a simple yet elegant measurement along the lines of [33] to visualize anti-Stokes lines in a cavity-optomechanical system.

Acknowledgments

At this point I want to express my sincere gratitude to the people who have contributed in one way or another to the completion of this diploma thesis.

Foremost, I am very much indebted to my adviser Prof. Stefan Rotter who gave me the possibility to pursue the research on this fascinating topic. During our numerous extensive discussions he guided me with his profound knowledge and encouragement. On my behalf, I very much appreciate his understanding patience and his reliability on a personal level.

My gratitude also to my colleague Juraj Feilhauer with whom the collaboration on this project has been a great pleasure and will hopefully continue to prosper in the following. The whole research group of Prof. Rotter on the third floor also deserve considerable credit for the deliberate discussions, the joyful lunch breaks and the help with technical issues. This holds especially for my former office mates as well as my current ones that had to put up with some minor outbursts concerning technical difficulties.

I am moreover thankful for the opportunity to visit Prof. Jack Harris and his research group at *Yale University* in the course of this work. The warm hospitality of him and his research group made my stay very pleasant. They provided me with extensive insights into their cavity-optomechanical experiment and helped me to elaborate on my theoretical work as well. I look back with great pleasure to my weekly meetings with Prof. Harris and his astute comments as well as to all the memorable moments with my lab colleagues who generously put it on themselves to include me in all their activities right from the start.

Thereunto, I would like to thank the members of the selection committee of the TU Wien for the granted financial support, which made this collaboration possible and gave me this opportunity that I will certainly benefit from in my future scientific career.

Finally, I want to take this opportunity to thank my friends and family for their unconditional support and encouragement and to apologize to all those that I forgot to mention. The one person that must not go unmentioned is my brother, Gerald Schumer. I highly appreciate his perpetual help, trust and belief - simply thank you for everything that you have done for me throughout my whole life.

List of Acronyms and Abbreviations

| | |
|-------------------------|-------------------------------------|
| cw | Clockwise |
| ccw | Counter-clockwise |
| COM | Cavity-optomechanics |
| CPA | Coherent perfect absorber |
| c_Y | Chirality |
| DP | Diabolical point |
| EB | Eigenbasis |
| EP | Exceptional point |
| MB | Mode basis |
| ODE | Ordinary differential equation |
| p_I | Population inversion |
| PT | Parity-time |
| SE | Schrödinger equation |
| t_E | Transfer efficiency |
| TDSE | Time-dependent Schrödinger equation |

| | |
|-----------------|---|
| B | Metric for the generalized Hermitian form |
| H | Hamiltonian in the mode basis |
| H_{EB} | Hamiltonian in its eigenbasis |
| U | Time-evolution operator in the mode basis |
| \tilde{U} | Time-evolution operator in the eigenbasis of H |
| λ_{\pm} | Eigenvalues of the Hamiltonian in the mode basis |
| $ +\rangle$ | Eigenvector to the eigenvalue λ_+ |
| $ -\rangle$ | Eigenvector to the eigenvalue λ_- |
| $ v\rangle$ | Eigenvector at the EP |
| $ h\rangle$ | Generalized eigenvector of rank two at the EP |
| a, b | Expansion coefficients in the mode basis |
| c_-, c_+ | Expansion coefficients in the eigenbasis of H |
| T | Period of a single parametric closed loop |
| θ | Mixing angle of the eigenvectors |
| f | Non-adiabaticity function |
| ϕ_0 | Initial starting angle for circular loops |
| ψ_- | Initial eigenstate that is subject to loss ($ -(0)\rangle$) |
| ψ_+ | Initial eigenstate that is subject to gain ($ +(0)\rangle$) |
| Π_i | Projector onto the i -th basis state |

Bibliography

- [1] N. Moiseyev. *Non-Hermitian Quantum Mechanics*. Cambridge University Press (2011).
- [2] C. M. Bender. *Ghost busting: Making sense of non-Hermitian Hamiltonians*. Algebraic Analysis of Differential Equations: From Microlocal Analysis to Exponential Asymptotics Festschrift in Honor of Takahiro Kawai **70**, 55 (2008).
- [3] C. M. Bender, D. C. Brody, and H. F. Jones. *Complex Extension of Quantum Mechanics*. Physical Review Letters **89**, 270401 (2002).
- [4] D. C. Brody. *Biorthogonal quantum mechanics*. Journal of Physics A: Mathematical and Theoretical **47**, 035305 (2014).
- [5] P. D. Mannheim. *PT symmetry as a necessary and sufficient condition for unitary time evolution*. Philosophical Transactions of the Royal Society A: Mathematical, Physical and Engineering Sciences **371**, 20120060 (2013).
- [6] O. N. Kirillov, A. A. Mailybaev, and A. P. Seyranian. *On eigenvalue surfaces near a diabolic point*. 2005 International Conference on Physics and Control, PhysCon 2005, Proceedings **2005**, 319 (2005).
- [7] W. D. Heiss and A. L. Sannino. *Avoided level crossing and exceptional points*. Journal of Physics A **23**, 1167 (1990).
- [8] M. V. Berry. *Physics of nonhermitian degeneracies*. Czechoslovak Journal of Physics **54**, 1039 (2004).
- [9] W. D. Heiss. *Exceptional points of non-Hermitian operators*. Journal of Physics A: Mathematical and General **37**, 2455 (2004).
- [10] O. N. Kirillov, A. A. Mailybaev, and A. P. Seyranian. *Unfolding of eigenvalue surfaces near a diabolic point due to a complex perturbation*. Journal of Physics A: Mathematical and General **38**, 5531 (2005).
- [11] W. D. Heiss. *The Physics of exceptional points*. JPhys A **44****016**, 28 (2012).
- [12] D. C. Brody and E. M. Graefe. *Information geometry of complex hamiltonians and exceptional points*. Entropy **15**, 3361 (2013).
- [13] Z. Lin, H. Ramezani, T. Eichelkraut, T. Kottos, H. Cao, and D. N. Christodoulides. *Unidirectional Invisibility Induced by P T -Symmetric Periodic Structures*. Physical Review Letters **106**, 213901 (2011).

- [14] Y. D. Chong, L. Ge, H. Cao, and A. D. Stone. *Coherent Perfect Absorbers: Time-Reversed Lasers*. Physical Review Letters **105**, 053901 (2010).
- [15] J. Wiersig. *Enhancing the Sensitivity of Frequency and Energy Splitting Detection by Using Exceptional Points: Application to Microcavity Sensors for Single-Particle Detection*. Physical Review Letters **112**, 203901 (2014).
- [16] J. Wiersig. *Sensors operating at exceptional points: General theory*. Physical Review A **93**, 1 (2016).
- [17] W. Chen, S. Kaya Özdemir, G. Zhao, J. Wiersig, and L. Yang. *Exceptional points enhance sensing in an optical microcavity*. Nature **548**, 192 (2017).
- [18] S. Assawaworrarit, X. Yu, and S. Fan. *Robust wireless power transfer using a nonlinear parity-time-symmetric circuit*. Nature **546**, 387 (2017).
- [19] M. Liertzer, L. Ge, A. Cerjan, A. D. Stone, H. E. Türeci, and S. Rotter. *Pump-induced exceptional points in lasers*. Physical Review Letters **108**, 1 (2012).
- [20] M. Brandstetter, M. Liertzer, C. Deutsch, P. Klang, J. Schöberl, H. E. Türeci, G. Strasser, K. Unterrainer, and S. Rotter. *Reversing the pump dependence of a laser at an exceptional point*. Nature Communications **5** (2014).
- [21] W. D. Heiss. *Repulsion of Resonance States and Exceptional Points*. Physical Review E **61**, 4 (1999).
- [22] A. A. Mailybaev, O. N. Kirillov, and A. P. Seyranian. *Geometric phase around exceptional points*. Physical Review A - Atomic, Molecular, and Optical Physics **72**, 15 (2005).
- [23] S.-D. Liang and G.-Y. Huang. *Topological invariance and global Berry phase in non-Hermitian systems*. Physical Review A **87**, 012118 (2013).
- [24] C. Dembowski, H.-D. Gräf, H. L. Harney, A. Heine, W. D. Heiss, H. Rehfeld, and A. Richter. *Experimental Observation of the Topological Structure of Exceptional Points*. Physical Review Letters **86**, 787 (2001).
- [25] C. Dembowski, B. Dietz, H.-D. Gräf, H. L. Harney, A. Heine, W. D. Heiss, and A. Richter. *Encircling an exceptional point*. Physical Review E **69**, 056216 (2004).
- [26] M. V. Berry and R. Uzdin. *Slow non-Hermitian cycling: exact solutions and the Stokes phenomenon*. Journal of Physics A: Mathematical and Theoretical **44**, 435303 (2011).
- [27] M. V. Berry. *Optical polarization evolution near a non-Hermitian degeneracy*. Journal of Optics **13**, 115701 (2011).
- [28] R. Uzdin, A. Mailybaev, and N. Moiseyev. *On the observability and asymmetry of adiabatic state flips generated by exceptional points*. Journal of Physics A: Mathematical and Theoretical **44**, 435302 (2011).

- [29] I. Gilary, A. A. Mailybaev, and N. Moiseyev. *Time-asymmetric quantum-state-exchange mechanism*. Physical Review A - Atomic, Molecular, and Optical Physics **88**, 010102 (2013).
- [30] T. J. Milburn, J. Doppler, C. A. Holmes, S. Portolan, S. Rotter, and P. Rabl. *General description of quasiadiabatic dynamical phenomena near exceptional points*. Physical Review A - Atomic, Molecular, and Optical Physics **92**, 1 (2015).
- [31] A. U. Hassan, B. Zhen, M. Soljačić, M. Khajavikhan, and D. N. Christodoulides. *Dynamically Encircling Exceptional Points: Exact Evolution and Polarization State Conversion*. Physical Review Letters **118**, 093002 (2017).
- [32] J. Doppler, A. A. Mailybaev, J. Böhm, U. Kuhl, A. Girschik, F. Libisch, T. J. Milburn, P. Rabl, N. Moiseyev, and S. Rotter. *Dynamically encircling exceptional points in a waveguide: asymmetric mode switching from the breakdown of adiabaticity*. Nature **537**, 76 (2016).
- [33] H. Xu, D. J. Mason, L. Jiang, and J. G. E. Harris. *Topological energy transfer in an optomechanical system with exceptional points*. Nature **537**, 80 (2016).
- [34] U. Günther, I. Rotter, and B. F. Samsonov. *Projective Hilbert space structures at exceptional points*. Journal of Physics A: Mathematical and Theoretical **40**, 8815 (2007).
- [35] W. D. Heiss and H. L. Harney. *The chirality of exceptional points*. The European Physical Journal D **17**, 149 (2001).
- [36] Y. D. Chong, L. Ge, and A. D. Stone. *PT-Symmetry Breaking and Laser-Absorber Modes in Optical Scattering Systems*. Physical Review Letters **106**, 093902 (2011).
- [37] S. Bittner, B. Dietz, H. L. Harney, M. Miski-Oglu, A. Richter, and F. Schäfer. *Scattering experiments with microwave billiards at an exceptional point under broken time-reversal invariance*. Physical Review E - Statistical, Nonlinear, and Soft Matter Physics **89**, 1 (2014).
- [38] K. V. Kepesidis, T. J. Milburn, J. Huber, K. G. Makris, S. Rotter, and P. Rabl. *PT-symmetry breaking in the steady state of microscopic gain-loss systems*. New Journal of Physics **18**, 095003 (2016).
- [39] K. G. Makris, L. Ge, and H. E. Türeci. *Anomalous Transient Amplification of Waves in Non-normal Photonic Media*. Physical Review X **4**, 041044 (2014).
- [40] N. Moiseyev, P. Certain, and F. Weinhold. *Resonance properties of complex-rotated hamiltonians*. Molecular Physics **36**, 1613 (1978).
- [41] Wolfram Research. *Two-argument inverse tangent*. Available at: <http://functions.wolfram.com/01.15.02.0001.01> (Accessed: 10 December 2017).

- [42] M. V. Berry. *Quantal Phase Factors Accompanying Adiabatic Changes*. Proceedings of the Royal Society A: Mathematical, Physical and Engineering Sciences **392**, 45 (1984).
- [43] A. Leclerc, D. Viennot, and G. Jolicard. *The role of the geometric phases in adiabatic population tracking for non-Hermitian Hamiltonians*. Journal of Physics A: Mathematical and Theoretical **45**, 415201 (2012).
- [44] A. V. Sokolov, A. A. Andrianov, and F. Cannata. *Non-Hermitian quantum mechanics of non-diagonalizable Hamiltonians: puzzles with self-orthogonal states*. Journal of Physics A: Mathematical and General **39**, 10207 (2006).
- [45] S. Ibáñez and J. G. Muga. *Adiabaticity condition for non-Hermitian Hamiltonians*. Physical Review A **89**, 033403 (2014).
- [46] A. Mostafazadeh. *Exact PT-symmetry is equivalent to Hermiticity*. Journal of Physics A: Mathematical and General **36**, 7081 (2003).
- [47] M. Abramowitz and I. A. Stegun. *Handbook of Mathematical Functions, With Formulas, Graphs, and Mathematical Tables*,. Dover Publications, Incorporated, 10 edn. (1974).
- [48] *NIST Digital Library of Mathematical Functions*. <http://dlmf.nist.gov/>, Release 1.0.15 of 2017-06-01.
- [49] C. Chicone. *Ordinary Differential Equations with Applications* **1** (1999).
- [50] A. U. Hassan, G. L. Galmiche, G. Harari, P. LiKamWa, M. Khajavikhan, M. Segev, and D. N. Christodoulides. *Chiral state conversion without encircling an exceptional point*. Physical Review A **96**, 052129 (2017).
- [51] A. U. Hassan, G. L. Galmiche, G. Harari, P. LiKamWa, M. Khajavikhan, M. Segev, and D. N. Christodoulides. *Erratum: Chiral state conversion without encircling an exceptional point [Phys. Rev. A 96 , 052129 (2017)]*. Physical Review A **96**, 069908 (2017).